The Dissertation Committee for Ping-Chun Li Certifies that this is the approved version of the following dissertation:

Large-Area Resonant and Non-Resonant Optical Nanostructures

Committee:

Edward T. Yu, Supervisor

Andrea Alù

C. Grant Willson

S. V. Sreenivasan

Hao Ling

Large-Area Resonant and Non-Resonant Optical Nanostructures

by

Ping-Chun Li, B.S.; M.S.E.

Dissertation

Presented to the Faculty of the Graduate School of

The University of Texas at Austin

in Partial Fulfillment

of the Requirements

for the Degree of

Doctor of Philosophy

The University of Texas at Austin

August 2014

Dedication

To my family

Acknowledgements

I would like to thank my advisor Prof. Edward T. Yu for his guidance, wisdom, broad knowledge in different research topics throughout my Ph.D. journey.

I thank my parents and grandparents for always supporting me in all my endeavors. The high value they place on education is the large part of the reason I have been able to accomplish my Ph.D.

I am grateful to my committee members Prof. Andrea Alu for discussions on metamaterials concepts and insights for data analysis, Prof. Hao Ling for discussions on microwave antenna designs, considerations, and his wonderful classes, Prof. S. V. Sreenivasan and Prof. C. G. Willson for sharing their experiences and knowledge in the field of nanoimprint lithography, and providing a wonderful team and project to work with.

I thank all the ETY group member: Dr. Lei Zhu, Dr. Clay Mcpheetors, Dr. Keun-Woo Park, Dr. Vaishno Dasika, Chengqing Hu, Xiaohan Li, Li Ji, Chris Brennan, and Jian Zhang for discussions and helps on clean room trainings/recipes, simulation software, and equipment setups.

I also wish to thank all my collaborators in UT: Dr. Pai-Yen Chen, Dr. Xing-Xiang Liu, Dr. Yang Zhao, Francesco Monticone, and Nasim Estakhri (Prof. Andrea Alu's group) for discussions on plasmonic metamaterials; Dr. Shang-Te Yang (Prof. Hao Ling's group) for always listening to my recent research progress and constantly providing keen insights; Dr. En-Shao Liu, Babak Fallahazad, Stefano Larentis, and Dr. Jiamin Xue (Prof. Tutuc's lab) for helps on electrical measurement and setup; Dr. Xiaohui Lin, Dr. Xiaochuan Xu, Dr. Yang Zhang, Dr. Wei-Cheng Lai, and Yi Zou (Prof. Ray

Chen's group) for discussions on electron beam lithography; Andy Yin, and Praveen Joseph for discussions on electron beam lithography and etching recipes (Prof. S. V. Sreenivasan's group); Kueifu Lai, Tzuhsuan Ma, Nima Dabidan, and Nihal Arju (Prof. Shvets' group) for discussions on experiments and theories of plasmonic metamaterials.

I would also like to thank my collaborators outside UT: Dr. Jen-Chien Chang and Prof. Arthur La Porta (Univ. of Maryland) for optical tweezers experiments. It has been a wonderful experience for us to collaborate with college classmate which we have never thought of. In addition, I thank (and apoligize) to Jen-Chien and his roommates, Dr. Tung-Chang Liu and Dr. Guo-Yuan Lien for listening to my complaints; Sean Kung (Rutgers Univ.) for detailed discussion on nanosphere lithography which not just become backbone of my research works but also become a versatile tool for ETY Lab. Dr. Yu-Cheng Tsai and Amy Wu (Princeton Univ.) for discussions on optical imaging and measurement setup. Dr. Shrawan Singhal and Dr. Ovadia Oved (Molecular Imprints) for discussions on fabrication process of flexible polymer substrates. Dr. Rao Tatavarti (Microlink Devices) and Dr. Kimberly Sablon (Army Research Laboratory) for providing solar cell samples and helpful suggestions.

I also appreciate the staff of the Microelectronic Research Center in UT, including Dr. Ferrer Domingo, Dr. Marylene Palard, William Ostler, Johnny Johnson, and Ricardo Garcia for equipment trainings and maintenance.

Special thanks to Dr. Horan and Dr. Kasper who literally save my life.

Finally, I would like to thank my wife, Wanhsuan Li, for being with me. Without you, it would not have been possible to write this doctoral thesis.

Large-Area Resonant and Non-Resonant Optical Nanostructures

Ping-Chun Li, Ph. D.

The University of Texas at Austin, 2014

Supervisor: Edward T. Yu

Manipulation of light via subwavelength nanostructures is currently a subject of intense research interest, and is enabling the development of nanostructured photonic crystal, metamaterials and metasurfaces that provide a variety of new optical and electromagnetic functionalities, or that enable existing functionalities to be realized in new and often extremely compact form factors. This dissertation will include wide-angle wavelength-selective metasurface, omnidirectional enhancement in photovoltaic performance via subwavelength gradient anti-reflection coating, and applications of birefringent nanocylinders for single-molecule spectroscopy.

In wide-angle wavelength-selective metasurface, high and broad reflectance (~95%) with low absorption (<5%) are shown to be achieved with multilayer metasurface structures. These characteristics are shown to be independent of interlayer misalignment and defects within individual layers. Interactions between different metasurface layers due to Fabry-Perot resonance are also examined with analytical models and numerical simulations. Wavelenth-selective focusing at optical wavelengths which is enabled by large-area nanosphere lithography on a flexible substrate is demonstrated. In omnidirectional enhancement in photovoltaic performance via subwavelength gradient anti-reflection coating, large-area "moth-eye" structure fabricated on a flexible substrate

is shown to have high transmittance (>85%) at large angle of incidences (>70^{o}) and insensitivity to polarizations. Integration of the "moth-eye" anti-reflection coating together with nanostructured gradient Al_2O_3/TiO_2 on a GaAs solar cell shows significant improvements on external quantum efficiency (EQE) and short circuit current over all angle of incidences compared with conventional thin film anti-reflection coating. Detailed design, simulation, and fabrication of these nanostructured anti-reflection coating for reducing the discontinuity in refractive index profile will also be discussed.

In application of birefringent nanocylinders for single-molecule spectroscopy, the design and fabrication method for large quantity of subwavelength birefringent nanoparticle are also discussed. These birefringent nanoparticles are shown to be stably trapped in an optical torque wrench setup, and enable observation of the dynamical response of a double-stranded DNA under torsional and extensional forces.

Table of Contents

List of Figures

Chapter 1: Introduction

Manipulation of light via subwavelength nanostructures is currently a subject of intense research interest, and is enabling the development of nanostructured photonic crystal, metamaterials and metasurfaces that provide a variety of new optical and electromagnetic functionalities, or that enable existing functionalities to be realized in new and often extremely compact form factors[1-4]. Most such concepts involve structures fabricated in a rigid, single-layer, planar geometry[5-11]. However, three-dimensional plasmonic nanostructures have been shown to enable additional possibilities for engineering optical chirality[12], negative refractive indices[13], and molecular sensing behavior[14]. Furthermore, interest in highly nonplanar geometries and fabrication on flexible or stretchable substrates[15-18] has been fueled by applications such as transformation optics[19], cloaking[20-21], and imaging[22]. The ability to fabricate plasmonic nanostructures with multiple plasmonic layers, over large areas, and on flexible substrates could enable the realization of additional new optical functionalities, and the application of plasmonic nanostructures in a broad range of new settings in which structural flexibility, conformation to curved or irregular surfaces, large areas, and/ or low cost are required.

Chapter 2 summarizes the experimental demonstration, numerical simulation and theoretical modeling of optical resonant nanostructures. In these results, we focus on the optical properties and performance of multilayer metasurfaces. For a single layer metasurface structure, the main metasurface resonance is shown to be independent of polarizations and incident angle, and sensitive only to the material composition, size and periodicity of a single element. Higher order resonance associated with surface plasmon polariton coupling and Wood's anomaly are sensitive to angle of incidence, and less

pronounced compared with the metasurface resonance. For multilayer metasurface structures, high and broad reflectance with low absorption are shown to be achieved by arranging each layer under Bragg criteria. Interaction between different metasurfaces is dominated by Fabry-Perot resonance. Fabry-Perot modes which reside between two metasurfaces with different distances are also demonstrated in experiments and confirmed with an analytical model and numerical simulations. A non-conventional m=0 resonance is also supported due to the wavelength-dependent phase-shift from the metasurface. These characteristics are also shown to be insensitive to the interlayer misalignment and defects within individual layers, and enable possibilities of using rapid, large-area, nanoscale nanosphere lithography to fabricate these devices. An experimental demonstration via the advantages of robust properties robust to interlayer misalignment, insensitivity to angle of incidence, and large-area nanosphere lithography fabrication method on flexible substrate enables the wavelength-selective focusing at optical wavelengths. Finally, optimization of a proposed photovoltaic-thermal system based on a flexible wavelength-selective metasurface is discussed.

Chapter 3 summarizes the experimental demonstration, numerical simulation and theoretical modeling of subwavelength anti-reflection coating. In these results, we first focus on optimization and realization of an antireflection coating nanostructure on glass. Simulations and experiments reveal that an optimized nanopillar structure can achieve transmittance >85% for angles of incidence in excess of 70^{o} at visible wavelengths and shown to be superior to tapered "moth-eye" structures with low dimensions. We then improved our fabrication process to realize a "moth-eye" nanostructure with significant height to provide a subwavelength graded-index profile on a flexible polymer substrate for packaging. The demonstrated transmittance is ~85% at 75^{o} which is ~2x improvement over unpatterned polymer substrate. Further improvements and optimizations via

"nanoisland" structures enabled by nanosphere lithography on interfaces between conventional bilayer antiflection coating and packaging materials show much better performance at large angles of incidence. Finally, we integrated the "moth-eye" structure on polymer together with a "nanoisland" structure on a bilayer antiflection coating integrated with GaAs solar cells. The measured external quantum efficiency and short circuit current show enhancement ~1.06x (at 0^o) and 1.67x (at 80^o).

Chapter 4 summarizes the experimental demonstration and theoretical modeling of torsional and extensional dynamics of single DNA molecules via optical tweezers. First, we demonstrated a low-cost, large throughput fabrication method via nanosphere lithography for birefringent nanocylinders. These birefringent nanocylinders have been shown to be stably trapped in the optical torque wrench setup and provide a suitable platform for studying single-molecule dynamics.

Part of section 2.2 was published in *Applied Physics Letters* 2011, P.-C. Li, Y. Zhao, A. Alu, and E. T. Yu [23]. Part of section 2.3 was published in *Journal of American Society B* 2013, P.-C. Li, and E. T. Yu [24]. Part of section 2.4 was published in *Journal of Applied Physics 2013* [25]. Part of section 3.2 was published in *Journal of American Society* B 2013, P.-C. Li and E. T. Yu [26]. Part of section 3.3 is now under preparation for publication. Part of chapter 4 has been accepted by *Nanotechnology*.

Chapter 2: Flexible, Large-Area, Wide-Angle, Wavelength-Selective Metasurface for Solar Energy Harvesting

2.1 MOTIVATION

Concentrating solar power (CSP) systems employing parabolic trough collectors and thermal absorbers represent a well-established and relatively mature technology that has delivered proven performance over multiple decades of real-world operation. CSP systems also possess the important advantage of providing energy storage in the form of heat. Photovoltaic (PV) conversion of solar power to electricity represents a similarly established technology offer great in promise for continued reductions in cost and increases in efficiency, but does not by itself provide energy storage. A hybrid system incorporating both PV and thermal conversion could enable major improvements in performance combined with the provision of both variable electricity and dispatchable heat. However, CSP rely on photothermal processes which convert solar energy to heat with efficiency which is relatively constant over the entire solar spectrum, depending on the optical loss of the coating on the thermal absorber. The efficiency can be increased by raising the thermal absorber's operating temperature due to Carnot cycle limit; however, for temperature > 600^{o}C there is high technical risk due to stability of pumping and storing these high temperature fluids. On the other hand, photovoltaic (PV) processes are wavelength dependent and efficiency is closely related to the bandgap energy of the absorbing material. Photon energy below the bandgap cannot be absorbed and is often dissipated as heat within the cell; photon energy larger than the bandgap can only be partly converted into electricity, and the remainder is dissipated as heat. Therefore, the optimal way to utilize solar energy is to spectrally split the optical wavelength portion ($\lambda_{on} < \lambda < \lambda_{off}$) into PV converter, which has higher efficiency in this region, and the remainder ($\lambda < \lambda_{on}$ and $\lambda > \lambda_{off}$) to a thermal converter as shown in Figure 2.1.

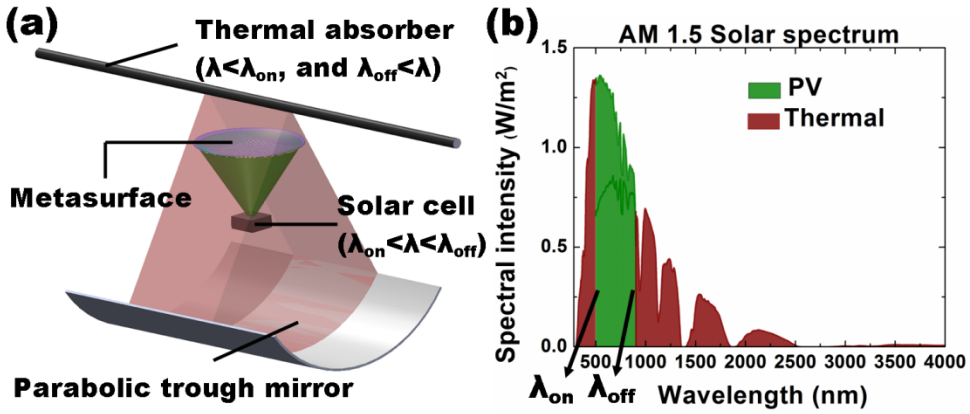

Figure 2.1 (a) Schematic diagram of a photovoltaic-thermal hybrid system. (b) Spectral distributions of PV and thermal absorber from an AM 1.5 solar spectrum.

A key requirement for efficiently combining PV and thermal conversion is the ability to direct the portions of the solar spectrum most efficiently converted to electric power via PV – typically the visible and near-infrared portions of the spectrum – to a high performance PV cell, and those less amenable to photovoltaic conversion – typically ultraviolet (UV) and infrared (IR) light – to a thermal absorber. Conventional optical components such as dichroic reflectors provide very good capability for wavelength-selective transmittance and reflectance, but have constraints on bandwidth and a substantial dependence of transmittance and reflectance on angle of incidence. Because the optical concentrator structures in CSP systems inevitably yield reflected light propagating over a range of angles, new optical components that can achieve wavelength-selective optical transmittance and reflectance independent of the direction and polarization of incident light are required. Furthermore, advanced optical designs are essential to maximize optical concentration factors, thereby reducing cost and increasing efficiency.

2.2 SINGLE-LAYER METASURFACE

In section 2.2, we discuss the modeling, fabrication and characterization of a single layer plasmonic metasurface with subwavelength features, whose dominant resonance is independent of incident angle and polarization, and is sensitive only to the material composition and geometry of a single element. Higher-order resonances, associated with surface plasmon polariton (SPP) coupling and higher diffraction orders, are sensitive to the incident angle and the array periodicity, and less pronounced compared with the metasurface resonance. Numerical simulations and theoretical analyses highlight a clear physical difference between SPP resonances and the dominant metasurface collective resonance, whose properties may be of great interest for plasmonic solar cells and subwavelength color filters.

2.2.1 The concept of metasurface

Our results can be understood by the concept of a metasurface, a periodic array of scattering elements whose dimensions and periods are small compared with the operating wavelength. These features allow for characterization in terms of dipolar polarizabilities of each scatterer. Imposition of the generalized sheet transition conditions[23-24] (GSTCs) for average electromagnetic fields across the surface allows the boundary-value problem to be solved for the dominant diffraction order. The subwavelength period of the metasurface ensures that all higher-order diffraction terms are evanescent, implying that the collective resonance of the array is weakly dependent on the angle of incidence. Under this assumption, we can characterize the metasurfaces using generalized dyadic polarizabilities, which describe the level of averaged electric and magnetic polarization for applied electric and magnetic fields. We assume them to be diagonal in a suitable reference system, due to the symmetries of the metasurface elements:

$$\overleftrightarrow{\alpha_{ES}} = \alpha_{ES}^{xx}\,\vec{x}\vec{x} + \alpha_{ES}^{yy}\,\vec{y}\vec{y} + \alpha_{ES}^{zz}\,\vec{z}\vec{z}, \tag{2-1}$$

$$\overleftrightarrow{\alpha_{MS}} = \alpha_{MS}^{xx}\,\vec{x}\vec{x} + \alpha_{MS}^{yy}\,\vec{y}\vec{y} + \alpha_{MS}^{zz}\,\vec{z}\vec{z}\,. \tag{2-2}$$

Under this definition, the generalized polarizabilities include the coupling effects among the elements in the surface. In the limit of small periods, the polarizabilities do not depend on the angle of incidence and are dominated by the individual element response, but for larger periods spatial dispersion effects may arise. For the simple shapes considered here (patches), in the subwavelength limit electric effects are expected to dominate the magnetic ones. The reflection and transmission coefficients can then be derived as a function of the electric and magnetic generalized polarizabilities. The resonance conditions leading to total reflection in the limit of zero losses may be obtained as a function of incident angle and polarization as[25]

$$k_0^2 \alpha_{MS}^{xx} (\alpha_{ES}^{yy} - \alpha_{MS}^{zz} \sin^2\theta) = 4 \text{ for TE}, \tag{2-3}$$

$$k_0^2 \alpha_{ES}^{xx} (\alpha_{MS}^{yy} - \alpha_{ES}^{zz} \sin^2\theta) = 4 \text{ for TM}, \tag{2-4}$$

where k_0 is the free-space wave vector, and TE and TM stand for transverse electric and transverse magnetic polarization, respectively.

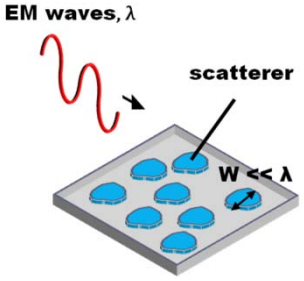

Figure 2.2: Schematic diagram of a metasurface consisting of arbitrary shape scatters on a surface. The rough size of the scatter is denoted as *W*, and the incident wavelength is λ.

2.2.2 Metasurface resonance

For these studies in section 2.1, 1×1 mm^2 areas on a glass substrate coated with 150 nm indium tin-oxide (ITO) were patterned with two dimensional arrays of square

patches using electron beam lithography. The array side length and periodicity of each patch are denoted by *W* and *L*, respectively. A 30nm-thick Au layer is deposited by electron beam evaporation, followed by a standard lift-off process to create the Au patch structure. A schematic diagram of the sample structure and experimental geometry, and a scanning electron micrograph of an Au patch array, are shown in Figure 2.3(a). Figure 2.3(b)(c) shows a series of optical microscope images of fabricated square patches array (~100μm x 100μm for each) as functions of *W*, *L*, and materials. For Ag metasurfaces, we observe the reflected color changes from blue (*W*~60nm), green (*W*~80nm) to yellow (*W*~120nm); on the other hand, the reflected colors of different dimension of Au metasurface are all yellow.

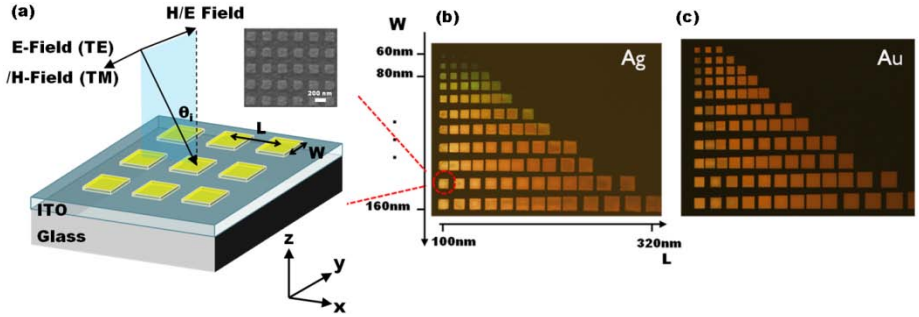

Figure 2.3: (a) Schematic diagram of the metasurface structure on an ITO coated glass substrate under illumination with TE and TM polarization respectively. The inset shows a scanning electron micrograph of a L = 200 nm, W = 100nm device. (b)(c) Optical microscope image of E-beam lithography fabricated square array metallic patches as function of *W* and *L* with different deposited metal, Ag, and Au, respectively. The square size is ~100 μm x 100 μm.

Optical transmittance measurements in these studies were performed using collimated light from a halogen lamp spectrally resolved by a monochromator. The monochromatic light is linearly polarized by a Glan-Thompson polarizer before it reaches the device. The device is mounted on a rotating stage, so that measurements can be performed at different incident angles θ_i. Numerical simulations of the field distribution

in these structures are based on Rigorous Coupled Wave Analysis (RCWA)[26-27] and enhanced with Modal Transmission Line (MTL) theory.[28] The material dispersion of Au and glass are modeled using the Lorentz-Drude model with published material parameters,[29] which fit well with experimental measurements.[30] The optical properties of ITO can vary due to different deposition methods, so we fit its dielectric constant from our measurements, and we neglect here its weak frequency dispersion in the optical regime.

The Au structures analyzed here have typical dimensions *W*, *L* of 100-400 nm, and thickness of 30 nm, ensuring that the transverse components of the electric polarizability dominate the ones in the normal direction ($\alpha_{ES}^{zz} \approx 0$). For oblique TM incidence, a normal magnetic dipole moment may in principle be induced on the metasurface, even in the limit of zero thickness, but due to the simple shape of our structures, this magnetic response is expected to be negligible in the subwavelength regime. These considerations enable resonant conditions to be achieved that are weakly dependent on the incidence angle, as $\alpha_{ES}^{yy} >> \alpha_{MS}^{zz} \sin^2\theta$ and $\alpha_{MS}^{yy} >> \alpha_{ES}^{zz} \sin^2\theta$ in Eqs. (2-3) and (2-4).

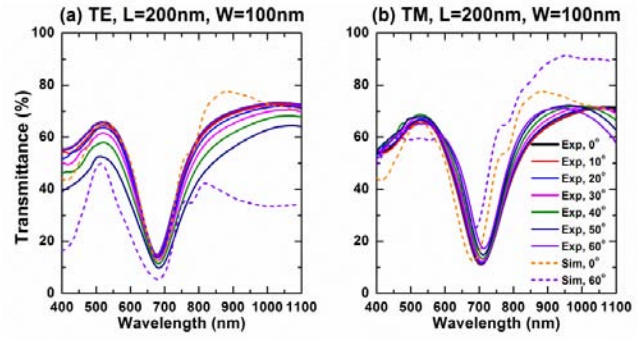

Figure 2.4: Transmission spectra of device shown schematically in Figure 2.3(a) illustrated schematically in Figure 2.3(a) with *L* = 200 nm, *W* = 100 nm for (a) TE, (b) TM polarization. Solid and dashed lines represent the measured and simulated spectra, respectively.

2.2.3 Surface plasmon resonance and Wood's anomaly

Similar experiments have been conducted with larger Au patches, L = 400 nm, W = 200 nm, as shown in Figure 2.5. From both the experimental data and simulations, we notice that the main metasurface resonant dip (~900 nm) remains unchanged under different polarization and incident angles, but is shifted to longer wavelengths compared with the L = 200 nm, W = 100 nm device (~680 nm), as expected due to the larger size of the individual metasurface elements.[31] In this case, the array period is still substantially smaller than the wavelength, and the polarizability model holds, yielding essentially no dependence on the incidence angle.

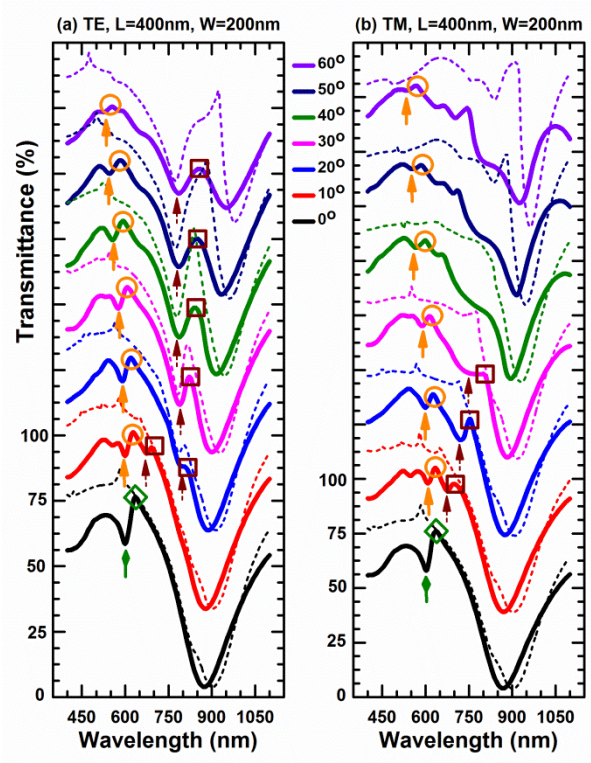

Figure 2.5: Transmission spectra of a L = 400 nm, W = 200 nm device for different incident angles with (a) TE and (b) TM polarization. Solid and dashed lines represent measured and simulated spectra, respectively. Transmission spectra at different incident angles have been offset vertically by 35% each for clarity. Different colored arrows indicate different SPP-coupled modes: green, (±1,0) and (0,±1); orange, (±1,0); brown, (0,-1). Different colors of circles indicate different orders of Wood's anomalies: green, (±1,0) and (0,±1); orange, (±1,0); brown, (0,-1).

In addition to the main metasurface resonance, we notice a local minimum appearing at ~600 nm (indicated by a green arrow) for both TE and TM polarization when $\theta_i = 0^o$ in Figure 2.5. As θ_i increases, this local minimum starts to split into two smaller dips (indicated by orange and brown arrows) which gradually shift away from each other. This effect is associated with the coupling of incident light with an SPP

supported by the grating. Conservation of momentum imposes the following condition for SPP coupling: [32]

$$\vec{k}_{SPP} = \vec{k}_{in} + m_x\vec{G}_1 + m_y\vec{G}_2, \tag{2-5}$$

where $k_{SPP} = (2\pi/\lambda)\sqrt{\varepsilon_{ITO}\varepsilon_{Au}(\lambda)/(\varepsilon_{ITO}+\varepsilon_{Au}(\lambda))}$ and $k_{in} = (2\pi/\lambda)\sin\theta_i$ are the parallel components of the wave vector of the SPP and the incident plane wave, respectively. $\vec{G}_1 = (2\pi/L)\vec{x}$ and $\vec{G}_2 = (2\pi/L)\vec{y}$ represent the 2D reciprocal lattice grating basis vectors, m_x and m_y are integers corresponding to different diffraction orders. Eq. (2-5) can be simplified to obtain

$$\frac{1}{\lambda}\sqrt{\frac{\varepsilon_{ITO}\varepsilon_{Au}(\lambda)}{\varepsilon_{ITO}+\varepsilon_{Au}(\lambda)}} = \sqrt{(\frac{m_x}{L})^2 + (\frac{\sin\theta_i}{\lambda} + \frac{m_y}{L})^2}\,, \tag{2-6}$$

where λ is the wavelength of incident light and ε_{ITO} is the dielectric constant of ITO. TM polarization supports the same resonant wavelengths, due to the symmetries of our geometry. We have assumed the dielectric constant of ITO to be ~1.91ε_0, which is its bulk permittivity in the optical regime. We have also used experimental data for the Au permittivity.[30] To interpret our results, we examine the case of normal incidence in Figure 2.5(a)(b), where the local minimum originates from the grating modes (±1,0) and (0,±1). Since they are four-fold degenerate, this resonance is more pronounced compared with oblique incidence. As the incident angle becomes larger, mode (±1,0) (orange arrows) and (0,-1) (brown arrows) are no longer degenerate, so they gradually shift apart as predicted by Eq. (2-6). At large incident angles (θ_i > 40^o), the SPP resonant dip remains fixed at 700 nm, due to the anti-crossing of the SPP resonance with the dominant metasurface resonance, which is not affected by the incidence angle.

Further inspection of the SPP resonances in Figure 2.5 (a)(b) reveals that they are always accompanied by sharp transmission peaks, indicated by orange and brown circles.

These are associated with Wood's anomalies,[33] and can be described by replacing k_{SPP} with n_{sub}/λ in Eq.(2-6), where n_{sub} is the effective refractive index of the substrate. Our numerical and experimental results indicate that n_{sub} ~1.6, which is slightly higher than the refractive index of the bare ITO ($n_{ITO} = \sqrt{\varepsilon_{ITO}} \sim 1.4$), due to the influence of the Au layer. Similar to SPP-coupled grating modes, we observe a sharper Wood's anomaly peak at $\theta_i = 0^o$, caused by four-fold mode degeneracy compared with the spectra under non-normal incident light. The peak splits into two minor ones and they gradually move away from each other as we increase θ_i; anti-crossing behavior is observed when $\theta_i > 40^o$.

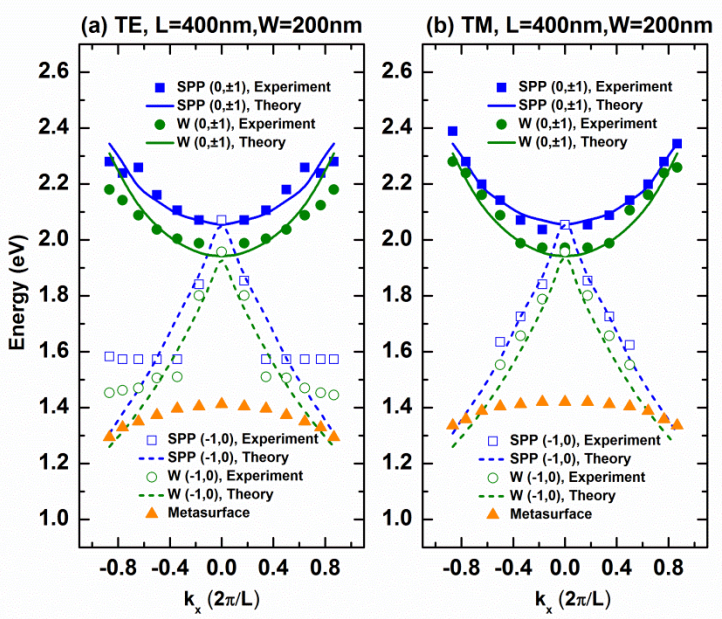

Figure 2.6: Band diagrams extracted from theoretical and measured spectral feature for SPP-coupled grating modes (SPP), Wood's anomaly (W), and metasurface resonances: (a) TE, L = 400 nm, W = 200 nm, (b) TM, L = 400 nm, W = 200 nm.

We summarize the behavior of the SPP-coupled grating modes, Wood's anomalies and metasurface resonances in the band diagrams shown in Figure 2.6. Generally, the

theory and experimental data are in excellent agreement for $\theta_i < 40^o$. In the range $\theta_i > 40^o$, the anti-crossing among the different bands shows some expected detuning, due to the dominant response of the metasurface resonance. As expected, the metasurface resonance shows a flat angular response, dominated by the metasurface element resonances, consistent with Eq. (2-6) and the previous discussions.

2.2.4 Conclusion

In conclusion, we have modeled, fabricated and characterized the optical transmission spectra of two-dimensional Au patch arrays. We have examined different periodicities, which determine the properties of the metasurface resonance and of SPP-coupled grating modes. The major difference between these two resonant phenomena consists in their sensitivity to the incident angle, due to the different underlying phenomena: the collective metasurfaces resonance is based on the plasmonic resonance of an individual metasurface element, and only weakly affected by the array coupling, whereas the SPP-coupled grating modes are lattice effects that are very sensitive to the incidence angle. High tolerance of incident angles and polarization in transmission and reflection of the metasurface resonance can be potentially useful for broad-angle energy harvesting applications such as plasmonic solar cell and for other devices, such as subwavelength plasmonic color filters.

2.3 DOUBLE-LAYER METASURFACE

In section 2.3, we discuss the design, experimental demonstration, and analysis of structures consisting of multiple layers of two-dimensional plasmonic arrays, with each individual layer constituting a subwavelength-scale metasurface.[14, 34] These structures are shown to provide high reflectivity and low transmittance at optical wavelengths across a bandwidth of ~100 nm that remains fixed under variations in angle of incidence from 0° to 30°. In this respect, these structures provide new functionality compared to more conventional optical components such as dichroic mirrors, which provide high reflectivity over a specific range of wavelengths but are highly sensitive to variations in angle of incidence.[4] Designs are demonstrated that provide either polarization-independent or polarization-sensitive optical behavior, as well as robustness to large variations in vertical alignment between metasurface layers. These behaviors are shown to be a consequence of plasmonic resonances in metal nanostructures that constitute the individual metasurface layers, interference effects between metasurface layers, scattering phase shifts at each metasurface, and the interplay among these phenomena.

2.3.1 Fabrication process of multilayer metasurface via e-beam lithography

Figure 2.7 shows the key fabrication processes of a multilayer metasuface structure. (a) A set of alignment marks with Cr (5 nm)/Au (30 nm) were defined via electron-beam lithography. (b) The first layer of metasurface was created by electron-beam lithography and followed by deposition of Ge (2 nm)/Ag (30 nm) using electron-beam evaporation. (c) The first layer of metasurface was planarized by spin-on glass with different dilution to control the thickness. The entire structure is then baked for 2 hours to remove solvents from spin-on glass. (d) The second layer of metasurface is defined by electron-beam lithography with reference to the alignment marks of the first layer.

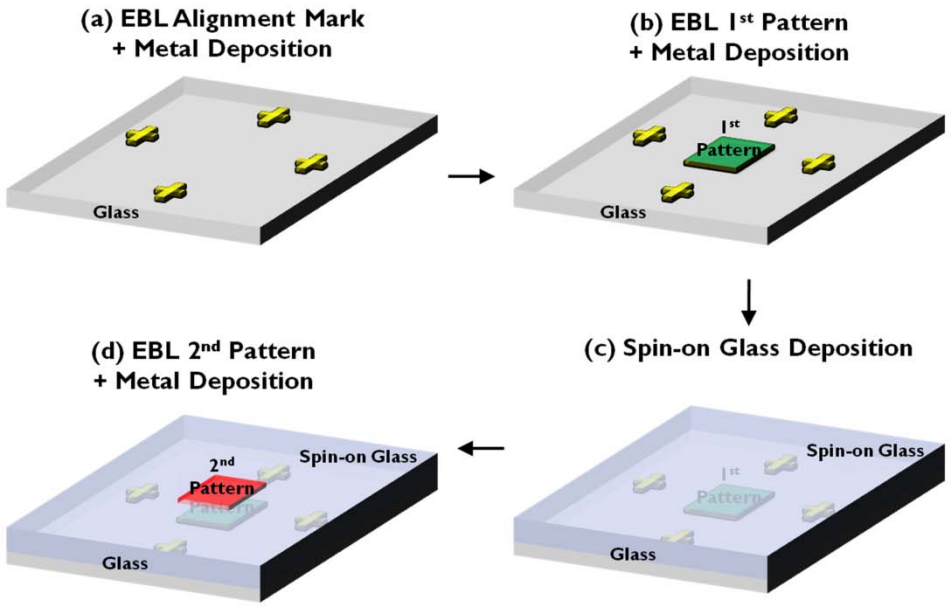

Figure 2.7: Key fabrication process of a multilayer metasurface.

2.3.2 Metasurface resonance

Figure 2.8 shows schematic diagrams and scanning electron micrographs of the multilayer metasurface structures employed in these studies, along with the measurement geometries for transverse electric (TE) and transverse magnetic (TM) polarizations. All structures were fabricated on 0.5 mm thick glass substrates (CoreSix) polished to yield a surface roughness of 0.5 nm. The individual Ag elements consist of 30 nm high square patches of side length W, and for each metasurface layer these are arranged in a square array of period *L*. Between individual metasurface layers, the sample structure is planarized using a spin-on glass whose thickness, *D*, is controlled via dilution of the spin-on-glass solution and spin coating speed. For a structure containing two metasurface layers with structure (side length and array period) given by W_1, L_1 and W_2, L_2, respectively, the alignment between the individual metasurfaces is characterized by S_x,

and S_y, as indicated in Figure 2.8. Since the periods of each metasurface layer are related by a rational multiple N/M, i.e., $NL_1 = ML_2$, we define the translational offsets in the plane of the metasurface, S_x, and S_y, to be the minimum distances in the x- and y-directions, respectively, that one metasurface layer would have to be shifted such that the centers of individual array elements spaced by $NL_1 = ML_2$ are perfectly aligned.

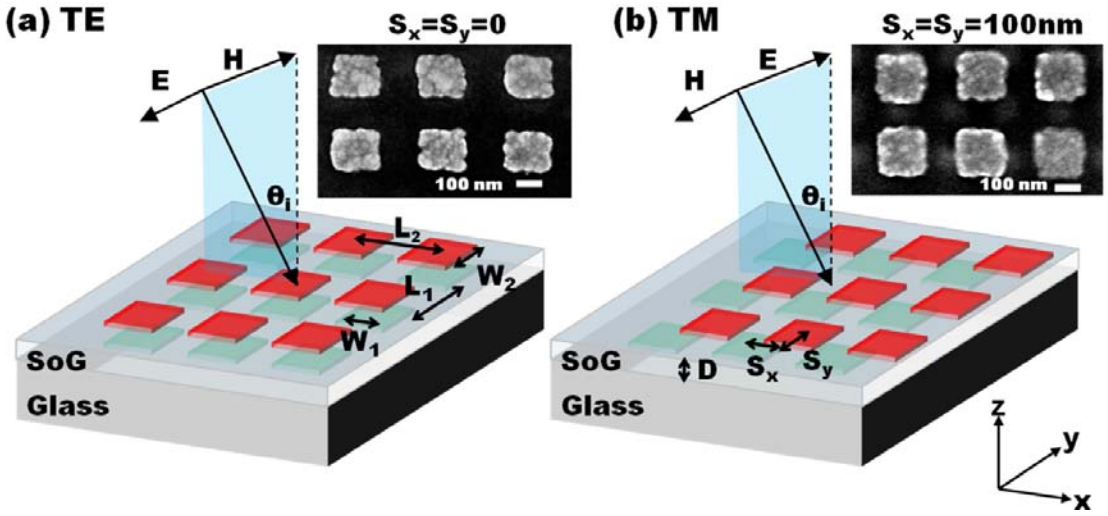

Figure 2.8: A schematic diagram of the multilayer metasurface structure on a glass substrate under (a) TE and (b) TM polarized illumination respectively. L_1, W_1 and L_2, W_2 indicate the periodicity of the array and size of the individual metallic nanostructures for the bottom and top metasurface layers, respectively. The translational alignment parameters S_x and S_y are indicated in (b). The insets show the scanning electron micrographs of an aligned (S_x = S_y = 0), and shifted (S_x = S_y = 100 nm). The scale bars are 100 nm.

Previous work has shown that a single-layer plasmonic metasurface structure can provide low optical transmittance, due to the excitation of plasmonic resonances within individual metasurface elements, over a narrow range of wavelengths that remains fixed over angles of incidence ranging from 0° to approximately 60° off normal.[35] Figure 2.8 (a)(b) shows optical transmittance measured for a single-layer metasurface structure

consisting of 100 nm × 100 nm × 30 nm Ag patches (i.e., W = 100 nm) arranged in a square array with period L=200nm, as a function of wavelength, angle of incidence, and polarization of incident light. Figure 2.8(c)(d) shows the same quantities for a second single-layer metasurface structure consisting of a square array of 30nm high Ag patches with W = 170 nm and L = 300 nm. As illustrated in the figures, the single-layer metasurfaces produce a minimum in transmittance coinciding approximately with the plasmonic resonance wavelengths in the individual Ag patches. For the metasurface with W = 100 nm and L = 100 nm [Figure 2.9 (a)(b)], the transmittance is very weakly dependent on incident angle θ_i over the range θ_i = 0°-60°. For the structure with W = 170 nm and L = 300 nm [Figure 2.9 (c)(d)], the minimum in transmittance is shifted to slightly longer wavelengths due to the larger size of the individual Ag structures, and local peaks in transmittance appear at wavelengths near the plasmonic resonance wavelength due to Wood's anomaly and coupling to surface plasmon modes.[35]

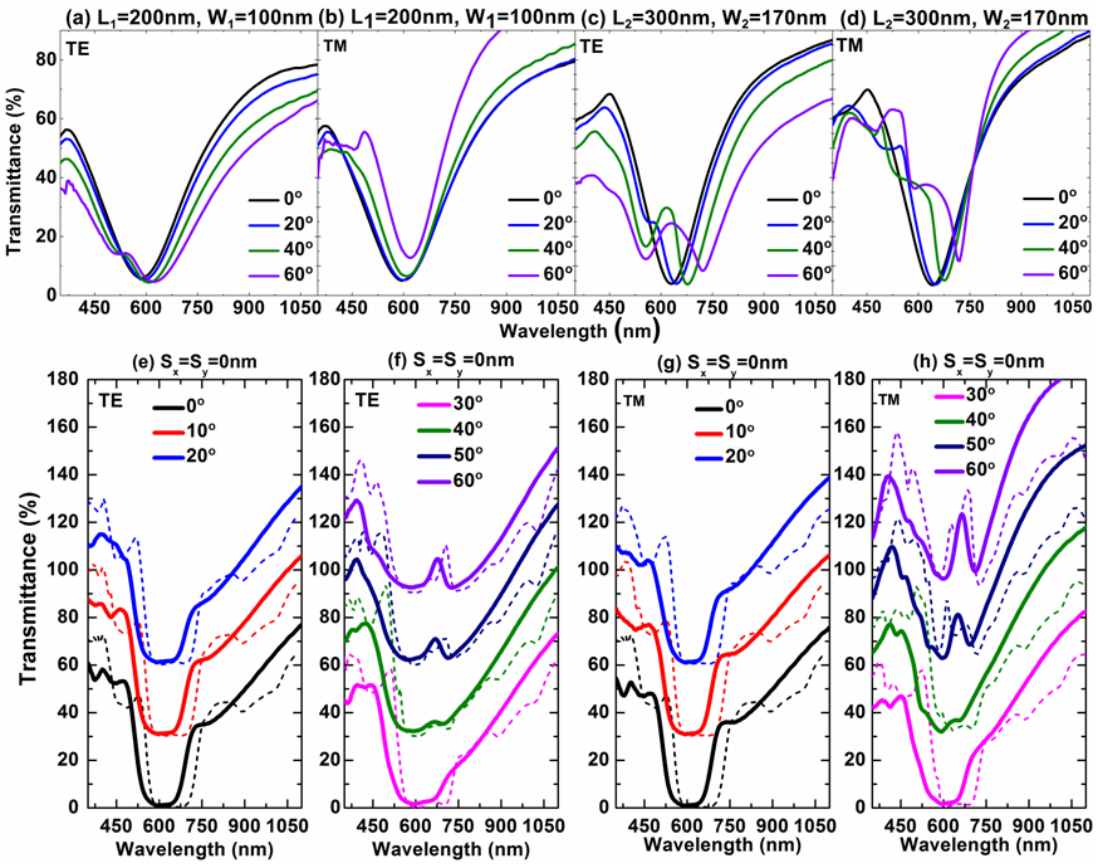

Figure 2.9: (a)(b)(c)(d) Measured transmission spectra for L_1 = 200 nm, W_1 = 100 nm, and L_2 = 300 nm, W_2 = 170 nm single layer metasurfaces under TE and TM polarized illumination, respectively. (e)(f)(g)(h) Measured (solid lines) and simulated (dashed lines) transmission spectra for an aligned multilayer metasurface structure, L_1 = 200 nm, W_1 = 100 nm, L_2 = 300 nm, W_2 = 170 nm, D = 350 nm, and S_x = S_y = 0 under TE and TM polarized light respectively.

Figure 2.9 (e)(h) shows measured and numerically simulated optical transmittance spectra for an aligned (S_x = S_y = 0) multilayer structure consisting of a lower metasurface with W_1 = 100 nm and L_1 = 200 nm, an upper metasurface with W_2 = 170 nm and L_2 = 300 nm, and a spin-on glass layer of thickness D=350nm separating the two metasurface layers. The measured and numerically simulated transmittance spectra are in excellent agreement, and demonstrate that the multilayer structure is able to produce a deep, broad

minimum in transmittance – transmittance < 1% over wavelengths from 550 nm to 650 nm – for both TE and TM polarizations and for angles of incidence θ_i from 0° to 30°. For angles of incidence from 0° to 20°, the transition to high optical transmittance (30-50% or greater) occurs over a narrow wavelength range – ~30-50 nm – at both shorter and longer wavelengths. For incident angles of 30° or greater, a local maximum in transmittance begins to appear at ~650 nm, and becomes more prominent as θ_i increases. Simulated reflectance, transmittance, and absorption spectra as functions of wavelength, polarization, and incident angle indicate that reflectance within the low transmittance band is > 75%.

2.3.3 Fabry-Perot resonance

Detailed numerical simulations provide insight into the origin of these behaviors, and into opportunities to engineer specific optical properties and realize designs that are robust to variations and imperfections that are most likely to arise in practical manufacturing processes. Figure 2.10 shows numerically simulated transmittance spectra under TE-polarized illumination for a multilayer structure containing two metasurfaces with W_1 = 100 nm, L_1 = 200 nm and W_2 = 170 nm, L_2 = 300 nm, separated by a spin-on glass dielectric layer with thickness D ranging from 40 nm to 600 nm. The layers are vertically aligned. In Figure 2.10 (a), corresponding to normally incident illumination ($\theta_i = 0^o$), we observe that there is a deep minimum in transmittance extending approximately from 550 nm to 650nm that is present for all values of D. The wavelength boundaries of this region are modulated due to the presence of local peaks in transmittance, corresponding approximately to the solid lines in the figure, that occur at specific wavelengths for a given value of metasurface layer separation D. These transmittance peaks can be interpreted as arising from Fabry-Perot resonances created by the

reflectance and transmittance properties of each metasurface, appropriately modified to account for the wavelength-dependent phase shift produced by each.

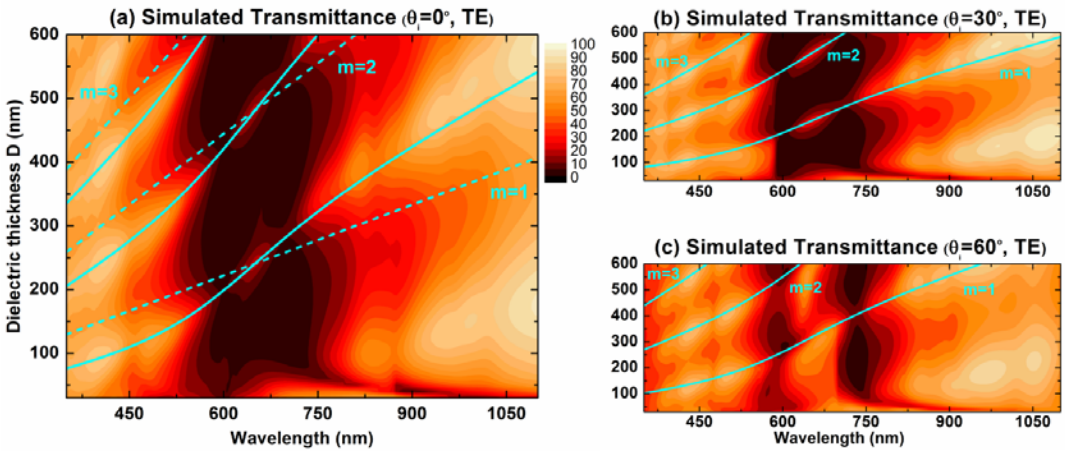

Figure 2.10: Simulated transmittance spectra, as function of wavelength and dielectric layer thickness D for a multilayer metasurface structure with L_1 = 200 nm, W_1 = 100 nm, L_2 = 300 nm, W_2 = 170 nm, and $S_x = S_y = 0$ for (a) $\theta_i = 0^o$, (b) $\theta_i = 30^o$, and (c) $\theta_i = 60^o$ under TE polarized light. The solid and dashed lines represent Fabry-Perot resonance wavelengths as given by Eq. (3) with and without, respectively, inclusion of the metasurface phase shift given by Eq. (2-8).

For conventional Fabry-Perot resonances, the wavelengths at which peaks in optical transmittance through a dielectric cavity of thickness D would occur are given by

$$\lambda = \frac{2n_d}{m} D, \tag{2-7}$$

where m is a positive integer corresponding to different cavity modes, nd is the refractive index of the dielectric material, and λ is the wavelength in free space. The Fabry-Perot resonant wavelengths given by Eq. (2-7) with n_d and D taken to be the refractive index and thickness, respectively, of the spin-on glass, are indicated by the dashed lines in Figure 2.10 (a), revealing that this expression provides at best a very approximate estimate of the wavelengths at which such resonances occur in the multilayer metasurface

structure. Much better agreement is obtained by accounting for the wavelength-dependent phase shift incurred upon interaction of light with the metasurface layers.[36-37] Specifically, the total wavelength-dependent phase shift produced by the two metasurfaces is given approximately by[37]

$$\varphi(\lambda) \approx \tan^{-1}\left[\frac{2\pi c}{\gamma}\left(\frac{1}{\lambda}-\frac{1}{\lambda_r}\right)\right], \tag{2-8}$$

where γ is a phenomenological damping constant obtained by fitting to transmittance or reflectance spectra, and λ_r is the resonance wavelength in the multilayer metasurface structure. Given this phase shift, and following a recently developed approach for analysis of refraction in the presence of phase shifts,[34] the Fabry-Perot resonance condition is modified from that given by Eq. (2-7) to become

$$\lambda = \frac{2\sqrt{n_d^2 - \sin^2\theta_i}}{m - \varphi(\lambda)/\pi} D, \tag{2-9}$$

where $\phi(\lambda)$ is given by Eq. (2-8). The solid lines in Figure 2.10 (a) are the Fabry-Perot resonant wavelengths given by Eq. (2-9) with n_d and D taken to be the refractive index and thickness, respectively, of the spin-on glass, and with γ = 3×105 s^{-1} and λ_r = 650 nm determined by fitting to the computed transmittance spectra. We see that agreement between the Fabry-Perot resonant wavelengths computed using Eq. (2-9) and the transmittance peaks present in Figure 2.10 (a) is excellent. Figure 2.10 (b) and (c) show numerically simulated transmittance spectra and Fabry-Perot resonant wavelengths computed using Eq. (2-9) for incident angles of 30° and 60°. Once again, excellent agreement is observed between the resonant wavelengths computed using Eq. (2-9) and the peaks observed in the numerically simulated transmittance spectra, providing clear evidence of the role of metasurface phase shifts in influencing optical transmittance in these structures.

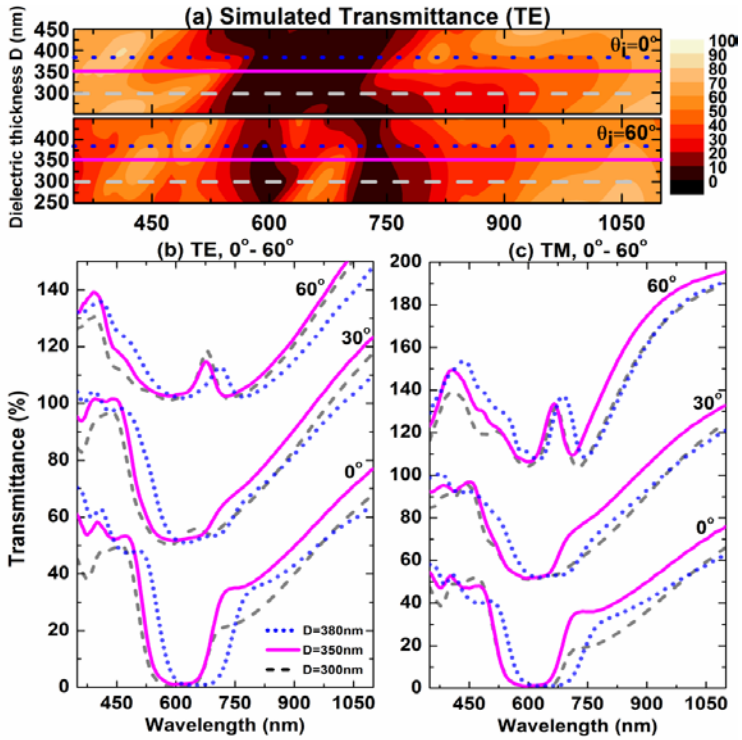

Figure 2.11: (a) Simulated transmittance spectra for θ_i = 0° and θ_i = 60° under TE polarization. Dashed, solid, and dotted lines correspond to dielectric layer thicknesses D=300nm, 350nm, and 380nm, respectively. (b)(c) Measured transmittance spectra for multilayer metasurface structures with L_1 = 200 nm, W_1 = 100 nm, L_2 = 300 nm, W_2 = 170 nm, S_x = S_y = 0 and D = 300 nm, 350 nm, and 380 nm, following the same plot scheme as in (a), under TE or TM polarization, respectively. In parts (b) and (c), transmittance spectra at different incident angles have been offset vertically by 50% each for clarity.

The existence of transmittance peaks associated with phase-dependent Fabry-Perot resonances in multilayer metasurface structures offers an opportunity to optimize the wavelength sensitivity of transmittance via judicious selection of the thickness D of the spin-on glass layer. Figure 2.11 (a) shows numerically simulated transmittance spectra for multilayer metasurface structures with W_1 = 100 nm, L_1 = 200 nm, W_2 = 170 nm, L_2 = 300 nm, D = 250-450 nm, and S_x = S_y = 0, for light incident with TE polarization. While a broad transmittance minimum is present over the entire range of

values of D shown, the positioning of the Fabry-Perot resonance transmission peaks at the edges of this transmittance minimum for $D \approx$ 300-380 nm allows D to be used a tuning parameter to produce (a) higher-contrast transitions with wavelength between low and high transmittance, and (b) moderate shifts in the center wavelength of the transmittance minimum. These trends are confirmed in experimental measurements. Figure 2.11 (b) and (c) show measured transmittance spectra for multilayer metasurface structures with W_1 = 100 nm, L_1 = 200 nm, W_2 = 170 nm, L_2 = 300 nm, and D = 300 nm, 350 nm, and 380 nm. The layers are vertically aligned, with $S_x = S_y = 0$. Measurements for angles of incidence of 0° and 30°, and for both TE and TM polarization, are shown. The positioning of the Fabry-Perot transmittance peak at ~700nm for D = 350 nm and D = 380 nm leads to a substantial increase in contrast between the low- and high-transmittance regions of the measured spectra on either side of the transmittance peak. Furthermore, the shift in position of the Fabry-Perot transmittance peak between D = 350 nm and D = 380 nm allows the center wavelength of the transmittance minimum to be shifted by ~50 nm while maintaining a fixed bandwidth of ~100 nm.

The existence of transmittance peaks associated with phase-dependent Fabry-Perot resonances in multilayer metasurface structures offers an opportunity to optimize the wavelength sensitivity of transmittance via judicious selection of the thickness D of the spin-on glass layer. Figure 2.11 (a) shows numerically simulated transmittance spectra for multilayer metasurface structures with W_1 = 100 nm, L_1 = 200 nm, W_2 = 170 nm, L_2 = 300 nm, D = 250-450 nm, and $S_x = S_y = 0$, for light incident with TE polarization. While a broad transmittance minimum is present over the entire range of values of D shown, the positioning of the Fabry-Perot resonance transmission peaks at the edges of this transmittance minimum for $D \approx$ 300-380 nm allows D to be used a tuning parameter to produce (a) higher-contrast transitions with wavelength between low

and high transmittance, and (b) moderate shifts in the center wavelength of the transmittance minimum. These trends are confirmed in experimental measurements. Figure 2.11 (b) and (c) show measured transmittance spectra for multilayer metasurface structures with W_1 = 100 nm, L_1 = 200 nm, W_2 = 170 nm, L_2 = 300 nm, and D = 300 nm, 350 nm, and 380 nm. The layers are vertically aligned, with $S_x = S_y = 0$. Measurements for angles of incidence of 0° and 30°, and for both TE and TM polarization, are shown. The positioning of the Fabry-Perot transmittance peak at ~700 nm for D = 350 nm and D = 380 nm leads to a substantial increase in contrast between the low- and high-transmittance regions of the measured spectra on either side of the transmittance peak. Furthermore, the shift in position of the Fabry-Perot transmittance peak between D = 350 nm and D = 380 nm allows the center wavelength of the transmittance minimum to be shifted by ~50nm while maintaining a fixed bandwidth of ~100 nm.

2.3.4 Robustness against interlayer misalignment

Vertical alignment of nanoscale features is often a key concern in design and fabrication of multilayer or three-dimensional nanostructures. For applications requiring fabrication at low cost or over large areas, it would be highly desirable to design structures whose performance characteristics are robust to variations in vertical alignment. Because their properties depend primarily on plasmonic resonant phenomena in individual metallic nanostructures, and because interactions between these individual elements in the vertical direction do not play a significant role, the multilayer metasurface structures presented here are extremely robust to even large variations in vertical alignment, i.e., values of S_x and S_y that are substantial fractions of W or L for the individual metasurface layers. Figure 2.12 shows numerically simulated and measured optical transmittance spectra for a multilayer metasurface structure with W_1 = 100 nm, L_1

= 200 nm, W_2 = 170 nm, L_2 = 300 nm, D = 380 nm, and $S_x = S_y$ = 100 nm. We note that this is the maximum translational misalignment, relative to $S_x = S_y = 0$, that can occur for this structure. Despite this misalignment, the measured optical transmittance spectra are nearly identical to those of the corresponding structure with $S_x = S_y = 0$ shown in Figure 2.11 (b) and (c). Further simulations for translation misalignments ($S_x = S_y$ = 0 to 100 nm) also confirm our experimental results.

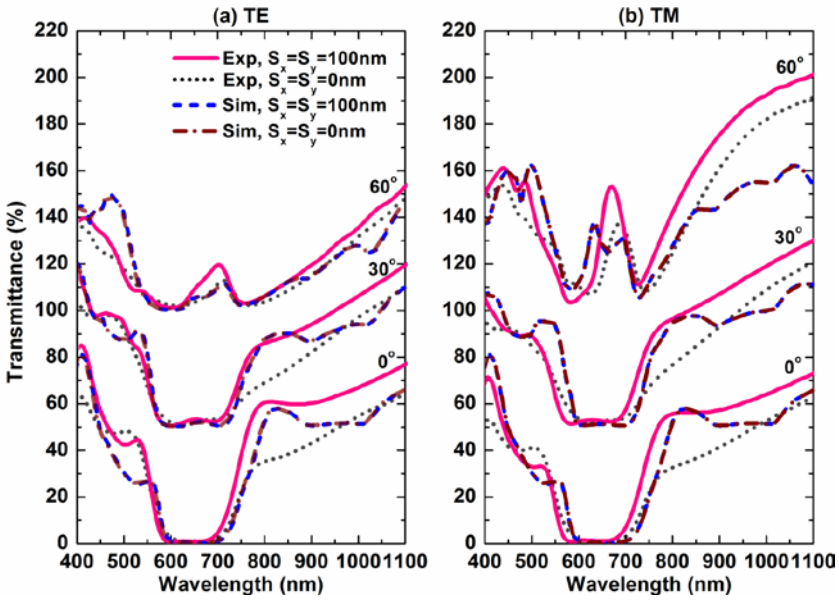

Figure 2.12: Measured and simulated transmission spectra for a multilayer metasurface structure with L_1 = 200 nm, W_1 = 100 nm, L_2 = 300 nm, W_2 = 170 nm, D = 380 nm, and $S_x = S_y$ = 100 nm or $S_x = S_y = 0$ for different θ_i under (a) TE or (b) TM polarization. Transmittance spectra at different incident angles have been offset vertically by 50% each for clarity.

2.3.5 Conclusion

In summary, we have designed, experimentally demonstrated, and analyzed both numerically and analytically a series of multilayer plasmonic metasurface structures that provide wide-angle, wavelength-selective, polarization-independent optical transmittance

and reflectance with performance that is robust to even severe vertical misalignment between individual plasmonic metasurface arrays constituting the complete multilayer structure. These characteristics are shown to be a consequence of high reflectivity associated with plasmonic resonances in each metasurface layer, phase shifts induced by interaction of light with the metasurfaces, and phase-dependent Fabry-Perot resonances associated with the multilayer stack. The insensitivity of the wavelength-dependent optical reflectance and transmittance to polarization and angle of incidence suggest potential use of these types of structures for a broad range of applications. Robustness to severe vertical misalignment between individual layers in a multilayer structure suggests that these structures can be highly amenable to low-cost, high-throughput fabrication processes.

2.4 FLEXIBLE, LARGE-AREA, LOW-LOSS MULTILAYER METASURFACE

In section 2.4, flexible, low-loss, large-area multilayer plasmonic optical metasurfaces are demonstrated and analyzed that provide wavelength-selective reflectance > 95% and transmittance < 1% with low absorption and robustness to variation in angle of incidence and polarization. These characteristics are shown to be insensitive to vertical misalignment between layers, and defects within individual layers. Analysis based on analytical modeling and numerical simulations provides physical insights into reflectance, loss, and bandwidth of these multilayer metasurface structures. Fabry-Perot resonances associated with phase shifts from each individual metasurface are also examined, and evidence of m = 0 resonance due to the nonzero, wavelength dependent phase shift from the metasurface cavity is demonstrated and explained. Finally, fabrication on flexible substrates via rapid, large-area nanosphere lithography and the robustness of optical properties of interlayer misalignment together enable the demonstration of wavelength-selective focusing at optical frequencies.

2.4.1 Transfer matrix method for modeling multilayer metasurface

2.4.1.1 Assumptions and derivations

The inhomogenous wave equation can be derived from Maxwell's equations as[38-40]

$$[\nabla^2 - \frac{1}{c^2}\frac{\partial^2}{\partial t^2}]\vec{E}(r,t) = \mu_0 \frac{\partial^2}{\partial t^2}\vec{P}(r,t) - \frac{1}{\varepsilon_0}\nabla(\nabla \cdot \vec{P}(r,t)), \qquad (2\text{-}10)$$

where $\vec{P} = \vec{P}_{meta} + \vec{P}_d$ consists of the polarization of the metasurface, $\vec{P}_{meta}$ and the dielectric layer, $\vec{P}_d$ .Typical dielectric layers we used for stacking multilayer structures are non-resonant and homogenous at the wavelengths of interest, so that $\vec{P}_d$ can be simplified as $\vec{P}_d(r,t) = \chi_d \vec{E}(r,t)$, where the susceptibility can be described with the refractive index of the dielectric layer, $n_d^2 = 1 + \chi_d / \varepsilon_0$.

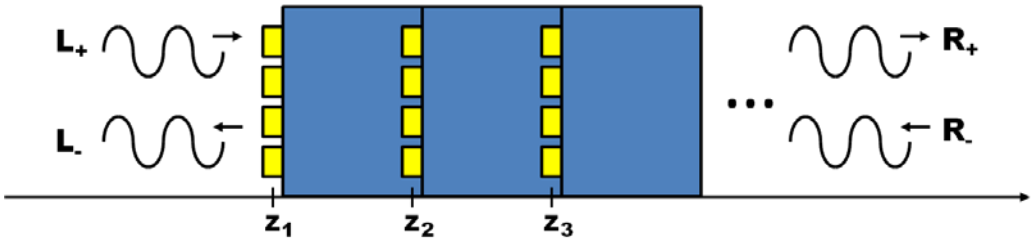

Figure 2.13: The schematic of the multilayer metasurface structure. The position of Nth layer metasurface is denoted as z_N, and the amplitude of the reflected and transmitted electric field on the left hand side are denoted as L_+, and L_-.

The second term of Eq. (2-10) on the right hand side is related to the longitudinal part of the field. Here, we are only interested in light propagating orthogonally to the multilayer structure, and Eq. (2-10) can then be simplified to

$$[\frac{\partial^2}{\partial z^2}-\frac{n_d^2}{c^2}\frac{\partial^2}{\partial t^2}]\vec{E}(r,t)=\mu_0\frac{\partial^2}{\partial t^2}\vec{P}_{meta}(r,t). \tag{2-11}$$

Since the metasurface is optically thin ($\lambda >> d$ with d typically ~40 nm), so that we simply assume $\vec{P}_{meta}=\chi(\omega)\vec{E}(z_1,\omega)\delta(z-z_1)$ is localized to the position of the metasurface, z_1. Eq. (2-11) can then be simplified as:

$$[\frac{\partial^2}{\partial z^2}+\frac{n_d^2\omega^2}{c^2}]E(z,\omega)=-\mu_0\omega^2\chi(\omega)E(z_1,\omega)\delta(z-z_1), \tag{2-12}$$

The typical homogenous solution for the electric field on either side of the metasurface can be written as,

$$E_L(z,\omega)=L_+e^{ikn_dz}+L_-e^{-ikn_dz}, \text{ for } z<z_1 \tag{2-13}$$

$$E_R(z,\omega)=R_+e^{ikn_dz}+R_-e^{-ikn_dz}, \text{ for } z>z_1. \tag{2-14}$$

Using proper boundary conditions appropriate for the metasurface represented as a Dirac delta function, we obtain

$$E_L(z_1,\omega)=E_R(z_1,\omega), \tag{2-15}$$

$$E_L'(z_1,\omega)+I=E_R'(z_1,\omega), \tag{2-16}$$

where $I = -\mu_0 \omega^2 \chi(\omega) E(z_1, \omega)$. The transfer matrix of a metasurface, $\hat{M}_{meta}$,can be derived by connecting coefficients,

$$\begin{bmatrix} R_+ \\ R_- \end{bmatrix} = \hat{M}_{meta} \begin{bmatrix} L_+ \\ L_- \end{bmatrix}. \tag{2-17}$$

For a single layer metasurface, $\hat{M}_{meta}$ can be written as,

$$\hat{M}_{meta} = \begin{bmatrix} 1+X & Xe^{-2ikn_d z_1} \\ Xe^{2ikn_d z_1} & 1-X \end{bmatrix}, \tag{2-18}$$

with $X = i(k/2\varepsilon_0 n_d)\chi(\omega)$. The transmission and reflection coefficient, $t = R_+/L_+$ and $r = L_-/L_+$, can be derived by solving,

$$\begin{bmatrix} t \\ 0 \end{bmatrix} = \hat{M}_{meta} \begin{bmatrix} 1 \\ r \end{bmatrix}, \tag{2-19}$$

and that leads to

$$r = -\frac{M_{21}}{M_{22}} = \frac{X}{1-X} e^{2ikn_d z_1}, \tag{2-20}$$

$$t = \frac{M_{11}M_{22} - M_{12}M_{21}}{M_{22}} = \frac{1}{1-X}. \tag{2-21}$$

For a multilayer metasurface structure as shown in Figure 2.13, Eq. (2-19) can be expressed as,

$$\begin{bmatrix} t \\ 0 \end{bmatrix} = \hat{M}^N_{meta} \hat{M}^{N-1}_{meta} \cdot \ldots \cdot \hat{M}^2_{meta} \hat{M}^1_{meta} \begin{bmatrix} 1 \\ r \end{bmatrix}, \tag{2-22}$$

where $\hat{M}^N_{meta}$ is the transfer matrix for the Nth metasurface. The corresponding *r* and *t* can be calculated based on Eq. (2-20) and (2-21).

2.4.1.2 Analytical solutions of multilayer metasurface under Bragg condition

The effective susceptibility for a single metasurface layer can be modeled as[38, 41]

$$\chi(\lambda) = -\frac{\Gamma(\lambda_r/\lambda)}{hc/\lambda - hc/\lambda_r + i\gamma}, \tag{2-23}$$

where h is Planck's constant, c is the speed of light, Γ is the radiative linewidth, γ is the nonradiative linewidth, and λ_r is the resonant wavelength (~605nm). Γ and γ are determined from the experimental full width half maximum (FWHM) and reflectance of the single layer structure. γ is usually small and can be ignored. Γ is associated with the strength and linewidth of the oscillator, higher Γ is usually accompanied with higher bandwidth and oscillation amplitude.

The reflectance and transmittance can be derived from Eq. (2-20) and (2-21):

$$R = |r|^2 = \frac{\Gamma^2}{(hc/\lambda - hc/\lambda_r)^2 + (\gamma + \Gamma)^2}, \tag{2-24}$$

$$T = |t|^2 = \frac{(hc/\lambda - hc/\lambda_r)^2 + \gamma^2}{(hc/\lambda - hc/\lambda_r)^2 + (\gamma + \Gamma)^2}, \tag{2-25}$$

and Γ and γ can be fitted by,

$$\Gamma = \frac{FWHM}{2}\sqrt{R_{\max}}, \tag{2-26}$$

$$\gamma = \frac{FWHM}{2}[1 - \sqrt{R_{\max}}]. \tag{2-27}$$

For a structure with P = 200 nm, D = 160 nm, d = 40 nm, h = 10 nm, the experimental results yield Γ = 0.513 eV, and γ =0.0794 eV. Figure 2.14 (a) shows analytical results demonstrating that the resonant peaks in reflectance and absorption coincide with the dip in transmittance. The absorption at the resonant wavelength (~605nm) is ~25%.

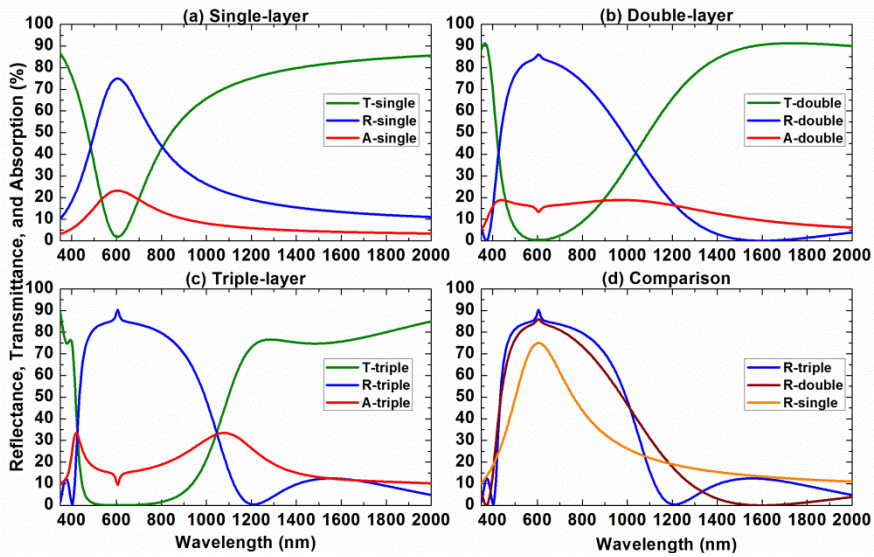

Figure 2.14: The calculated reflectance, transmittance, and absorption under normal incidence based on transfer matrix of (a) single layer, (b) double layer (c) triple layer. (d) The reflectance comparison between single, double, and triple layer.

The transfer matrix for a double layer metasurface structure, $M^{(2)}$, can be calculated by,

$$M^{(2)} = \begin{bmatrix} 1+X & Xe^{-2ikn_d z_1} \\ Xe^{2ikn_d z_1} & 1-X \end{bmatrix} \begin{bmatrix} 1+X & Xe^{-2ikn_d z_2} \\ Xe^{2ikn_d z_2} & 1-X \end{bmatrix}, \tag{2-28}$$

where $z_1 = \lambda_r / 2n_d$ and $z_2 = \lambda_r / n_d$ are the positions of the metasurface layers and the thickness of the interlayer dielectric is $H + h = \lambda_r / 2n_d$. The matrix elements can be calculated as

$$M_{11}^{(2)} = (1+X)^2 - X^2 e^{-2i\pi(\lambda_r/\lambda)}, \tag{2-29}$$

$$M_{12}^{(2)} = (1+X)Xe^{-2i\pi(\lambda_r/\lambda)} + (1-X)Xe^{-4i\pi(\lambda_r/\lambda)}, \tag{2-30}$$

$$M_{21}^{(2)} = -(1+X)Xe^{4i\pi(\lambda_r/\lambda)} - (1-X)Xe^{2i\pi(\lambda_r/\lambda)}, \tag{2-31}$$

$$M_{22}^{(2)} = -X^2 e^{2i\pi(\lambda_r/\lambda)} + (1-X)^2, \tag{2-32}$$

and the reflectance and transmittance, *R* and *T*, can be calculated, respectively. Figure 2.14 (b) shows the analytical results for reflectance, transmittance, and absorption. The

reflectance is significantly broadened compared with that for a single layer, and a small additional peak is superimposed at 605 nm due to Bragg criterion.

The transfer matrix, $M^{(3)}$, can be calculated by

$$M^{(3)} = \begin{bmatrix} 1+X & Xe^{-2ikn_d z_1} \\ Xe^{2ikn_d z_1} & 1-X \end{bmatrix} \begin{bmatrix} 1+X & Xe^{-2ikn_d z_2} \\ Xe^{2ikn_d z_2} & 1-X \end{bmatrix} \begin{bmatrix} 1+X & Xe^{-2ikn_d z_3} \\ Xe^{2ikn_d z_3} & 1-X \end{bmatrix}, \quad (2\text{-}33)$$

and the corresponding matrix elements with $z_1 = \lambda_r / 2n_d$, $z_2 = \lambda_r / n_d$, $z_3 = 3\lambda_r / 2n_d$, and $H + h = \lambda_r / 2n_d$ can be shown as,

$$M_{11}^{(3)} = (1+X)^3 - (1+X)X^2 e^{-2i\pi(\lambda_r/\lambda)} - (1+X)X^2 e^{-2i\pi(\lambda_r/\lambda)} - (1-X)X^2 e^{-4i\pi(\lambda_r/\lambda)}, \quad (2\text{-}34)$$

$$M_{12}^{(3)} = (1+X)^2 Xe^{-2i\pi(\lambda_r/\lambda)} - (1-X)^2 Xe^{-4i\pi(\lambda_r/\lambda)} - X^3 e^{-4i\pi(\lambda_r/\lambda)} + (1-X)X^2 e^{-6i\pi(\lambda_r/\lambda)}, \quad (2\text{-}35)$$

$$M_{21}^{(3)} = -(1+X)^2 Xe^{6i\pi(\lambda_r/\lambda)} + X^3 e^{4i\pi(\lambda_r/\lambda)} - (1-X^2)Xe^{4i\pi(\lambda_r/\lambda)} - (1-X)^2 Xe^{2i\pi(\lambda_r/\lambda)}, \quad (2\text{-}36)$$

$$M_{22}^{(3)} = -(1+X)X^2 e^{4i\pi(\lambda_r/\lambda)} - (1-X)X^2 e^{-4i\pi(\lambda_r/\lambda)} - (1-X)X^2 e^{2i\pi(\lambda_r/\lambda)} + (1-X)^3, \quad (2\text{-}37)$$

and the reflectance and transmittance, *R*, and *T*, can be calculated from Eqs. (2-24)(2-25). Figure 2.14 (c) shows the analytical results for reflectance, transmittance and absorption. The FWHM remains relatively unchanged compared to the double-layer structure, suggesting that the optimum or near-optimum performance can be achieved with *N* as small as two. The local peak at 605 nm also becomes more prominent compared with double layer.

The position of *N*th metasurface can be expressed as $z_N = N(\lambda_r / 2n_d)$, and if the resonance of the metasurface is narrow. The reflectance and transmittance near the λ_r can be simplified as,

$$R = |r|^2 = \frac{(N\Gamma)^2}{(hc/\lambda - hc/\lambda_r)^2 + (\gamma + N\Gamma)^2}, \quad (2\text{-}38)$$

$$T = |t|^2 = \frac{(hc/\lambda - hc/\lambda_r)^2 + \gamma^2}{(hc/\lambda - hc/\lambda_r)^2 + (\gamma + N\Gamma)^2}, \quad (2\text{-}39)$$

Eq. (2-38) and (2-39) suggest that the peak reflectance can be enhanced by stacking multiple layers at Bragg criterion, therefore reducing the absorption.

2.4.1.3 Photonic bandgap

As *N* increases, the FWHM behavior of the multilayer structure will approach that of a 1D photonic crystal with unity reflectance within the photonic bandgap, and it can be estimated using the transfer matrix approach as [42]

$$E_r - \sqrt{\frac{2\Gamma E_r}{\pi}} < E < E_r + \sqrt{\frac{2\Gamma E_r}{\pi}}, \tag{2-40}$$

which can be rearranged as

$$\frac{1}{\frac{1}{\lambda_r} + \sqrt{\frac{2\Gamma}{\pi hc}(\frac{1}{\lambda_r})}} < \lambda < \frac{1}{\frac{1}{\lambda_r} - \sqrt{\frac{2\Gamma}{\pi hc}(\frac{1}{\lambda_r})}}. \tag{2-41}$$

2.4.1.4 Fabry-Perot resonance

Fabry-Perot resonance will occur between the individual metasurface layers due to constructive interference of waves, and the resonance condition can be calculated by [37, 43]

$$\lambda = \frac{2\sqrt{n_d^2 - \sin^2\theta_i}}{m - \phi(\lambda)/\pi}(H + h), \tag{2-42}$$

where the phase shift, $\phi(\lambda)$, resulting from the metasurface is given by

$$\phi(\lambda) = \tan^{-1}(\frac{\mathrm{Im}(r)}{\mathrm{Re}(r)}) = \tan^{-1}[hc\frac{(1/\lambda - 1/\lambda_r)}{\Gamma + \gamma}]. \tag{2-43}$$

2.4.2 Fabrication process of multilayer metasurface via nanosphere lithography

Figure 2.15 (a) shows a schematic diagram of a two-layer metasurface structure, the measurement geometry employed for transverse electric (TE) and transverse magnetic (TM) polarizations, and a scanning electron microscope (SEM) image of a completed structure. As indicated in the figure, individual metallic elements of diameter *D* and

thickness *d* that constitute each metasurface layer are arranged in a hexagonal array with center-to-center spacing *P* between adjacent elements. A SiO_2 layer of thickness *h* is present below each hexagonal array layer, and an SU-8 layer of thickness *H* is present between successive metasurface layers. All structures were fabricated on polyethylene terephthalate (PET) films (Dupont Melinex 454). Key steps in the fabrication process for each metasurface layer are shown in Figure 2.15 (b)-(d). First, 10nm SiO_2/100 nm liftoff resist (LOR)/10nm SiO_2 are deposited. The two layers of SiO_2 were deposited in separate e-beam evaporation processes. A self-assembled monolayer of 200 nm-diameter polystyrene (PS) spheres is then deposited on the SiO_2 surface using the Langmuir-Blodgett method,[44-45] as shown in Figure 2.15 (b). Reactive ion etching (RIE) is then used to etch the PS spheres, thereby reducing their diameter to ~160nm, after which 20 nm Cr is deposited by e-beam evaporation. The nanospheres are then removed by a lift-off process in toluene, resulting in formation of a Cr hard mask consisting of a hexagonal array of holes, within which the underlying LOR/SiO_2 layers are removed by RIE, resulting in the structure shown in Figure 2.15 (c). Finally, 5 nm Ge/40 nm Ag metallization is deposited by e-beam evaporation, followed by liftoff to create a hexagonal array of Ag disks as shown in Figure 2.15 (d). Between successive metasurface layers, an SU-8 dielectric layer is deposited by spin-coating, which also serves to planarize the surface for fabrication of the subsequent metasurface layer. Figure 2.15 (e) shows a large-area SEM image of a completed structure, in which a number of individual and clustered point defects in the hexagonal array are present. At larger length scales, well-ordered hexagonal grains with a typical lateral dimension of ~100 μm become evident.

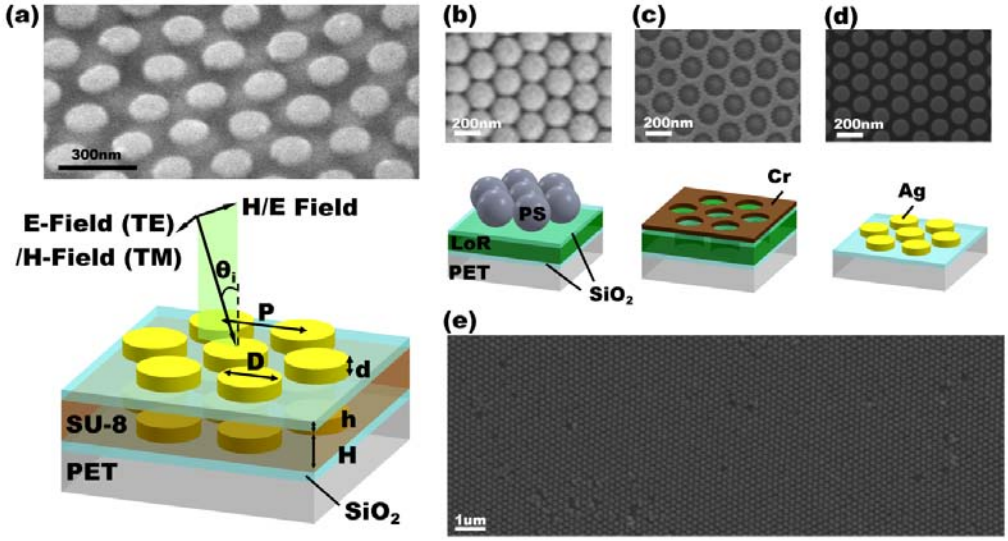

Figure 2.15: (a) Schematic diagram of the multilayer metasurface structure on a PET substrate under TE and TM polarized illumination. *P*, *D*, and d indicate the periodicity of the array, size, and thickness of the individual metallic nanostructure. The thickness of SU-8 and SiO_2 are denoted as *H* and *h*, respectively. The inset shows a scanning electron micrograph of a fabricated sample with *P* = 200 nm, *D* = 160 nm, *d* = 40 nm, *h* = 10 nm and *H* = 185 nm. (b)(c)(d) Schematic diagram of the fabrication process flow and scanning electron micrograph at each step: (b) A PET substrate is covered with 10nm SiO_2/100 nm LOR/10 nm SiO_2, followed by NSL using *D* = 200 nm PS nanospheres. (c) After deposition of 20nm of Cr and lift-off process of PS, the substrate is etched by RIE to create a hexagonal hole array structure. (d) The hexagonal hole array patterned PET substrate is deposited with 5 nm Ge/40 nm Ag, and the LOR is removed by lift-off process. (e) Large-area (6 x 16 μm^2) scanning electron micrograph image to show representative defects which can result from NSL.

2.4.3Bragg resonance

Previous work has shown [35, 43] that single- and double-layer metasurface structures consisting of square arrays of nanoscale metallic elements on glass substrate can provide wavelength-selective transmittance and reflectance at optical wavelengths that are insensitive to polarization and angle of incidence, with a double-layer metasurface able to provide low (<1%) transmittance and high (>75%) reflectance over a

bandwidth of ~100nm. As shown here, a large increase in bandwidth can be achieved with hexagonal rather than square arrays. Figure 2.16 (a)(b) shows experimentally measured transmittance T and reflectance R, along with the implied absorption $A = 1 - R - T$, for a single-layer metasurface with D = 160 nm, P = 200 nm, d = 40 nm, and h = 10nm for normal incidence. A minimum in transmittance (maximum in reflectance) is observed at ~605 nm with a full-width half-maximum (FWHM) bandwidth of ~300nm. Because this behavior is associated with the dipolar plasmonic resonance in an individual Ag disc as confirmed by numerical simulations shown in Figure 2.16 (c)(d), it is very weakly dependent on polarization of the incident light,[23, 25, 36] and also insensitive to defects in the hexagonal array associated with the nanosphere lithography patterning process. These features are similar to those observed in a single-layer square plasmonic metasurface array with similar dimensions,[35] for which a transmittance minimum was observed centered at ~650 nm with a bandwidth of ~200nm. As described below, we attribute the increase in bandwidth for the hexagonal array compared to the square array to stronger coupling among individual Ag plasmonic elements associated with a higher geometrical fill factor in the former. Figure 2.16 (e)(f) shows the measured transmittance, reflectance, and absorption as a function of θ_i from 15° to 60° under TE and TM polarized illumination. The resonance at 605 nm shows very weak dependence on angle of incidence consistent with our previous work.[43]

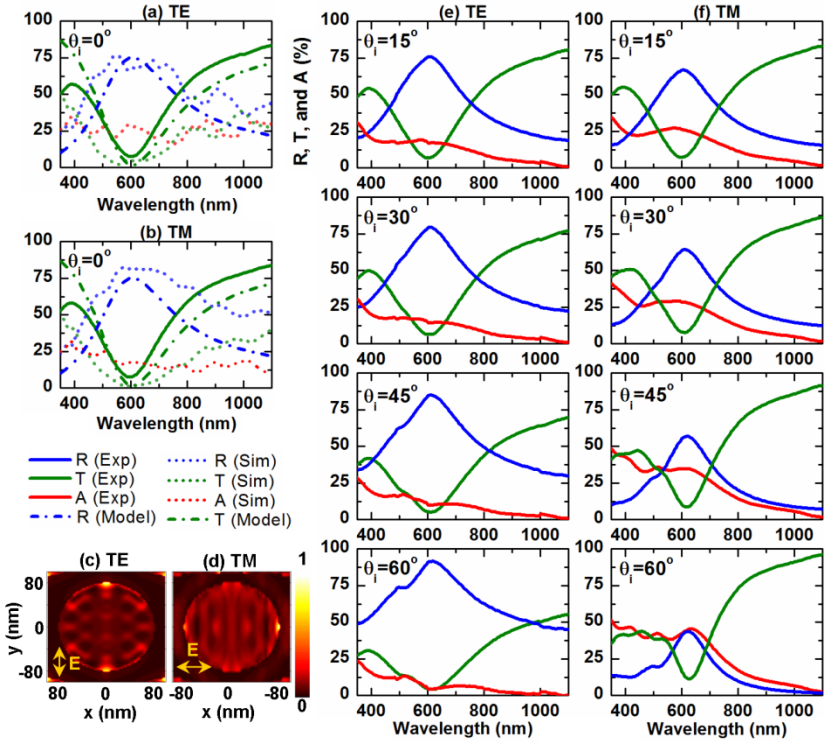

Figure 2.16: (a)(b) Measured, simulated, and modelled reflectance (R), transmittance (T), and absorption (A) spectra for a single layer metasurface with P = 200 nm, D = 160 nm, d = 40 nm, and h = 10 nm for θ_i = 0° under TE and TM polarized illumination, respectively. (c)(d) Normalized electric field distribution of the metasurface structure at resonant wavelength (λ = 605 nm) for θ_i = 0° under TE and TM polarized illumination, respectively. (e)(f) Measured refletance (R), transmittance (T), and absorption (A) spectra for a single layer metasurface with P = 200 nm, D = 160 nm, d = 40 nm, and h = 10 nm for θ_i = 15°, 30°, 45°, and 60° under TE and TM polarized illumination, respectively.

Analytical modeling of the optical response of a single-layer metasurface as an optically thin, polarization-independent homogeneous planar resonator can provide physical insight into the behavior of such structures, and a basis for rapid design and approximate modeling of multilayer metasurfaces.[38] Briefly, an effective susceptibility $\chi(\lambda)$ of the metasurface layer is defined, and assumed to be given by a Lorentzian lineshape function,[37-38, 41]

$$\chi(\lambda) = -\frac{\Gamma(\lambda_r/\lambda)}{hc(1/\lambda - 1/\lambda_r) + i\gamma}, \tag{2-44}$$

where h is Planck's constant, c is the speed of light in vacuum, Γ is a radiative linewidth, γ is a nonradiative linewidth, and λ_r is the resonant wavelength. From Eq. (2-44), we see that Γ is associated with the amplitude and broadening of the susceptibility at the resonant wavelength, consistent with the correlation between increased geometric fill factor and resonance bandwidth described above. The corresponding amplitudes of electromagnetic plane waves reflected by and transmitted across a single metasurface layer at normal incidence, $r(\lambda)$ and $t(\lambda)$, respectively, can be computed using a standard transfer matrix approach and are then given by

$$r(\lambda) = \frac{i\Gamma}{hc(1/\lambda - 1/\lambda_r) + i(\gamma + \Gamma)}, \tag{2-45}$$

$$t(\lambda) = \frac{hc(1/\lambda - 1/\lambda_r) + i\gamma}{hc(1/\lambda - 1/\lambda_r) + i(\gamma + \Gamma)}. \tag{2-46}$$

The reflectance R and transmittance T are then given by $R = |r|^2$ and $T = |t|^2$, respectively. Fitting these functions to the experimentally measured transmittance at normal incidence, shown in Figure 2.16, yields λ_r = 605 nm, Γ = 0.513 eV, and γ = 0.0794 eV, and the resulting modeled transmittance is seen to be in good agreement with the experimentally measured results.

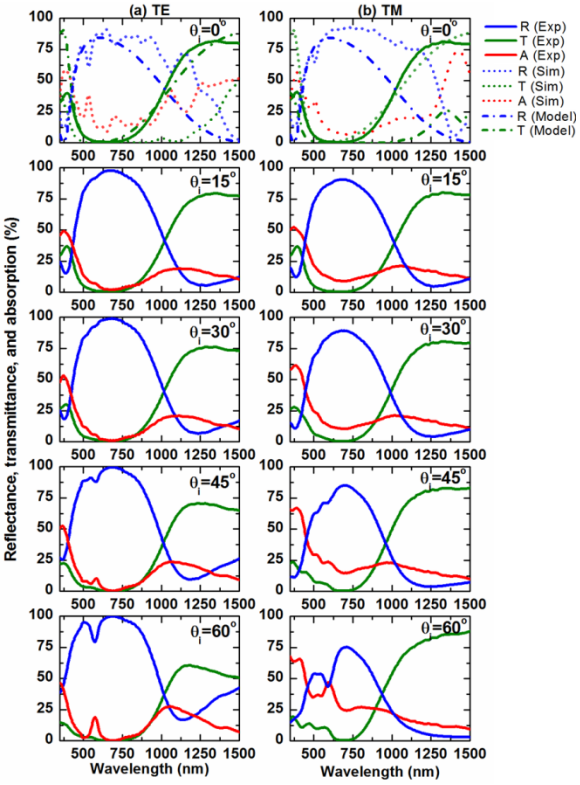

Figure 2.17: (a)(b) Measured, simulated, and modelled reflectance, transmittance, absorption spectra for a double layer metasurface with P =200 nm, D = 160 nm, d = 40 nm, h = 10 nm, and H = 185 nm for θ_i = 0°, 15°, 30°, 45°, and 60° under TE and TM polarized illumination.

This analytical model can be extended in a straightforward manner[38] to the design and analysis of multilayer metasurface structures. Figure 2.17 shows measured transmittance, analytically modeled transmittance and reflectance, and numerically simulated transmittance, reflectance, and absorption, at normal incidence with TE or TM polarization, for a multilayer structure containing two Ag metasurface layers, each with P = 200 nm, D = 160 nm, d = 40 nm, and h = 10 nm, separated by an SU-8 dielectric layer with H = 185 nm. Also shown are measured transmittance and reflectance, along with implied absorption, as a function of angle of incidence θ_i from 0° (normal incidence) to 60°. A very high, broad reflectance band is observed with peak reflectance near 650 nm

of ~90% or higher for angles of incidence ranging from 0° to 45° and for both TE and TM polarization. Bandwidth (FWHM) of ~400nm centered at ~650 nm is maintained for the measured high-reflectance band for both polarizations and over angles of incidence ranging from 0° to 45°.

The high, broad reflectance feature observed experimentally can be explained as a consequence of Bragg reflection by the multilayer metasurface structure using the analytical model described above. In general, the Bragg reflection criterion will be satisfied, and high reflectance will be observed, when the electromagnetic waves reflected by each individual metasurface layer are in phase with each other. According to Eq. (2-44), the wave component reflected from each metasurface layer will in general include a phase shift $\phi(\lambda)$ given by

$$\varphi(\lambda) = \tan^{-1}\left(\frac{\mathrm{Im}(r)}{\mathrm{Re}(r)}\right) = \tan^{-1}\left(\frac{hc\left(1/\lambda - 1/\lambda_r\right)}{\gamma + \Gamma}\right). \tag{2-47}$$

At the resonance wavelength λ_r = 605 nm, however, this phase shift vanishes, so that the Bragg criterion will be satisfied for $H + h = \lambda/2n_d \approx 190$ nm, where $n_d = 1.6$ is the refractive index of the dielectric separating the metasurface layers. For the two-layer metasurface structure of Figure 2.17, $H + h$ = 185 nm + 10 nm = 195 nm, allowing constructive interference due to Bragg reflection at and near the resonance wavelength to increase the peak reflectance, and broaden the reflectance peak, compared to that for a single-layer structure.[38] The performance of multilayer metasurface is superior than conventional thin film Bragg reflectors[40, 46] which have very limited angle of incidence acceptance and usually require many dielectric layers to achieve high reflectance. These characteristics of traditional Bragg reflectors will also restrict the use of thin film Bragg reflectors on curved surfaces.

We also observe that the width of the high-reflectance peak is close to its photonic bandgap, reached in the limit of an infinite periodic metasurface/dielectric stack, given by[38]

$$\lambda_{min} = \frac{1}{\frac{1}{\lambda_r} + \sqrt{\frac{2\Gamma}{\pi hc\lambda_r}}} < \lambda < \frac{1}{\frac{1}{\lambda_r} - \sqrt{\frac{2\Gamma}{\pi hc\lambda_r}}} = \lambda_{max}, \tag{2-48}$$

where $\lambda_{max} - \lambda_{min}$ is the FWHM bandwidth of the reflectance peak. For the single-layer metasurface parameters λ_r = 605 nm and Γ = 0.513 eV, derived from Eq. (2-46) and the data in Figure 2.17, we obtain λ_{min} = 432nm, λ_{max} = 1006 nm, corresponding to a FWHM bandwidth $\lambda_{max} - \lambda_{min}$ = 564 nm. The measured FWHM of the reflectance peaks for angles of incidence up to 30° is ~550 nm, close to the theoretical limit estimated from our analytical model and suggesting that bandwidth close to the photonic bandgap for a periodic multilayer metasurface structure can be achieved with as few as two metasurface layers. A detailed analysis employing the multilayer metasurface analytical model[38] is also consistent with this observation.

2.4.4 Fabry-Perot resonance

Phase shifts associated with reflectance by each metasurface layer also influence the nature of Fabry-Perot resonances and associated increases in absorption in multilayer metasurface structures. Figure 2.18 (a)(b) show numerically simulated reflectance, for TE polarized light, of a multilayer structure with two metasurface layers separated by an SU-8 dielectric layer, as a function of wavelength and dielectric thickness *H*, for angles of incidence of 15° and 60°. Each metasurface layer consists of a hexagonal array of Ag discs with *P* = 200nm, *D* = 160nm, and *d* = 40nm, atop a SiO_2 layer of thickness *h* = 10nm. For a given *H*, the numerically simulated reflectance exhibits local minima as a function of wavelength that can be attributed to Fabry-Perot resonances created by

reflection from each metasurface layer. Accounting for the wavelength-dependent phase shift introduced upon each reflection from a metasurface layer, the wavelengths for which Fabry-Perot resonances occur are given by[37, 43]

$$\lambda = \frac{2\sqrt{n_d^2 - \sin^2\theta_i}}{m - \varphi(\lambda)/\pi}(H + h), \tag{2-49}$$

where m is a non-negative integer corresponding to different Fabry-Perot modes, n_d and H are the refractive index and thickness, respectively, of the SU-8 dielectric spacer layer, and $\phi(\lambda)$ is given by Eq. (2-47). The Fabry-Perot resonance wavelengths given by Eq. (2-49) are shown as solid red lines in Figure 2.18 (a)(b), and show excellent agreement with numerically simulated results for angles of incidence of both 15° and 60°. Because of the nonzero phase shift associated with reflection from the metasurface layer, a Fabry-Perot mode exists even for m = 0, in contrast to conventional resonant cavities but consistent with recent studies of enhancement in absorption by a semiconductor deposited on a metal film, for which a nonzero phase is also introduced upon reflection.[47]

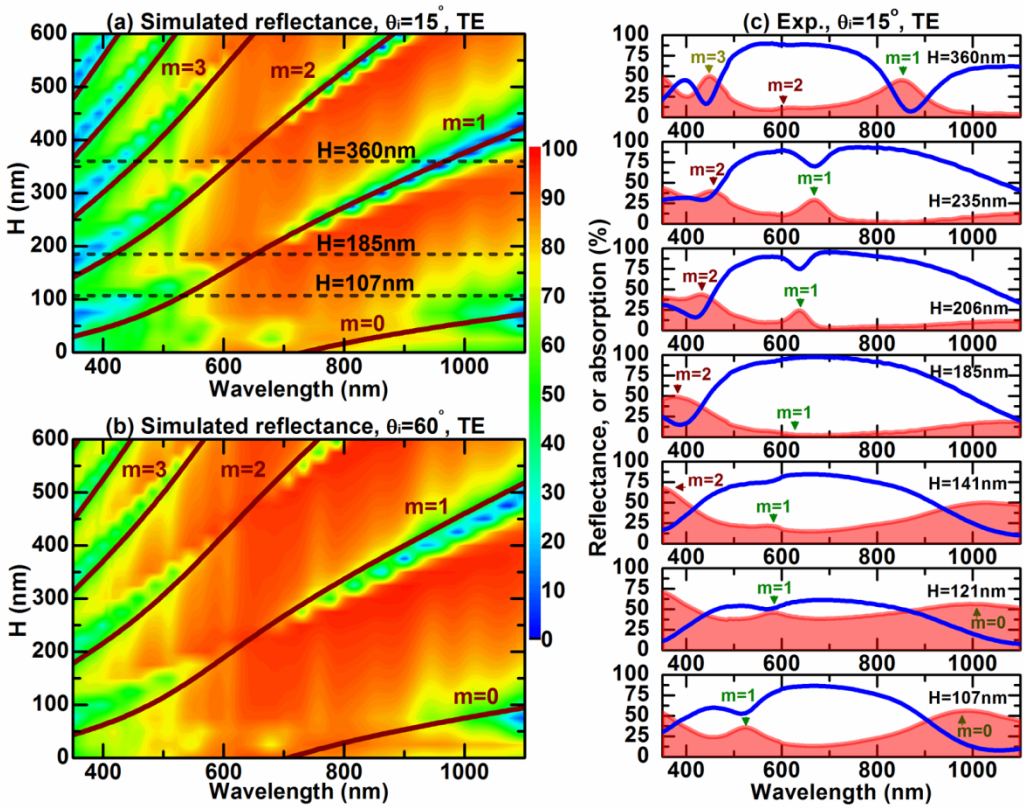

Figure 2.18: (a)(b) Simulated transmittance spectra as a function of wavelength and dielectric layer thickness, H, for $\theta_i = 15^o$ and 60^o. The solid curves represent the Fabry-Perot resonance given by Eq. (6). The dashed lines are indicated for double layer samples with H = 360 nm, 185 nm, 107 nm, respectively. (c) Measured reflectance (solid lines) and absorption (filled lines) for a double layer metasurface with P = 200 nm, D = 160 nm, d = 40 nm and h = 10 nm with different dielectric layer thickness, H, under TE polarized illumination.

These features are evident in the reflectance and absorption data shown in Figure 2.18 (c), measured at an angle of incidence of 15° for multilayer metasurface structures with SU-8 dielectric layer thickness H ranging from 107 nm to 360 nm. A dip in reflectance, and corresponding peak in absorption, are observed for the m = 1 Fabry-Perot resonance at wavelengths in reasonable agreement with those predicted by Eq. (2-49) for all values of H shown. For larger values of H, similar dips in reflectance and peaks in

absorption are observed for the m = 2 and, for H = 360 nm, the m = 3 Fabry-Perot resonances as well. For H = 107 nm and H = 121 nm, elevated absorption at wavelengths of ~1000nm is observed, corresponding to the m = 0 Fabry-Perot resonance that arises as a consequence of the nonzero phase shift associated with reflection from each metasurface layer. These Fabry-Perot resonances can be beneficial if increased absorption in the dielectric layer is desired, but are detrimental to maximizing reflectivity. In this regard, we note that the reduction in reflectance, and corresponding increase in absorption, is minimized for Fabry-Perot resonances that coincide in wavelength with the Bragg reflection condition. This is most evident in the structure with H = 185 nm, for which we see that the reflectance dip and absorption peak associated with the m = 1 Fabry-Perot resonance are strongly suppressed. On this basis, we observe that a broad, high reflectance band is most effectively achieved with a multilayer metasurface structure for which the metasurface plasmonic resonance wavelength λ_r coincides with a Bragg reflection condition. We also emphasize that our multilayer metasurface structure is very robust to variations in vertical layer-to-layer alignment in these discussed characteristics since large variations in vertical alignment are expected over the typical beam size (~1 mm) in our measurements. This is because the reflection and transmittance properties and Fabry-Perot resonances depend on plasmonic resonance in each individual metasurface layer. Near field coupling between elements in each layer will not play a significant role, when the vertical distance, $H + h$, is large enough, and this is also consistent with previously reported results.[43, 48]

2.4.5 Wavelength-selective focusing

Wavelength-dependent focusing by a flexible, multilayer metasurface structure is shown explicitly in Figure 2.19 (a) shows reflection of a distant, broadband illumination source by a ~2 x 2.5 cm^2 flat multilayer metasurface structure consisting of two metasurface layers with P = 200 nm, D = 160 nm, d = 40 nm, and h = 10 nm separated by an SU-8 dielectric layer with H = 185 nm, fabricated on a flexible PET substrate. Short-wavelength blue light (along with infrared light, not visible in the photograph) is transmitted, while light at longer visible wavelengths is reflected. Figure 2.19 (b)(c) show light transmitted and reflected by the same multilayer metasurface structure bend to different curvatures. The reflected light is observed to be focused onto different locations, depending on the degree of curvature of the multilayer metasurface, while the transmitted light remains collimated and largely unchanged in spectral content. The spectral distribution of the transmitted light at different locations x across a curved multilayer metasurface structure is shown in Figure 2.19 (d)(e), for TE and TM polarization, respectively. As shown in the inset to Figure 2.19 (d), these locations correspond to local angles of incidence ranging from 0° at x = 0 mm, corresponding to the midpoint of the curved surface, to ~60° at x = 7 mm, where x is the lateral distance from the midpoint of the curved surface. The transmitted spectra at all locations measured are very similar, differing primarily in that there is a slight decrease in transmittance at short wavelengths as x, and correspondingly the local angle of incidence, is increased. Based on simulations, analytical modeling, and measurements as shown in Figure 2.18, we attribute this decrease to the development of a Fabry-Perot resonance at shorter wavelengths as the local angle of incidence is increased. The results shown in Figure 2.19 provide direct confirmation of the ability to perform wavelength-selective imaging and focusing via flexible multilayer metasurface structures, uniformity of optical

properties over large (~5 cm^2) areas, and independence of optical properties to vertical alignment between individual features in adjacent metasurface layers for separations $H + h$ in the range studied here (~120 nm and larger).

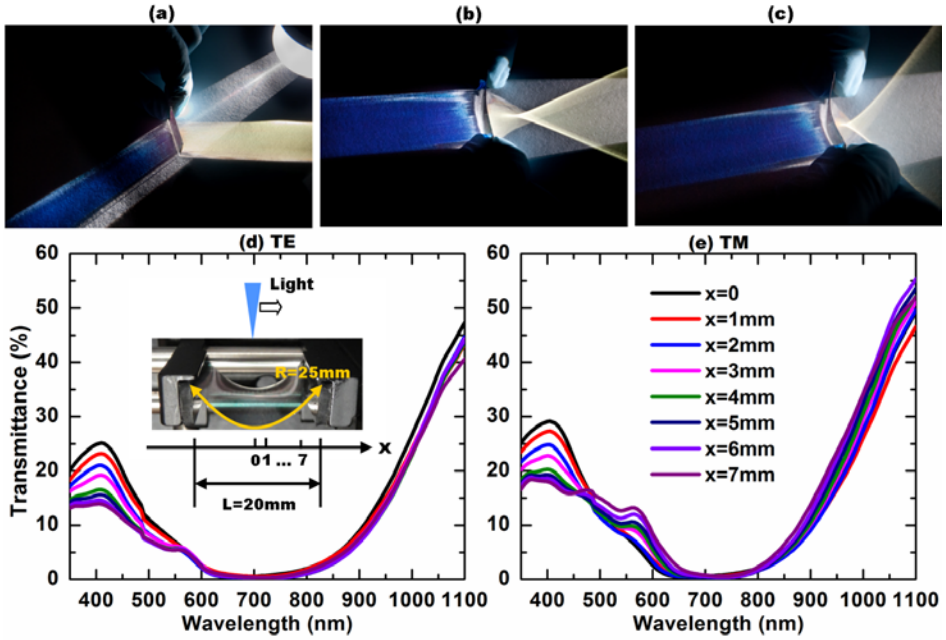

Figure 2.19: (a)(b)(c) Photo taken for samples (P = 200 nm, D = 160 nm, d = 40 nm, h = 10 nm and H = 185 nm) held flat, or bent to different curvatures under illumination from a solar simulator to show wavelength-selective focusing by the fabricated multilayer metasurface. (d)(e) Measured transmittance for a curved double layer metasurface under TE and TM polarized illumination with sample length 25 mm; the end-to-end length is bent to 20 mm. The measurement is taken at different positions of the sample starting from the center to around the edge of the sample, with increment of 1 mm which is roughly the beam size.

2.4.6 Conclusion

In summary, we have designed, experimentally demonstrated, and analyzed both numerically and analytically a series of flexible, large area, multilayer plasmonic metasurface structures fabricated via nanosphere lithography that provide low loss, wavelength-selective, polarization-independent optical transmittance, reflectance, and

focusing of incident light. These characteristics are shown to be robust to vertical misalignment between layers and variations within an individual metasurface layer. The high broad reflectance and low absorption can be understood as the consequence of the constructive Bragg reflection by the multilayer metasurface. Phase shifts associated with each individual metasurface are also examined both experimentally and numerically to show the influence of Fabry-Perot resonance. Finally, wavelength-selective focusing of visible light is also demonstrated.

2.5 PHOTOVOLTAIC-THERMAL HYBRID SYSTEM INTEGRATED WITH FLEXIBLE PLASMONIC FILTER

Concepts for optimizing the utilization of sun light, in particular, the combination of concentrating photovoltaic (CPV) and thermal absorbers which can provide higher efficiency than purely photovoltaic or thermal approaches are under intense study. However, such hybrid system is currently limited by the optical components such as dichroic filters which are highly sensitive to the angle of incidences. As an example, Figure 1(a) shows the schematic diagram of a new-type photovoltaic-thermal (PV-T) hybrid system, integrated with the flexible plasmonic metasurface. The optimized utilization of full solar spectrum is achieved by directing visible portions into PV; and ultraviolet and infrared light into thermal absorber.

The total efficiency of PV-T system, η_{PV-T} , can be expressed as,

$$\eta_{PV-T}(\lambda_{low},\lambda_g,C_{PV},T_c,T_{th}) = \eta_{PV}(\lambda_{on},\lambda_g,C_{PV},T_c) + \eta_T(\lambda_{off},\lambda_g,T_{th}), \qquad (2\text{-}50)$$

, where η_{PV} is the efficiency of the PV component, and η_T is the efficiency of the thermal converter, λ_{on} and λ_{off} cut-on and cut-off wavelengths, C_{PV} and C_{TH} concentration factors of PV and thermal converter, respectively, T_{PV} cell temperature, and T_{TH} operating temperature as shown in Figure 2.20 (c). Figure 2.20 (a) shows the theoretical efficiency of PV, η_{PV} , modeled by Shockley-Queisser limit. For one sun illumination ($C_{PV}=1$), the maximum efficiency is ~33% at $\lambda_{off}=1100nm$ which correspond to the bandgap energy of silicon. As we start to increase C_{PV} to 100, overall efficiencies are increased, and the peak efficiency is ~38%. For even higher C_{PV} , the maximum efficiency starts to saturate ~40%. Therefore if we consider a reasonable size

of lens employed in concentrated system within these limitations, $C_{PV} = 100$ is a reasonable choice. Figure 2.20 (b) shows the theoretical efficiencies of thermal converter based on thermodynamics. The black line is the Carnot cycle limit as a function of T_{TH}, which can be expressed as ,

$$1 - \frac{T_0}{T_{TH}}. \tag{2-51}$$

The Carnot cycle limit monotonically increase with T_{TH}, which is ideal for adiabatic process. However, if we consider the radiation from the absorber and possible loss involved in realistic situations, we can then further model the efficiency as,

$$\eta_{TH} = \frac{2}{3}(1 - \frac{T_0}{T_{TH}})(1 - \frac{\sigma^4}{S \cdot C_{TH}}), \tag{2-52}$$

where σ is the Stefan's constant, and S is defined as solar constant for one sun. Based on Eq. ((2-52), instead of monotonic increment as observed from Carnot cycle limit, the efficiency has an optimum point from each different C_{TH}, and the maximum efficiency can be increased as we increase C_{TH}. The most reasonable choice in consideration of optical limitation and operating temperature is $C_{TH} = 100$. Figure 2.20 (d) shows the optimized electricity output and efficiency of a proposed photovoltaic-thermal system. The theoretical efficiency can be achieved η ~58.7% which is higher than individual PV or thermal system.

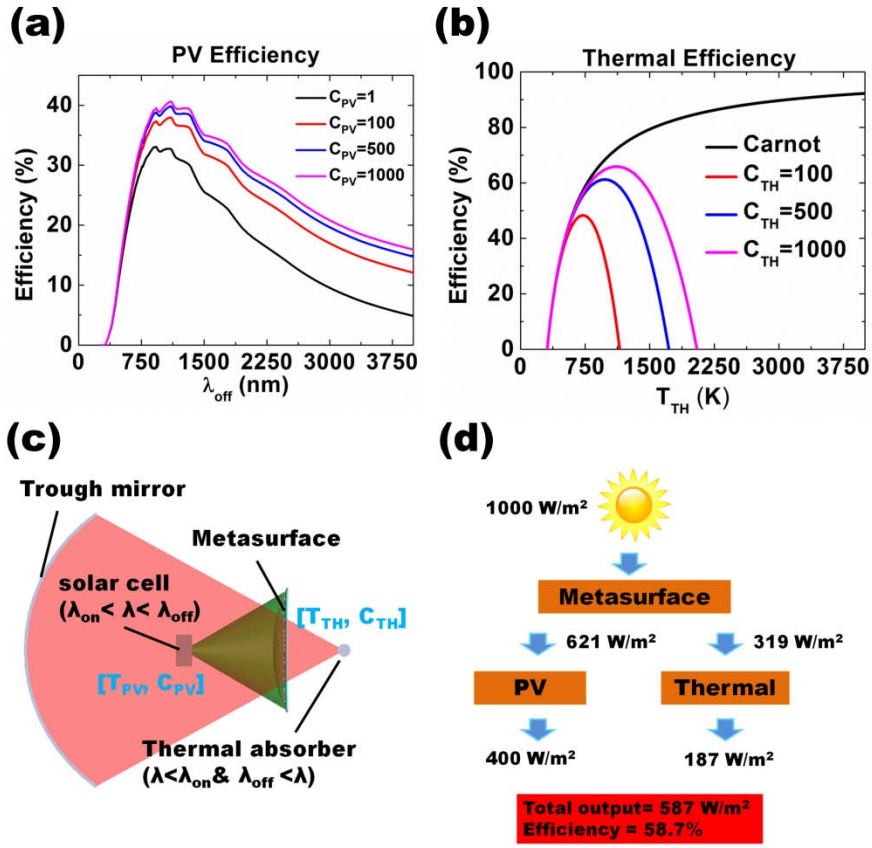

Figure 2.20: (a)(b) Theoretical efficiencies of photovoltaic and thermal absorber, respectively. (c) Side view of the proposed architecture of PV-T system. (d) Block diagram of final output of a proposed PV-T system.

Chapter 3: Omnidirectional Antireflection Coating on Low-Index Materials Integrated with Solar Cells

3.1 MOTIVATION

Coatings for reducing optical reflections from surfaces have attracted broad interest for applications ranging from photovoltaics to displays. The typical approaches for realizing anti-reflective surfaces can be grouped into two general categories[49]--homogeneous and inhomogeneous anti-reflection coatings. Homogeneous anti-reflection coatings typically use quarter-wave stacks of optical thin films to achieve admittance matching in both magnitude and phase;[50] however, implementations are often limited by the refractive indices of materials available in nature, although nanostructured material can expand the range of available refractive indices.[51-54] Inhomogeneous anti-reflection coatings can provide greater flexibility in effective refractive indices but often require the use of challenging nanofabrication processes. These have included top-down approaches such as self-masked dry etching,[55] wet etching,[56-59] electron beam lithography,[60] interference lithography,[61-62] and roll-to-roll nanoimprinting;[63] and bottom up approaches such as anodic alumina oxide nanoporous films,[64-65] nanosphere lithography (NSL),[66] and carbon nanotubes.[67] In nearly all cases, minimizing surface reflectivity for normally incident light has been emphasized. The challenge of reducing shallow-angle (angle of incidence > 60^{o}) reflection on low-index materials has not been well addressed, in terms of both the optimization of the anti-reflection surface and practical limitations in fabrication over large areas. In many applications, low-index materials such as polymer and glass have been widely used as packaging material; reduced reflectivity from such surfaces at large angles of incidence can have a major practical impact, e.g., by reducing glare from a flat display monitor, or increasing total efficiency of a solar panel module.

3.2 OPTIMIZATION AND REALIZATION OF OMNIDIRECTIONAL ANTIREFLECTION COATING ON LOW-INDEX MATERIALS

3.2.1Fabrication process

Figure 3.1 (a) shows a schematic diagram, photograph, and scanning electron micrograph of representative omnidirectional anti-reflection coatings described in this section, along with the measurement geometries for TE and TM polarizations. The nanostructures were fabricated on 1.1mm thick double side polished fused quartz substrates (Delta Technology). The structure of a unit cell can be specified by the hexagonal array periodicity (*P*), and the diameter (*D*) and height (*h*) of the constituent cylindrical dielectric pillars. Figure 3.1 (b) shows a photo taken at shallow angle to demonstrate that the reflection from an anti-reflection treated substrate (left, P = 200nm, D = 90nm, and h = 350nm) is lower than an untreated quartz substrate (right). Figure 3.1 (c) shows the scanning electron micrograph of a fabricated structure with P = 200nm, D = 100nm, and h = 350nm.

Figure 3.1 (d) shows key steps in the fabrication process for the omnidirectional anti-reflection nanostructure. The quartz substrate (1 square inch) is coated with 60 nm Cr/10 nm SiO_2 using e-beam evaporation. On top of the SiO_2 layer, a self-assembled ordered monolayer of 200nm diameter polystyrene (PS) nanospheres is deposited by the Langmuir-Blodgett method.[44-45] For our implementation of this process, defect-free hexagonally close packed regions of nanospheres typically extend over distances of ~20μm, separated by cracks between boundaries and a few vacancies. The diameters of the nanospheres are then reduced by reactive-ion etching (RIE) resulting in nanospheres with diameters of 50 nm to 150 nm, depending on etch time. These nanospheres then serve as an etch mask to transfer the hexagonal pattern to the underlying Cr, which acts as a hard mask during the subsequent quartz reactive ion etching process to achieve the

desired high aspect ratio cylindrical pillar structure. Finally, the Cr mask is removed by a standard wet etch process. While the structures presented here were fabricated from quartz, the general procedure just described can be applied to various substrates to create hexagonal arrays of submicron to nanometer-scale high aspect ratio pillars rapidly, at low cost, and over large areas.

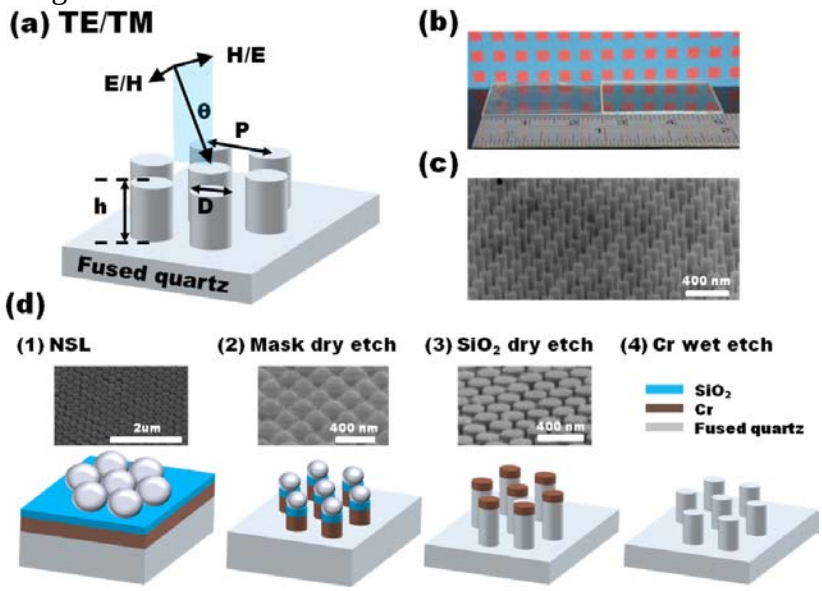

Figure 3.1: (a) Schematic diagram of a dielectric hexagonal lattice structure on a quartz substrate with periodicity (*P*), diameter (*D*), height (*h*), and of simulation and measurement geometry for TE or TM polarization. (b) Photo taken at shallow angle, showing that the anti-reflection coated quartz (left, *P* = 200 nm, *D* = 90 nm, and *h* = 350 nm) is less reflective compared with the non-treated substrate (right). (c) Scanning electron micrograph of a fabricated *P* = 200 nm, *D* = 100 nm, and *h* = 350 nm structure. (d) Schematic diagram of the fabrication process flow and scanning electron micrograph at each step: (1) A quartz substrate is cleaned, covered with 60 nm Cr/10 nm SiO_2, followed by NSL using *D* = 200 nm polystyrene nanospheres. (2) A series of dry etching processes is used to transfer the hexagonal lattice pattern to the underlying Cr layer. (3) Cylindrical nanopillars formed by SiO_2 dry etching using Cr hard mask (4) Wet etch to remove Cr.

Optical transmittance measurements were performed on these structures using collimated light from a halogen lamp spectrally resolved by a monochromator. The

monochromatic light was linearly polarized by a Glan-Thompson polarizer before reaching the device. Devices were mounted on a rotating stage, allowing measurements to be performed at angles of incidence, θ, ranging from 0^o to 72^o. Numerical simulations of the optical behavior of these structures were performed using rigorous coupled wave analysis (RCWA).[26] In these simulations, the refractive index of the quartz was taken to be 1.46, independent of wavelength.

3.2.2 Optimization and simulation of "nanopillar" structures on low-index substrate

To achieve a wide-angle, broadband anti-reflection coating, theoretically an optimal graded-index profile should yield the best results;[68-73] however, such a structure would require sufficiently large depth to produce low reflectivity at large angles of incidence. As discussed below, the required depths result in structures that are highly impractical to fabricate. We have therefore focused on nanopillar structures which are physically attainable and provide wide-angle broadband anti-reflection properties. Theoretical calculations for single layer anti-reflection coatings with incident wavelength λ = 500 nm and θ = 85^o can provide insight in the design of a shallow angle anti-reflection coating. The reflectance for such a structure, based on Fresnel's equation, can be expressed as2

$$R = \frac{(n_0 - n_{sub})^2 \cos^2\delta + [(n_0 n_{sub} / n_{arc}) - n_{arc}]^2 \sin^2\delta}{(n_0 + n_{sub})^2 \cos^2\delta + [(n_0 n_{sub} / n_{arc}) + n_{arc}]^2 \sin^2\delta}, \quad (3\text{-}1)$$

where $\delta = 2\pi\sqrt{n_{arc}^2 - \sin^2\theta}\, d/\lambda$; $n_{0,}$ n_{sub} and n_{arc}, are the refractive indices of air, the dielectric substrate, and the anti-reflection coating layer, respectively; and d is the thickness of the anti-reflection coating. For a quartz substrate with n_{sub} = 1.46, the optimal n_{arc} can then be calculated from Eq. (3-1) to be 1.05 and 1.02 for TE and TM polarization, respectively, and the optimal thickness, d, can be calculated by setting δ =

$\pi/2$, yielding $d \sim 376$ nm. Materials with $n < 1.3$ do not exist in nature but we can synthesize them by fabricating a subwavelength nanostructure such as the hexagonal lattice nanopillar array illustrated in Figure 3.1. We note that the effective index of a two dimensional structure such as the nanopillar array cannot be given by an analytical closed form using effective medium theory due to difficulties in descriptions of fields along all directions. Thus, it is necessary to determine the effective refractive index via simulations. In this retrieval process, we assume the subwavelength nanopillar structure behaves like a homogeneous medium with effective refractive index n_{eff} if $P << \lambda$, and we compare the simulated transmittances for nanopillar structures with different *D/P* ratios and a thin film with variable index n_{eff} for the same height under various angles of incidence to determine the effective refractive index at normal incidence. This process yields

$$n_{eff} \approx 0.4(D/P)^2 + 1. \tag{3-2}$$

The previously calculated n_{arc} can then be converted into a *D/P* ratio based on Eq. (2), yielding optimal values for *D/P* of ~0.35 and 0.22 for TE and TM polarizations respectively. Because the transmittance for TM polarization is already very high, while transmittance for TE polarization decreases rapidly with increasing angle of incidence, we choose *D/P* = 0.35 as our starting point for design and fabrication of our anti-reflection surfaces.

Figure 3.2 (a) shows the numerically simulated transmittance as a function of *D* and *P* under 45^o polarization with h = 350nm, $\theta = 85^o$, and λ = 500nm. These simulations indicate that the transmittance can be raised to ~85%, compared to 40% for a bare quartz surface, with *D/P*=0.35 (n_{eff}~ 1.05). The optimal ratio *D/P* under 45^o polarization is close to the previously calculated TE optimal value, since the transmittance of TE polarized light varies much more strongly than that of TM polarized light at large angles of

incidence. The predicted low surface reflectance is also very robust to variations in the detailed nanopillar structure: for D/P varying from 0.12 to 0.55, or equivalently, n_{eff} varying from 1.006 to 1.12, one can still achieve ~20% (~1.5x) transmittance enhancement. In this respect, these designs are expected to be very robust to fabrication-induced variations in structure. The simulations shown in Figure 3.2 (a) also indicate that P can be increased to values larger than λ while maintaining high transmittance at shallow angles of incidence. However, for $P \gtrsim \lambda$, the high transmittance will result in part from higher-order diffraction peaks, and the direction of light transmittance will therefore differ from the incident direction. If the application requires only overall high transmittance regardless of diffraction, non-subwavelength values of P can be chosen; otherwise, subwavelength periodicities are still preferred for enhancing zero-order transmission.

Figure 3.2 (b) illustrates the simulated dependence of transmittance on D and h for P fixed at 200 nm; with $\theta = 85^{o}$ and $\lambda = 500$ nm, the maximum transmittance can be raised to ~87.7% with $P = 200$ nm, $D = 70$ nm, and $h = 350$ nm, under 45^{o} polarization. Away from the region of maximum transmittance, a ripple pattern associated with Fabry-Perot interferences across different values of D and h is observed: as h increases, we observe an increase in Fabry-Perot modes within the nanopillars between different D, resulting in several locally optimal points; however, these points have less tolerance to variations in the value of D/h compared with the global optimum, therefore they are less favored from a fabrication perspective. The overall transmittance decreases when D increases regardless of h, since n_{eff} increases and there is a greater mismatch between the relative refractive indices of air and substrate. The periodicity and magnitude of the

Fabry-Perot interferences observed in simulation agree well with these predicted by Eq. (3-1).

Figure 3.2 (c) shows a comparison of simulated transmittance spectra for angles of incidence from 0^o to 85^o between a tapered “moth eye” structure (for which D is linearly tapered from 70 nm to 0 nm) and the cylindrical nanopillar (D = 70 nm) structure, with the same period P = 200 nm and height h = 350 nm for both, under 45^o polarization. The "moth eye" and cylindrical nanopillar structures have similar transmittance response (~95%) for $\theta = 0^o$-60^o; however, the transmittance of the "moth eye" structure starts to decrease quickly beyond $\theta = 60^o$ while the cylindrical nanopillar structure maintains high transmittance to $\theta=75^o$ for all wavelengths, and transmittances ~80% or higher to $\theta = 80^o$ in wavelength range of 500 to 650 nm. Our simulations can be compared with earlier experimental work of a tapered "moth-eye" structure (for which D is linearly tapered from 140 nm to 60 nm) with P = 150 nm and h = 150 nm on glass, we note that the transmittance of "moth-eye" structure with insufficient height decreases significantly when $\theta > 75^o$ which is consistent with our simulations.

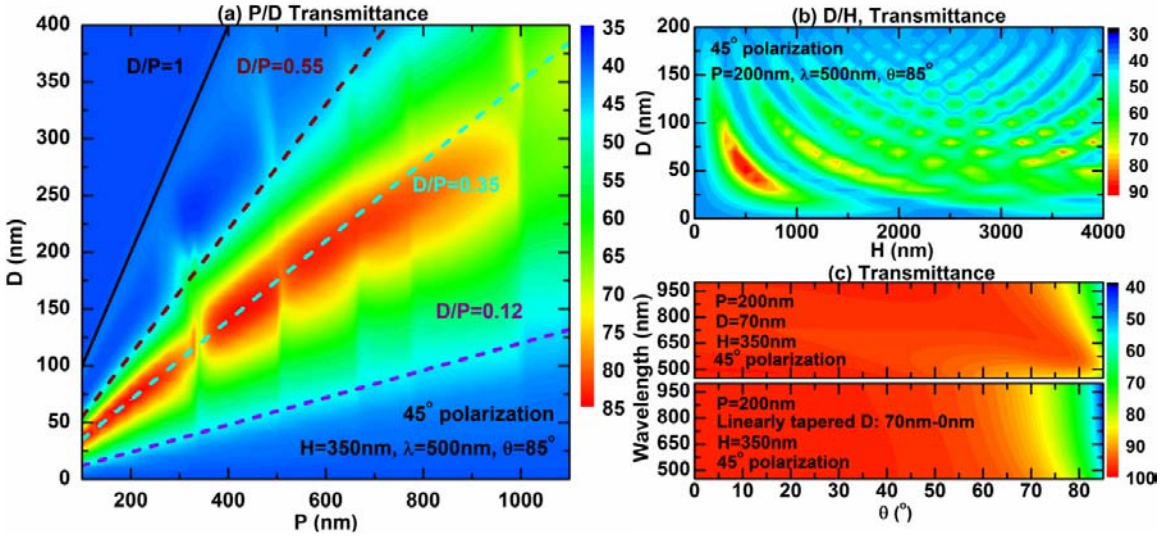

Figure 3.2: Simulated transmittance spectra of a dielectric hexagonal lattice structure: (a) Transmittance contour map with h = 350 nm, λ = 500 nm, θ = 85^o under 45^o polarization. (b) Transmittance contour map with P = 200 nm, λ = 500 nm, θ = 85^o under 45^o polarization. (c) Transmittance spectra comparison between D = 70 nm cylindrical nanopillar structure, and linearly "moth eye" structure with tapered D from 70-0 nm with same P = 200 nm, h = 350 nm, under 45^o polarization.

Perfect antireflection structures have been discussed theoretically using different tapered "moth eye" geometries[69-74]; however, the geometries of these structures need to match perfectly to form the optimally graded-index profile, and the height of the structure needs to be large enough to ensure a sufficiently smooth transition from air to substrate to avoid reflection. Therefore, both total height and potential profile imperfections are key concerns in design and fabrication of "moth eye" antireflection coatings. Figure 3.3 (a) shows simulated transmittance spectra as a function of height (h) at λ = 500 nm and θ = 85^o for an optimized cylindrical pillar structure (D = 70 nm, P = 200 nm, h = 380 nm) and tapered "moth eye" structures with different base diameters (D). For height h limited to 380 nm or less, the cylindrical nanopillar structure with h = 380 nm clearly outperforms any tapered "moth eye" structure. As the allowable height is

increased to ~1 μm, certain "moth eye" structures can yield transmittance slightly higher than the cylindrical nanopillar structures but only within narrow ranges of height and base diameter. The "moth eye" structures are superior only for heights of ~1.5 μm or greater, and such structures would be both highly impractical to fabricate and very fragile in actual use. Figure 3.3 (b) shows simulated transmittance spectra as a function of top diameter (*W*). The transmittance monotically decreases as the structure starts to taper. The pillar structure will lose its benefits compared to "moth-eye" in similar dimensions when the top diameter is decreased to 35 nm or less. We note the superiority of the pillar structure is also robust to tapering due to manufacturing errors. Thus, in situations requiring very low reflectance over a broad range of angles and moderate range of wavelengths, the cylindrical nanopillar structures demonstrated here are expected to be superior to any practical "moth eye" structure.

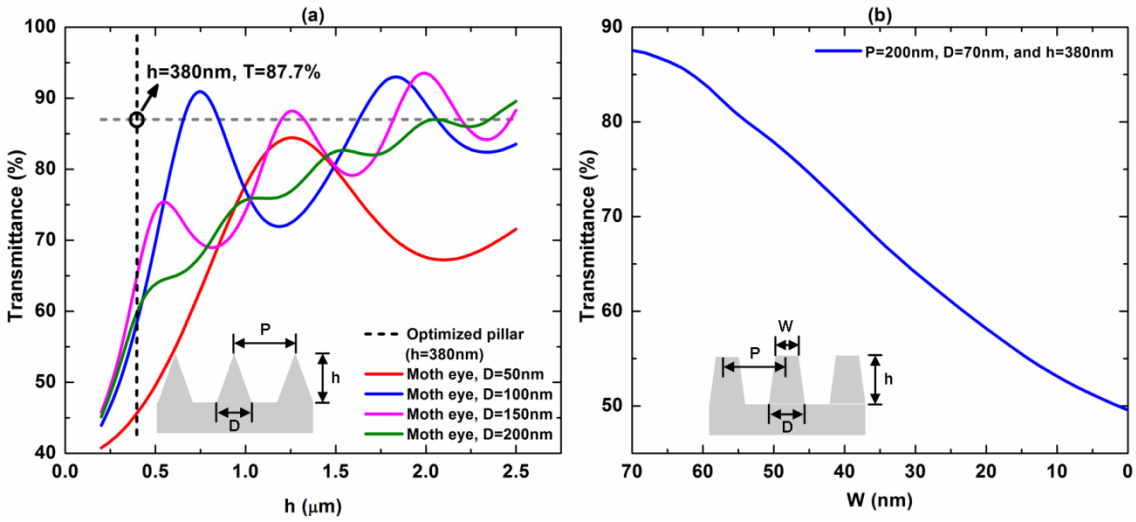

Figure 3.3: (a) Simulated transmittance spectra of tapered "moth eye" structures at λ = 500 nm, θ = 85°, as a function of height (h) with P = 200 nm and D = 50 nm, 100 nm, 150 nm, 200 nm under 45° polarization. The horizontal gray dashed line corresponds to the optimized cylindrical nanopillar structure with P = 200 nm, D = 70 nm, h = 380 nm, and the vertical dashed line indicates h = 380 nm for comparison. The inset shows a schematic diagram of the tapered "moth eye" structures for which the simulations were performed. (b) Simulated transmittance spectra of tapered pillar structures with P = 200 nm and D = 70 nm at λ = 500 nm, θ = 85°, as a function of top diameter (W) under 45° polarization. The inset shows a schematic diagram of the tapered pillar structures for which the simulations were performed.

3.2.3 Characterization and measurement of "nanopillar" structure on low-index substrate

Figure 3.4 (a) shows the measured transmittance spectra for nanopillar structures with P = 200 nm, h = 350 nm, and D = 50, 90, or 100 nm, along with transmittance for an unpatterned quartz substrate, for θ = 0°-72° and λ = 450-1050 nm, under TE polarization. The transmittances for nanopillar structures with D = 50, 90, 100 nm are greatly enhanced compared to that for the quartz substrate for all wavelengths and angles of incidence. Figure 3.4 (b) shows a comparison of different transmittance spectra with λ = 500 nm, at θ = 0°-85°. Within these structures, D = 90 nm shows the highest

transmittance (~87%) at θ = 72°, which is ~25% (~1.45x) enhancement in transmittance compared with the unpatterned quartz substrate; the transmittance spectra of structures with D = 50 nm and 100 nm show similar enhancement, but of slightly smaller magnitude than for D = 90 nm, due to the non-optimal D/P ratio.

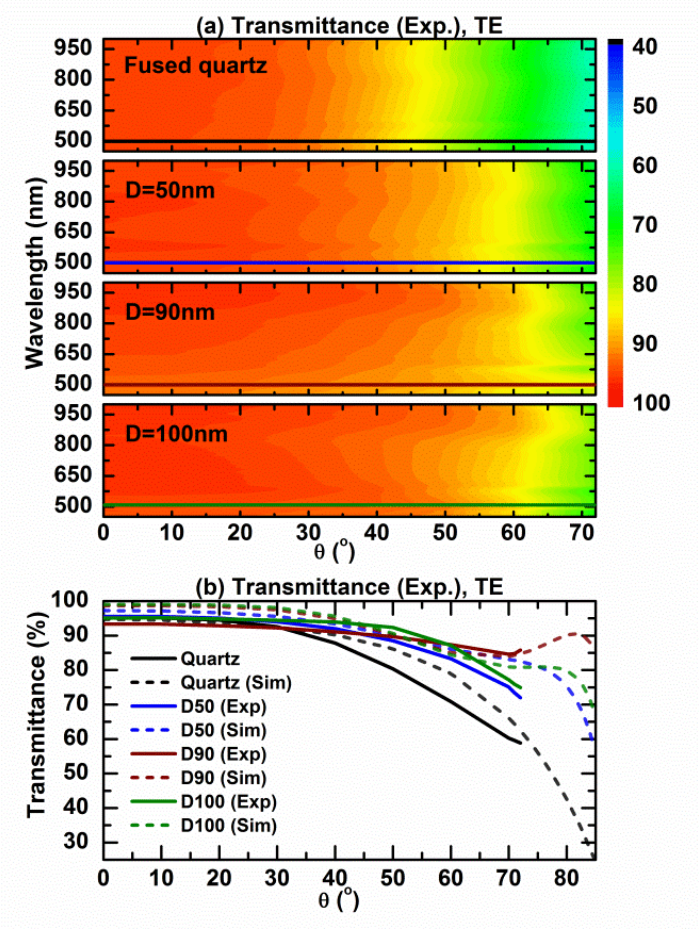

Figure 3.4: (a) Measured transmittance spectra of quartz, and cylindrical nanopillar structures with P = 200nm, h = 350nm, and D = 50, 90, or 100 nm. (b) Measured (solid lines) and simulated (dashed lines) transmittances at λ = 500 nm, as functions of angle of incidence (θ) for quartz substrate and structures with P = 200 nm, h = 350 nm, and D = 50, 90, or 100 nm under TE polarization.

Figure 3.5 (a) shows the measured transmittance spectra under TM polarization. The transmittances of the cylindrical nanopillar structures with D = 50 nm and 100 nm are ~92%, which is similar to that of the unpatterned quartz substrate for θ = 0-50^{o}, and reaches ~95%, which is higher than that for the unpatterned surface, when θ > 50^{o}. Transmittance for D = 90 nm is close to that of the unpatterned substrate since the admittance is slightly less optimized at TM polarization, but given the large TE transmittance this structure exhibits at shallow angles, the overall transmittance for the D = 90 nm structure averaged over all incident polarizations will be the highest. The simulations are generally in good agreement with experimental data except for a small offset, which we attribute to fabrication imperfections and differences in dispersion relations between the actual quartz substrate and the values assumed in our simulation.

3.2.4Conclusion

In summary, we have designed, demonstrated, and analyzed a series of subwavelength dielectric nanostructures that provide very high transmittance over visible wavelengths for different polarizations and over the entire range of angle of incidence. Detailed analysis based on simulations and theory reveal the optimal choices of feature size, periodicity, and height of subwavelength nanopillar structures associated with matching of phase and magnitude at large angle of incidence. The performance of an optimal nanopillar structure is shown to be superior to that of "moth eye" structures within realistic fabrication limits on low-index substrates. The nanopillar structures fabricated via NSL are tunable, and may be applicable to different substrates, and can be used for a broad range of practical applications.

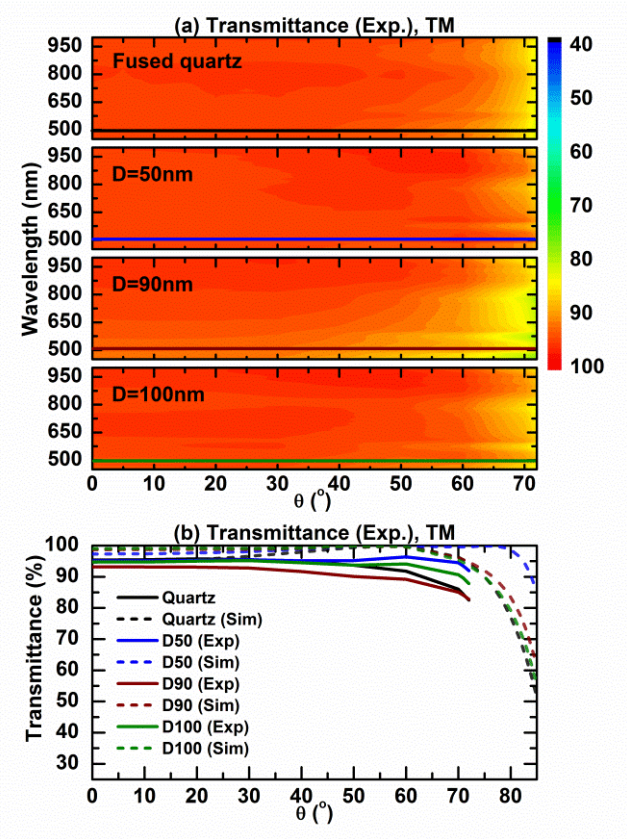

Figure 3.5: (a) Measured transmittance spectra of quartz, and cylindrical nanopillar structures with P = 200nm, h = 350nm, and D = 50, 90, or 100 nm. (b) Measured (solid lines) and simulated (dashed lines) transmittances at λ = 500 nm, as functions of angle of incidence (θ), for quartz substrate and structures with P = 200 nm, h = 350 nm, and D = 50, 90, or 100 nm under TM polarization.

3.3 Optimization and Realization of Antireflection Coating Integrated with GaAs Solar Cell

III/V solar cells play a key role in photovoltaic energy harvesting for various space and terrestrial applications, and are strong candidates for concentrating photovoltaic and next-generation solar cell concepts. [75-78] Furthermore, recent advances in epitaxial growth and processing of III/V, thin-film solar cells, including

approaches for separation of active device layers from epitaxial growth substrates, has made III/V solar cells increasingly attractive for electricity generation strategies such as concentrated photovoltaic (CPV) systems [79] and mobile solar devices [80] that require very high energy conversion efficiency and/or reduced material usage. [81-87] However, in these photovoltaic applications, Fresnel reflection particularly at large angles of incidence becomes the primary factor in limiting the overall energy conversion efficiency. Conventional planar thin-film antireflection coating [50] are designed to provide excellent antireflection performance within a narrow band of wavelengths in the solar spectrum. Furthermore, the limitation of the number of materials with different refractive indices that exist in nature acts as the bottleneck for further improving the photovoltaic performance of such approach. [51, 88-90]

3.3.1 Fabrication process

Figure 3.6 (a) shows the schematic diagram of a complete packaged solar cell structure with polyethylene terephthalate (PET) "moth-eye" and Al_2O_3 "nanoisland" nanostructures integrated with standard Al_2O_3/TiO_2 bilayer antireflection coating and GaAs solar cell. Figure 3.6 (b)-(d) shows the key steps in fabrication process of "moth-eye" on a PET films (Dupont Melinex 454, 100μm). A self-assembled monolayer of D_1=200nm polystyrene (PS) sphere is deposited via Langmuir-Blodgett method as shown in Figure 3.6 (b). In the subsequent reactive ion etching (RIE) process, the PS spheres mask and PET substrate are etched simultaneously under O_2 plasma to complete the "motheye" structures as shown in Figure 3.6 (d). The finalized "motheye" structures have the same diameter D_1 and different heights, H_1 depending on total etching time as shown in Figure 3.6 (d). Similar process can be employed for fabricating “nanoisland” structure

as shown in Figure 3.6 (f)-(h). The NSL was employed with D_2=1000nm PS spheres as shown in Figure 3.6 (f). 500nm Al_2O_3 was deposited by electron beam evaporation and followed by standard lift-off process to remove the PS spheres.

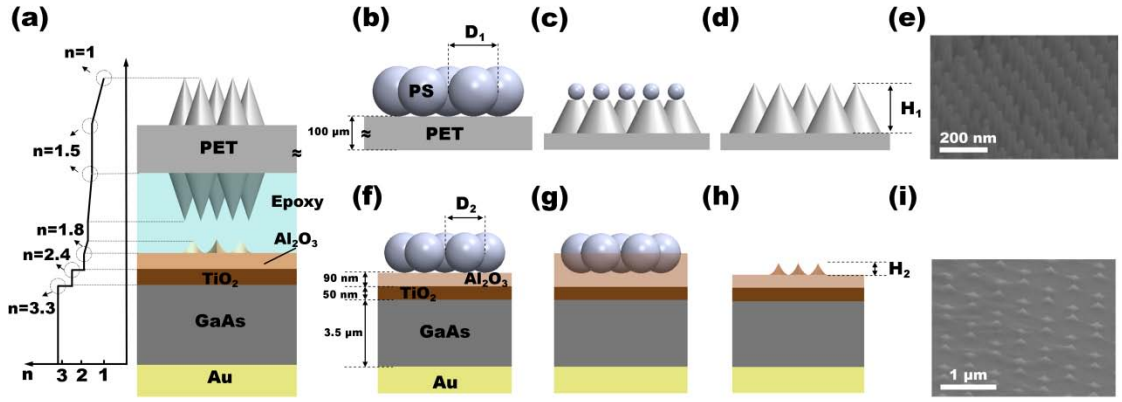

Figure 3.6: (a) Schematic diagram of "motheye" and "nanoisland" antireflection nanostructure integrated with GaAs solar cell. (b)-(d) Key steps in fabrication process of "motheye" structures on PET (e) SEM image of a "motheye" nanostructure on PET substrate. (f)-(h) Key steps in fabrication process of "nanoisland structure" (i) SEM image of a "nanoisland" structure on Al_2O_3/TiO_2 bilayer antireflection coating.

3.3.2 Optimization of "moth-eye" nanostructures on PET substrate

Figure 3.7 (a) shows the measured transmittance spectra for "motheye" structures on PET with H_1= 300, 400, 500, and 600nm along with transmittance for an unpatterned PET substrate for θ=0-75^o and λ=400-1100nm under TE polarization. The transmittances for "motheye" structures are greatly enhanced compared to that for the PET substrate for all wavelengths and angles of incidence. Figure 3.7 (b) shows a comparison of different transmittance spectra at θ=75^o. Within these structures, H_1=400nm shows the highest transmittance which is ~40% (~2x) enhancement in transmittance compared with the

unpatterend PET substrate. The transmittance spectra of structures with H_1=300, 500, and 600nm shows similar enhancement but of less magnitude than for H_1=400nm, suggesting that the transmittance saturates at a certain height of the motheye structure which is different with simulations possibly due to fabrication limitations of perfect shape of pyramidal structure at this height.

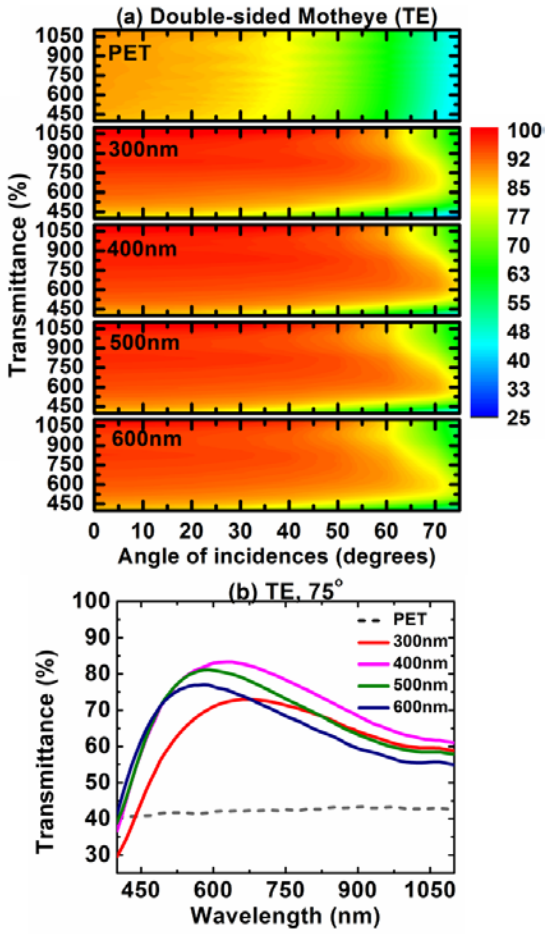

Figure 3.7: (a) Measured transmittance spectra of PET (dashed line) and "motheye" patterned PET with H_1=300nm, 400nm, 500nm, and 600nm (solid lines) under TE illumination. (b) Measured transmittance spectra at $\theta = 75^0$ for PET and "motheye" patterned PET.

Figure 3.8 (a) shows the measured transmittance spectra under TM polarization. The transmittances of all motheye structures are similar to that of the unpatterned PET substrate for θ=0-60^{o}, and performs ~5% worse than unpatterned PET when θ > 60^{o} because the structure is optimized primarily for the TE polarization which can contribute to a greater improvement of transmittance.

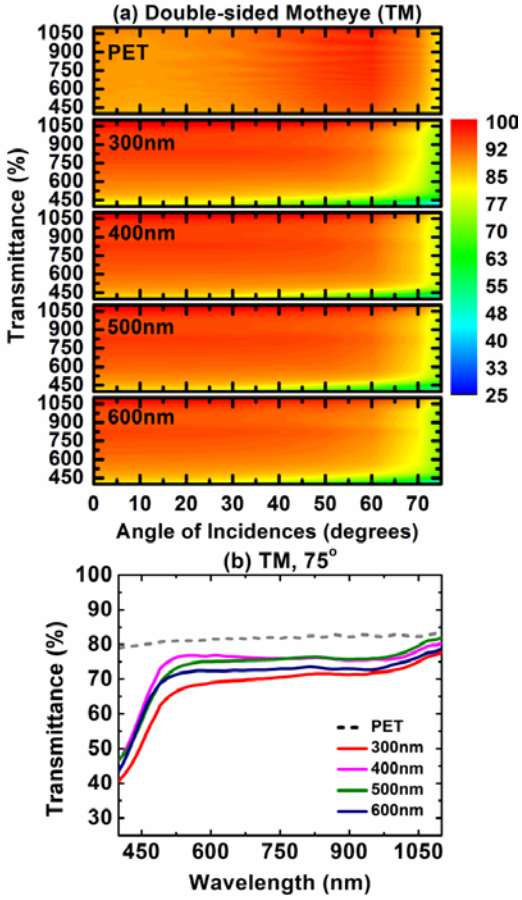

Figure 3.8: (a) Measured transmittance spectra of PET (dashed line) and "motheye" patterned PET with H_1=300nm, 400nm, 500nm, and 600nm (solid lines) under TM illumination. (b) Measured transmittance spectra at $\theta = 75^{0}$ for PET and "motheye" patterned PET under TM illumination.

3.3.3 Optimization of "nanoisland" structures on bilayer antireflection coating

Figure 3.9 (a) shows the schematic diagrams of (i) "nanoisland" Al_2O_3/TiO_2 nanostructure, and (ii) conventional Al_2O_3/TiO_2 antireflection coating on GaAs solar cell. These structures are measured under unpolarized illumination with different angle of incidences (θ). Figure 3.9 (b) shows the simulated absorption of structure (i) as functions of wavelength, and periodicities (D_2) for θ=0^o and 80^o. The height of the "nanoisland," H_2, is assumed to be D_2/2 for an ideal structure. For θ=0^o, we observe that there are two minimums in absorption from 310nm to 330nm and 370nm to 420nm which are present for all values of D_2. These absorption dips are resulted from the underlying bilayer antireflection coating, and they play less significant role in photovoltaic performance since the quantum efficiencies of GaAs at these wavelengths are low. For large angle of incidences, i.e. θ=80^o, the influence of the "nanoisland" dielectric structures become more prominent. The maximized absorption can be found at D_2>500nm due to the enhanced transmittance from the graded-index profile of "nanoisland" with sufficient height. Inside the optimum band, the previously observed absorption minimum dips at θ=0^o, are modulated with the optimum band boundaries at 80^o which occur at specific periodicities, D_2, (or heights which are H_2=D_2/2). In addition to absorption dips (from 310nm to 330nm and 370nm to 420nm) resulting from bilayer antireflection coating, we observe interference lines in the simulated contour map. Further inspection from simulation of Al_2O_3 "nanoisland" on bulk Al_2O_3 (as shown in the inset) reveal the physical origin of the interference at $\theta = 80^o$ is from the Fabry-Perot resonances of the "nanoisland" structure at certain combination of heights and wavelengths. Figure 3.9 (c) shows the measured external quantum efficiency (E.Q.E.) of structure (i) with D_2=1000nm and H_2=150nm (dashed lines), and structure (ii) (solid lines) at different θ. For θ=0^o to 60^o, the measured E.Q.E. of structures (i) and (ii) are similar because bilayer antireflection coating can

provide reasonably good performance for θ<60^o. For θ=80^o, the measured E.Q.E. of structure (ii) is higher than (i) but less significant compared with previous simulated results due to the fabrication limitation of H_2.

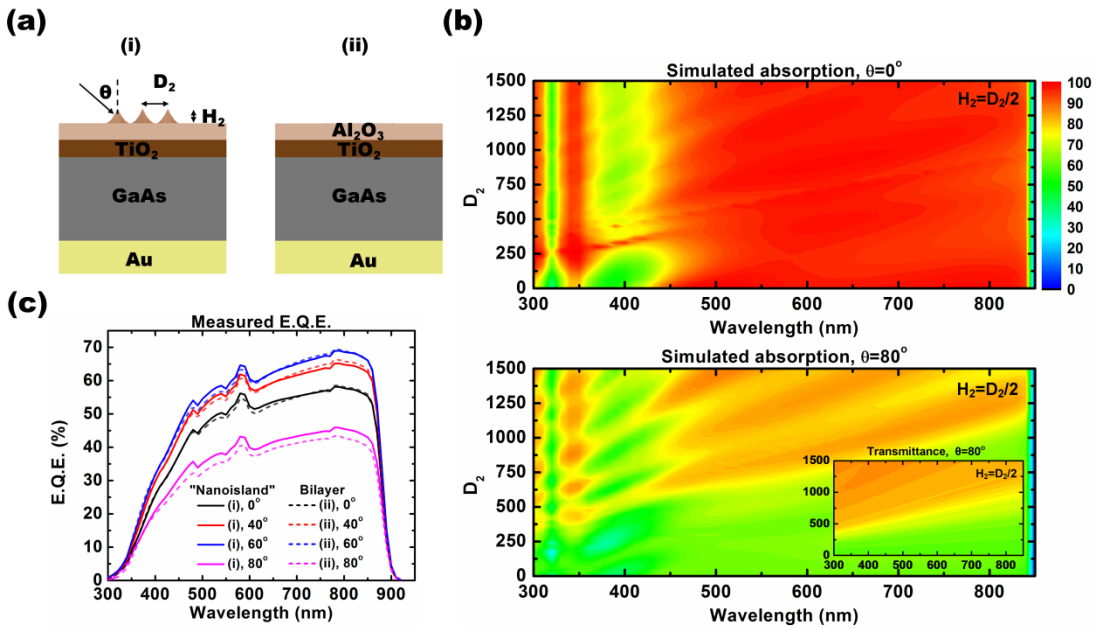

Figure 3.9: (a) Schematic diagram of (i) "nanoisland" on Al_2O_3/TiO_2 on GaAs solar cell and (ii) bilayer antireflection coating on GaAs solar cell. (b) Simulated absorption as functions of wavelengths and D_2 at $\theta = 0^o$ and $\theta = 80^o$. The inset shows the simulated transmittance as functions of D2 and wavelengths of an Al_2O_3 "nanoisland" on Al_2O_3 bulk. (c) Measured external quantum efficiency of structures (i) (solid lines) and (ii) (dashed lines) under different angle of incidences.

3.3.4 Realization and measurement of omnidirectional antireflection coating integrated with GaAs solar cell

Figure 3.10 (a) shows the schematic diagrams of (i) "moth-eye" and "nanoisland" integrated with bilayer antireflection coating, (ii) "moth-eye" with bilayer antireflection coating, (iii) plane PET on "nanoisland" integrated with bilayer antireflection coating, and (iv) PET on bilayer antireflection coating. Figure 3.10 (b) shows the measured

external quantum efficiency as a function of wavelengths and angle of incidence for structure (i)-(iv). Significant improvement of E.Q.E can be observed for >60^o as the graded-index at the interfaces of air to PET and epoxy to Al_2O_3 employed. Figure 3.10 (c)(d) shows the measured short circuit current and ratio as a function of angle of incidence. Structure (i) shows the best overall performance for all angle of incidence, the J_{sc} ratio is ~1.06x at θ=0^o and 1.67x at θ=80^o. Structure (ii) also shows significant improvement in J_{sc} but less when θ>40^o. Structure (iii) has the similar performance with (iv) at smaller θ, and more significant improvement at larger θ due to the graded-index profile from "nanoisland" structure.

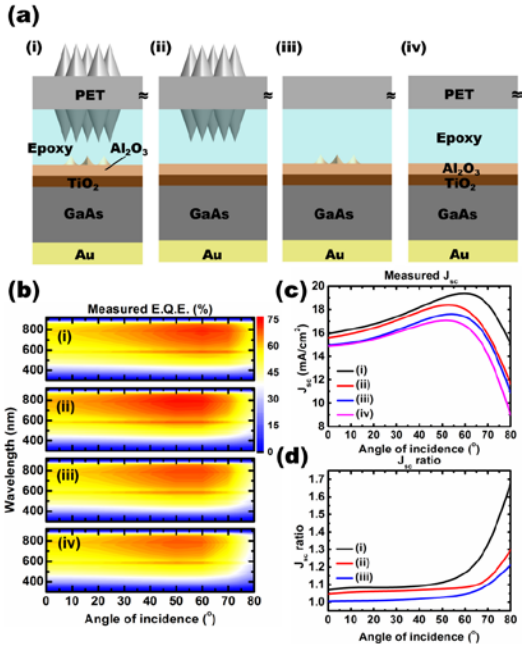

Figure 3.10: (a) Schematic diagrams of (i) "moth-eye" and "nanoisland" integrated with bilayer antireflection coating, (ii) "moth-eye" with bilayer antireflection coating, (iii) plane PET on "nanoisland" integrated with bilayer antireflection coating, and (iv) PET on bilayer antireflection coating. (b) Measured external quantum efficiencies as functions of wavelength and angle of incidences for structures (i)-(iv). (c)(d) Measured short circuit current and ratio as a function of angle of incidence for structure (i)-(iv).

3.3.5Conclusion

We have demonstrated an omnidirectional antireflection approach for solar cells integrated with polymer packaging based on creating “moth-eye” textures on polymer (PET) packaging sheets, which shows significant transmittance enhancement across the solar spectrum under normal and off-normal incident conditions compared to unpatterned polymer packaging sheet using a low-cost, high-throughput nanosphere lithography process. Also, utilizing the same lithography process, we fabricated Al_2O_3 dielectric “nanoisland” structure on the surface of conventional Al_2O_3/TiO_2 bilayer antireflection coating, which showed substantially reduced reflection loss from the interface between the Al_2O_3/TiO_2 bilayer antireflection coating and the space-grade encapsulant which was used to attach the PET packaging sheet to the cell, particularly at large incident angles. Numerical simulations were performed to elucidate the physics of this antireflection approach and to optimize optical nanostructures for such strategy. Finally, external quantum efficiency (E.Q.E.) measurements of the cell with Al_2O_3 “nanoislands” integrated with “moth-eye” textured PET packaging sheet and control cells with different light-trapping configurations were performed. The combination of these approaches yields increases in J_{sc} based on measurements of E.Q.E. combined with the AM1.5G solar spectrum, of ~1.1x at normal incidence, increasing to 1.67x at an incident angle of 80^o.

Chapter 4: Fabrication of birefringent nanocylinders for single-molecule force and torque measurement

4.1 MOTIVATION

Techniques such as optical tweezers[91-93], magnetic tweezers[94], atomic force microscopy[95], and fluorescence microscopy [96] have been developed to manipulate and observe single bio-molecules, enabling rare and transient events to be observed by avoiding the averaging that occurs in traditional ensemble measurements. Optical tweezers have been used to characterize various bio-molecules and biological processes in measurements of force and displacement in picoNewton and sub-nanometer regime. Examples of such studies include measuring mechanical properties of biopolymers, reconstructing energy landscapes for folding or unfolding secondary structure of nucleic acids and directly following the dynamics of motor proteins translocating on their tracks[97-101]. While most experiments characterize force and displacement, torque and angular motion play significant roles in biological phenomena such as DNA replication and transcription[102], ATP synthesis [103] and bacteria propulsion[104-105]. However, there have been relatively few reports on torque and angular measurements of bio-molecules due to the limited availability of methods to directly manipulate and detect such quantities. Here, we present a method to fabricate large quantities of birefringent cylinders rapidly at low cost using nanosphere lithography (NSL) [44-45, 106], and demonstrate their use for single-molecule experiments using an optical torque wrench (OTW) measurement. Key design considerations are described and compared with other methods. Nanocylinders of diameter ~500 nm and height ~800 nm were shown to provide stable angular trapping in OTW. Finally, the force and torque generated using the cylinders were calibrated, and linear and angular manipulations of twist-stretched DNA were demonstrated and are discussed.

The optical torque wrench [107] was developed for angular manipulation and precise detection of torque via trapping an optically anisotropic particle in a laser beam. Figure 4.1 (a) shows a birefringent particle whose ordinary axis (χ_o) and extraordinary axis (χ_e) are misaligned relative to an external electric field. As a consequence, a restoring torque (τ) from the cross product of the induced polarization (P) and external electric field (E) tends to align the extraordinary axis with the external electric field. The resulting torque can be expressed as

$$\tau = \mid \vec{P} \times \vec{E} \mid = \frac{1}{2}(\chi_0 - \chi_e)\,\mathrm{E}\sin 2\theta = \tau_0 \sin 2\theta, \tag{4-1}$$

where is θ the angle between electric field and extraordinary axis, and τ_0 is the maximum magnitude of torque which can be exerted on the particle. The torque signal can be determined by measuring the spin angular momentum transfer of the photon, i.e. imbalance of left- and right-circular components of the transmitted beam as shown in Figure 4.1 (b). Figure 4.1 (c) shows a typical OTW setup for single-molecule experiments. One end of the target bio-molecule is attached to the glass slide and the other end to a birefringent particle, which can be trapped by a tightly focused Gaussian beam. Controlling the position of the surface and the state of the input laser beam allows simultaneous stretching and rotating of the molecule. The multiple attachments make the torsion added to the molecule possible. The force and torque response can be detected by monitoring the position and polarization state of the transmitted trap beam.

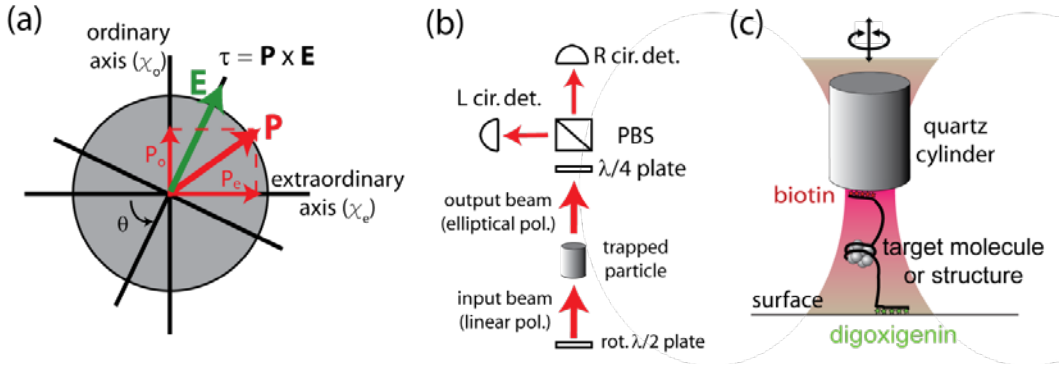

Figure 4.1: (a) Schematic diagram of a birefringent particle whose extraordinary axis is misaligned to the external electric field (E). Torque is generated when the induced polarization (P) is not aligned to the electric field (E). The angle between electric field and extraordinary axis (χ_e) is denoted as θ. (b) Schematic diagram of the torque detection in OTW. The torque signal is measured by detecting the imbalance of left- and right-circular polarized components of the scattered beam. PBS: polarizing beam splitter. (c) Schematic of OTW setup using fabricated quartz cylinders for single molecule experiments. The force and torque exerted on the bio-molecule are controlled by adjusting the polarization state of laser and the surface position.

A number of studies have reported on the design and fabrication of optimal particles for OTW[108-113]. The requirement of optical anisotropy can be obtained from shape properties or intrinsic material properties. In the case of form birefringence, the difference in dimensions and resulting anisotropy of polarizability make angular trapping possible, as reported for oblate particles[110]. However, it is difficult to obtain the uniformity of size and shape which is necessary for precise calibration in single-molecule experiments. In an alternate approach, birefringent quartz cylinders have been designed and fabricated for use in OTW, and these offer several advantages. First, the fabrication processes makes them easy to produce in large quantity and with high uniformity. Second, the elongated shape allows the symmetric axis of the cylinder to align with the propagation direction of the incident light, leaving only the rotational degree of freedom

to be controlled by the external field. Finally, for use in single-molecule experiments, the cylinder can be selectively functionalized only on the top surface, increasing the efficiency of achieving the appropriate geometry for measurement. In previous reports, fabrication of such cylinders was achieved by optical [111-112] or electron beam lithography[113]. However, these fabrication methods are either restricted in minimum feature size due to diffraction limits or are extremely time-consuming, and generally very expensive to carry out. Here, we implement a fabrication process for quartz cylinders suitable for OTW experiments using NSL. NSL has been previously developed and applied in production of anti-reflection coatings, sensing, and solar energy harvesting structure [66, 114-117]. We adapt the NSL technique to fabricate quartz nanocylinders with tunable sizes.

4.2 FABRICATION PROCESS AND STATISTICAL DISTRIBUTION OF FABRICATED BIREFRINGENT NANOCYLINDERS

The size of nanocylinders must be optimized for the specific application. For example, larger nanocylinders can provide larger torque under the same laser intensity and are suitable for experiments such as bacterial flagellar motors which are capable of generating torque up to 4000 pN.nm[118]. On the other hand, smaller nanocylinders offer faster response time and can be applied to molecular motors that do not generate large torque such as ATPase or RNA polymerase[102-103]. NSL readily provides the flexibility to produce a range of sizes of birefringent nanocylindersW. Figure 4.2 shows the key steps in the fabrication process for the birefringent nanocylinders. Starting from a 4" single crystal quartz (X-cut) substrate, 90nm Cr/10nm SiO_2 were deposited by e-beam evaporation. A self-assembled monolayer of 2μm diameter polystyrene (PS) nanospheres (with standard deviation of 200nm) were then deposited on the SiO2 surface using the Langmuir-Blodgett method [45, 106] as shown in Figure 4.2 (a). Reactive ion etching

(RIE) was used to etch the PS spheres to reduce the diameter to 1-1.5 μm. These nanospheres then served as an etch mask to transfer the hexagonal pattern to the underlying Cr, which acts as a hard mask containing Cr discs with diameter ~500nm as shown in Figure 4.2 (b). The quartz substrate with Cr hard mask on top then underwent RIE to yield quartz pillars ~800 nm in height as shown in Figure 4.2 (c). The Cr mask and residual polymer resulting from the dry etch were removed by a standard wet etch process. The diameter of the nanocylinders ranged from 50 nm to 1 μm depending on the size of the spheres and total etching time, and the height of the nanocylinders ranged from 500 nm to 2 μm, depending on the thickness of Cr mask. We note that the torque in OTW experiment is proportional to the volume of the nanocylinder since the signal strength depends on by the total angular momentum transfer of the nanocylinder. The aspect ratio of the nanocylinder should be also large enough to enable the alignment of the long axis of the nanocylinder with the laser beam. With these considerations, birefringent quartz nanocylinders with diameter 510 nm (with standard deviation of 20.35 nm) and height 800 nm (with standard deviation of 22.42 nm) were found to be suitable for single-molecule experiment in OTW[108].

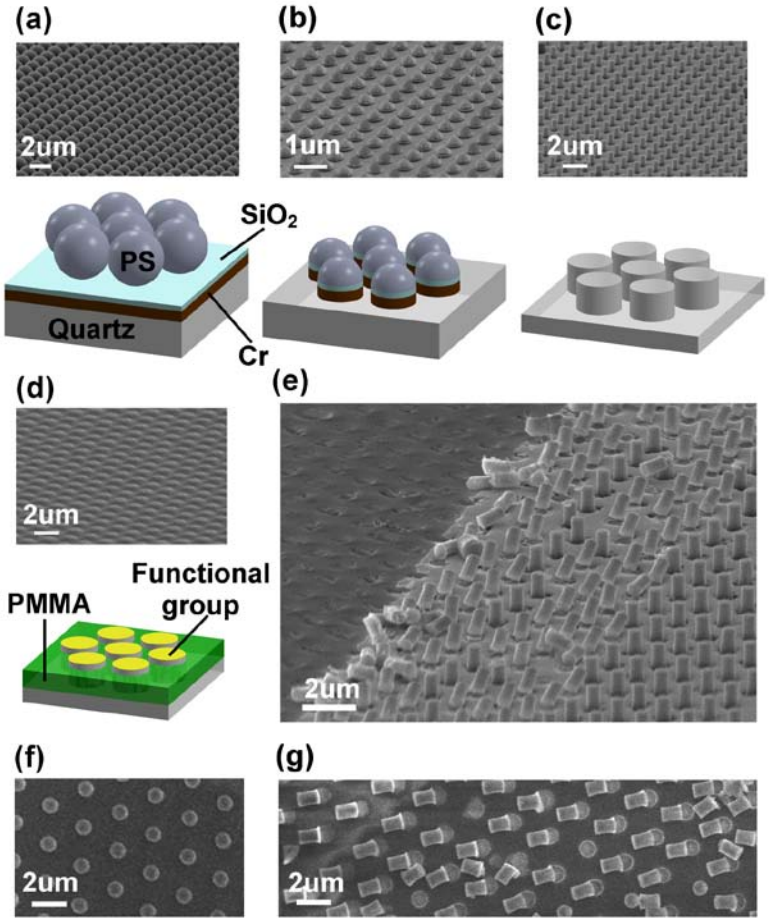

Figure 4.2: Schematic diagram of the fabrication process flow and scanning electron micrograph at each step: (a) A single crystal quartz substrate is covered with 10 nm Cr/100 nm SiO_2, followed by NSL using 2 μm diameter PS nanospheres. (b) A series of dry etching processes is used to reduce the sphere size and transfer the hexagonal lattice pattern to the underlying Cr layer. (c) Nanocylinders formed from single crystal quartz by dry etching using Cr mask which is later removed by wet etch process. (d) Nanocylinder buried in PMMA with only the top surface exposed for amino-group functionalization. (e) Single quartz cylinder after mechanical removal.

As shown in Figure 4.2 (d), the patterned substrate was spun coated with PMMA, and the excess PMMA etched away so that only the top surfaces of the nanocylinders were exposed. For application in single-molecule experiments, only the top surface was selectively functionalized with an amino group which is necessary for further avidin

coating. The excess PMMA was then etched away. Next, the wafer was incubated in 1% Vectabond reagent (Vector Laboratories, Inc.) for 5 minutes and then transferred to acetone for 30 minutes to remove the PMMA. The wafer was air-dried and cylinders are collected using a microtome blade (C.L. Sturkey, Inc.) as shown in Figure 4.2 (e). Finally, Avidin (Vector Laboratories, Inc.) molecules are coupled to the amino-functionalized cylinders using a Glutaraldehyde kit (Polysciences, Inc.). We note that controlling the distance between each nanocylinder and the aspect ratio are crucial to avoid incomplete removal of the nanocylinders and undesired quartz residues. For the experiment measuring twist-stretched DNA, the rotationally-constrained DNA was ligated from three pieces made separately by the polymerase chain reaction (PCR). The central piece was 1351 base pairs. Two short pieces incorporate multiple digoxigenin (322 base pairs) and biotin (336 base pairs) labelled nucleotides, which allows for torsionally constrained binding to the sample chamber surface and cylinder respectively. The detailed protocol for sample chamber creation and DNA binding to the surface and cylinder is similar to methods previously described for polystyrene sphere[119]. Briefly, the cover slip surface was coated with anti-digoxigenin, followed by blotting with buffer to prevent non-specific sticking of DNA to cylinders. The DNA and nanocylinder were then incubated, respectively. Finally, the sample are flowed and left with experimental buffer solution (50 mM sodium phosphate buffer pH 7.0, 50 mM NaCl, 10 mM EDTA, 0.02% Tween 20, and oxygen scavenger solution.) Using this process, a 4" quartz wafer provided ~10^8 nanocylinders, which was sufficient for calibration and measurement in a typical single-molecule experiment. Compared with conventional lithographies, the approach described here provides a rapid, low-cost, large-area nanoscale patterning technique covering a wide range of sizes.

Figure 4.3 (a) shows the distribution of nanocylinder diameters collected from different radial positions on the 4" wafer. The overall distribution for different positions is uniform and consistent with a standard normal distribution except for a few outliers due to imperfect distribution PS nanosphere. Figure 4.3 (b) shows the overall distribution of nanocylinder diameter. The averaged diameter is 510 nm with standard deviation of 20 nm. Figure 4.3 (c) shows the distribution of nanocylinder heights collected from different position from the 4" wafer center. The heights of the nanocylinders are overall uniform and more robustness to the variations of local plasma intensity. Figure 4.3 (d) shows the overall distribution of nanocylinder height. The averaged height is 800 nm with a standard deviation of 22 nm. To summarize, NSL can provide large numbers of birefringent nanocylinders with excellent uniformity.

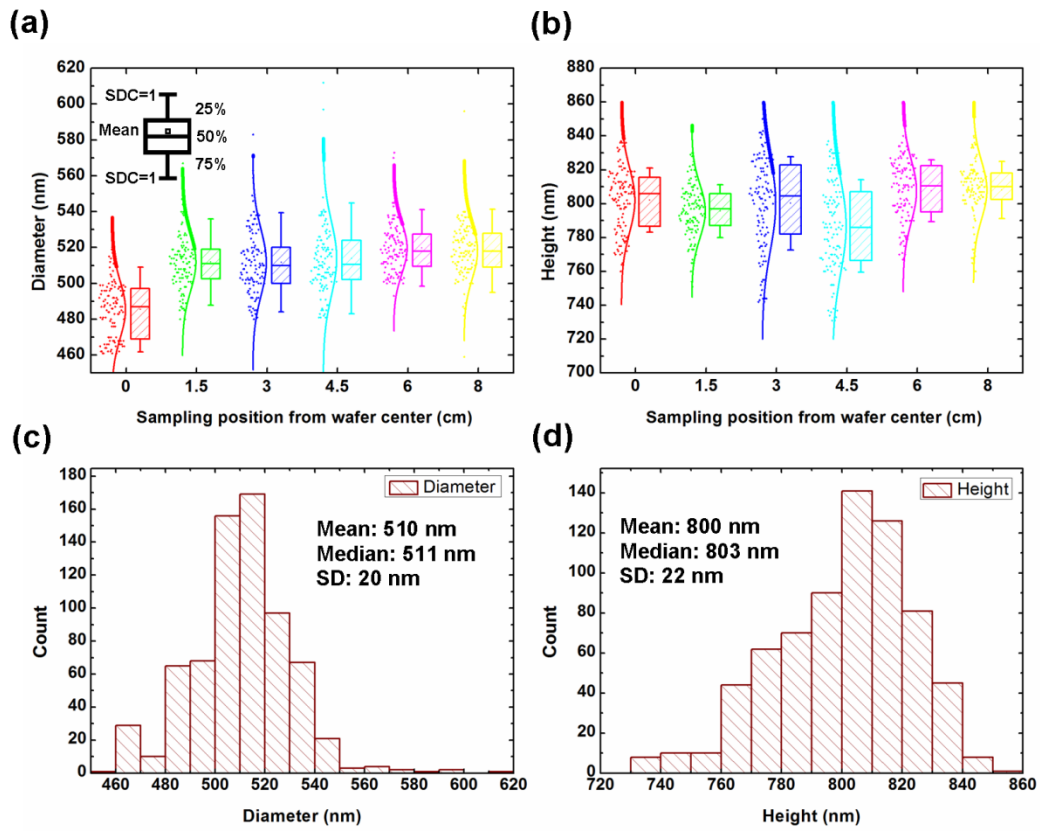

Figure 4.3: (a)(b) Distribution and box chart of nanocylinder diameter and height collected as a function of position from wafer center. The top and bottom of the box are the first and third quartiles. The median and mean are shown as the band and square symbol inside the box. The top and bottom whiskers stand for the standard deviation coefficient (SDC) equal to 1. (c)(d) Distributions of nanocylinder diameter and height fitted with normal distribution.

4.3 ANALYTICAL MODELING

4.3.1 Phase transition theory of DNA

The phenomenological model for DNA phase transition under force and torque can be understood by minimization of total free energies for combinations of different states. For a pure state (i) of DNA, the free energy of each state can be approximated as a function of linking number density (σ) and force (f) [120-121],

$$G_i(\sigma, f) = \varepsilon_i - g_i(f) + \frac{c_i(f)(\sigma - \sigma_{0,i})^2}{2}, \quad (4\text{-}2)$$

where ε_i is the energy offset, $\sigma_{0,i}$ is the relaxed linking number, $c_i(f)$ and $g_i(f)$ are the torsional coefficient and stretching energies as functions of force.

4.3.1.1 Free energies of stretched, plectonemic, and denatured states

(a) Stretched state ($i = s$)

The free energy of an extended DNA at a fixed force f can be expressed as [122-123]

$$G_s = -g_s(f) + \frac{c_s(f)\sigma^2}{2}, \quad (4\text{-}3)$$

where ε_s and $\sigma_{0,s}$ are zero since the force of interests is small (< 20 pN). The torsional coefficient and stretched energies in stretched state can be expressed as

$$c_s(f) = CkT\omega_0^2\left(1 - \frac{C}{4A}\sqrt{\frac{kT}{Af}}\right), \quad (4\text{-}4)$$

and

$$g_s(f) = f - \sqrt{\frac{kTf}{A}}, \quad (4\text{-}5)$$

respectively, where k is the Boltzmann constant, T is the temperature (we assume it is room temperature, 300 K), $\omega_0 = 2\pi/3.6nm = 1.85nm^{-1}$ is the contour-length rate of rotation of the relaxed double helix and A = 60 nm and C = 82 nm are the stretched and twist persistence length, respectively.

(b) Plectonemic state ($i = p$)

The free energy of a supercoiled DNA can be described by a quadratic model,

$$G_p = \frac{kTP\omega_0^2\sigma^2}{2}, \quad (4\text{-}6)$$

where P=18nm is the twist stiffness of the plectonemic state.

(c) Coexistence between stretched and plectonemic states

The mixed free energy of the coexistence state between stretched and plectonemic states can be written as

$$G_{s-p} = x_{s,+} G_s(\sigma_{s,+}) + x_p G_p(\sigma_p), \tag{4-7}$$

where $x_{s,+}$ is the fraction of stretched state, x_p is the fraction of plectonemic state, and they satisfy $x_{s,+}+x_p=1$. These quantities can be expressed as

$$x_{s,+} = \frac{\sigma_p - \sigma}{\sigma_p - \sigma_{s,+}}, \text{ and } x_p = \frac{\sigma - \sigma_{s,+}}{\sigma_p - \sigma_{s,+}}, \tag{4-8}$$

where $\sigma_{s,+}$ and σ_p are values at the onset and end of the stretching to the plectoneme transition, which can be calculated by minimization of free energy ($\frac{\partial G_{s-p}}{\partial \sigma_{s,+}} = 0$) with the constraint $\sigma = x_{s,+}\sigma_{s,+} + x_p\sigma_p$. They can be calculated as

$$\sigma_{s,+} = \frac{1}{c_s}\sqrt{\frac{2kTP\omega_0^2 g_s}{1 - kTP\omega_0^2 / c_s}}, \tag{4-9}$$

and

$$\sigma_p = \frac{1}{kTP\omega_0^2}\sqrt{\frac{2kTP\omega_0^2 g_s}{1 - kTP\omega_0^2 / c_s}}. \tag{4-10}$$

(d) Denatured state

We note that when the applied force is larger than 1 pN, the helix structure of DNA starts to denature upon negative rotations. Therefore, the corresponding denatured free energy needs to be modified to

$$G_d = \varepsilon_d - g_d(f) + \frac{c_d(f)}{2}(\sigma - \sigma_{0,d})^2, \tag{4-11}$$

where ε_d is the denaturation free energy, $\sigma_{0,d}$ = -0.8 is the relaxed linking number for denatured DNA, c_d is the twist rigidity of the denatured double helix, which is similar to c_s, and g_d is the stretched free energy for a denatured DNA which can be expressed as

$$g_d(f) = \lambda(f - \sqrt{\frac{kTf}{A_d}}), \tag{4-12}$$

where A_d = 4 nm, the persistence length of a denatured DNA, and λ = 1.2 is the factor to describe the increased length per base pair due to denaturation.

(e) Coexistence state between stretched and denatured states

The free energy for a mixed state of stretched and denatured states is therefore expressed as

$$G_{s-d} = x_{s,-}G_s(\sigma_{s,-}) + x_d G_d(\sigma_d), \tag{4-13}$$

where $x_{s,-}$ is the fraction of the stretched state in a denatured DNA, x_d is the fraction of denatured state, and they satisfy $x_{s,-} + x_d = 1$. These quantities can be expressed as,

$$x_{s,-} = \frac{\sigma_d - \sigma}{\sigma_d - \sigma_{s,-}}, \text{ and } x_d = \frac{\sigma - \sigma_{s,-}}{\sigma_d - \sigma_{s,-}}. \tag{4-14}$$

The onset and end, $\sigma_{s,-}$, and σ_d, can be calculated by minimization of coexistence free energy ($\frac{\partial G_{s-d}}{\partial \sigma_{s,-}} = 0$) with the constraint $\sigma = x_{s,-}\sigma_{s,-} + x_d\sigma_d$. They can be calculated as

$$\sigma_{s,-} = \frac{c_d}{c_s - c_d}\left(-\sigma_{0,d} - \sqrt{\sigma_{0,d}^2 + \frac{2(c_s - c_d)}{c_s c_d}(g_s + \varepsilon_d - g_d)}\right), \tag{4-15}$$

and

$$\sigma_d = \sigma_{0,d} + \frac{c_s}{c_s - c_d}\left(-\sigma_{0,d} - \sqrt{\sigma_{0,d}^2 + \frac{2(c_s - c_d)}{c_s c_d}(g_s + \varepsilon_d - g_d)}\right). \tag{4-16}$$

4.3.1.2 Extension curve

The modeled free energy (G_i) and linking number density (σ) can be converted into the experimentally measured quantities extension (z) and rotation turn, respectively, by

$$\frac{z}{L} = -\frac{\partial G_i}{\partial f}, \tag{4-17}$$

and

$$\sigma = \frac{\Delta Lk}{Lk_0} = \frac{n}{L/h}, \tag{4-18}$$

where Lk_0 is the normalized linking number of the relaxed DNA, L = 1351 bp is the total length of DNA studied here, h = 10.5 bp is the contour length of a single helix, and n is the number of rotation turns.

4.3.1.3 Table of constants

(a) Free energy of each state

States	**Coexistence of stretched and denatured states**	**Stretched state**	**Coexistence of stretched and plectonemic states**	**Plectonemic state**
Region	$\sigma_d<\sigma<\sigma_{s,-}$	$\sigma_{s,-}<\sigma<\sigma_{s,+}$	$\sigma_p>\sigma>\sigma_{s,+}$	$\sigma>\sigma_p$
Free energy	$G_{s-d}=x_{s,-}G_s(\sigma_{s,-})+x_dG_d(\sigma_d)$	G_s	$G_{s-p}=x_{s,+}G_s(\sigma_{s,+})+x_pG_p(\sigma_p)$	G_p

Table 4.1: Free energy expressions of each state

(b) Constants for each state

	Denaturation ($i=d$)	**Stretching** ($i=s$)	**Plectoneme** ($i=p$)
ε_i	$20kT/nm$	0	0
$\sigma_{0,i}$	-0.8	0	0
$g_i(f)$	$\lambda(f-\sqrt{\frac{kTf}{A_d}})$	$f-\sqrt{\frac{kTf}{A}}$	0
$c_i(f)$	$(6nm)kT\omega_0^2$	$CkT\omega_0^2(1-\frac{C}{4A}\sqrt{\frac{kT}{4f}})$	$PkT\omega_0^2$

Table 4.2: The detailed expressions of ε_i, $\sigma_{0,i}$, $g_i(f)$, and $c_i(f)$ in different energy states are summarized in the following table.

(c) Global constants

Parameters	*A*	*P*	*C*	A_d	ε_d	$\sigma_{0,d}$	λ
This work	60nm	18nm	82nm	4nm	20kT/nm	-0.8	1.2
References	43nm	24nm	95nm	5.5nm	6.25 kT/nm	-1.6	1.37

Table 4.3: The constants we used for this paper to describe the dynamics of DNA is summarized in the following table and compared with parameters from other references.

4.4MEASUREMENT OF DNA EXTENSION MEASUREMENT UNDER STRETCHING AND TORSIONAL FORCES

Accurate calibration of force and torque is required to perform precise quantitative measurements for a trapped nanocylinder in OTW. For cylinders of the size discussed here, the calibration of force and position follows the standard protocol for polystyrene (PS) particles of similar dimensions in optical tweezer experiments[93]. Analogous to force, the calibration of torque and rotation can be achieved by measuring the power spectrum of the torque signal (intensity difference in two detectors) for a trapped nanocylinder.[93, 107-108] The power spectrum can be fit by a Lorentzian line shape due to Brownian fluctuations in rotational motion[124]. This Lorentzian characteristic is modelled as $P(f) = A^2/(f^2 + f_0^2)$ with corner frequency $f_0 = \alpha/2\pi\xi$, and amplitude $A^2 = kT/\pi^2\alpha$, where α is the stiffness of the angular trap, ξ is rotational drag coefficient, *k* is the Boltzmann constant, and *T* is temperature in Kelvin. In Figure 4.4 (a) we observe that the measured power spectrum for a birefringent nanocylinder (solid squares) is in good agreement with the fit Lorentzian line (solid line), showing that the birefringent nanocylinder is angularly trapped; whereas a 820 nm diameter PS nanosphere (solid circles) is not trapped due to the lack of birefringence. The angular

sensitivity was measured by rotating the polarization on a cylinder fixed to the surface. Figure 4.4 (b) shows that the torque signal modulates sinusoidally, where θ rotating at 1.8 rad/s is the angle between the direction of the electric field and the extraordinary axis of the nanocylinder, as shown in Figure 4.1 (a) and V_0 is the maximum torque signal voltage obtained at θ=45°. Using the fitted parameters $f_0 = 204$ Hz and $A^2 = 9.8\times10^{-5}$ V^2Hz from data shown in Figure 3(a) as well as $V_0 = 0.11$ V in Figure 3(b), we obtain ξ = 2.1 pN.nm.s, $\alpha = 2.6\times10^3$ pN.nm/rad, and torque signal sensitivity 1.2×10^5 pN.nm/V. The measured torque signal can therefore be obtained by

$$\tau = \alpha\theta = \alpha(V_\tau / 2V_0)\,. \tag{4-19}$$

The maximum torque which can be generated here is ~1300 pN.nm, given the nominal laser power ~300 mW measured before the rotational half-wave plate. We note that the experimentally determined rotational drag coefficient here is consistent with other experimental [119] and theoretical work [125] for nanocylinders with similar dimensions.

We further demonstrate the application of the birefringent nanocylinder in single-molecule experiments by measuring a twisted and stretched DNA undergoing structural transition. The twisted state of DNA is regulated *in vivo* by topoisomerases, which influences the accessibility of DNA to many motor proteins. Therefore the mechanical properties of DNA under tension and torsion have profound implications in many biological contexts. Figure 4.4 (c) shows the measured and theoretically modelled extension of dsDNA recorded as a function of numbers of rotations under different stretching forces. Positive rotation is defined as the direction to overwind dsDNA. With positive torsion, the extension curves remain constant at low total turns (<3) since dsDNA is only overtwisted slightly. Beyond this region, the extension of dsDNA starts to drop abruptly and monotonically as total turns are added, indicating the dsDNA buckles to form a plectoneme. The critical number of turns for this sharp transition increases with

the applied force due to the increased rigidity of dsDNA under tension. Upon negative rotation, the extension responses with higher force (2.5 and 3.6 pN) remain almost constant because dsDNA prefers to unwind rather than buckle, therefore no plectoneme is formed. For lower force (1 pN), the dsDNA unwinds and buckles simultaneously when the total applied turn increases so that the extension curve drops without a sharp transition. For even lower force (0.3 pN), a symmetric extension response is expected based on the phase transition model[120]. The force is small enough that unwinding of helix structure is unfavorable and only the stretched and plectonemic states are allowed. The characteristics we observe in these measurements are consistent with other measurements performed using magnetic tweezers[126-127] and OTW[121, 128-129].

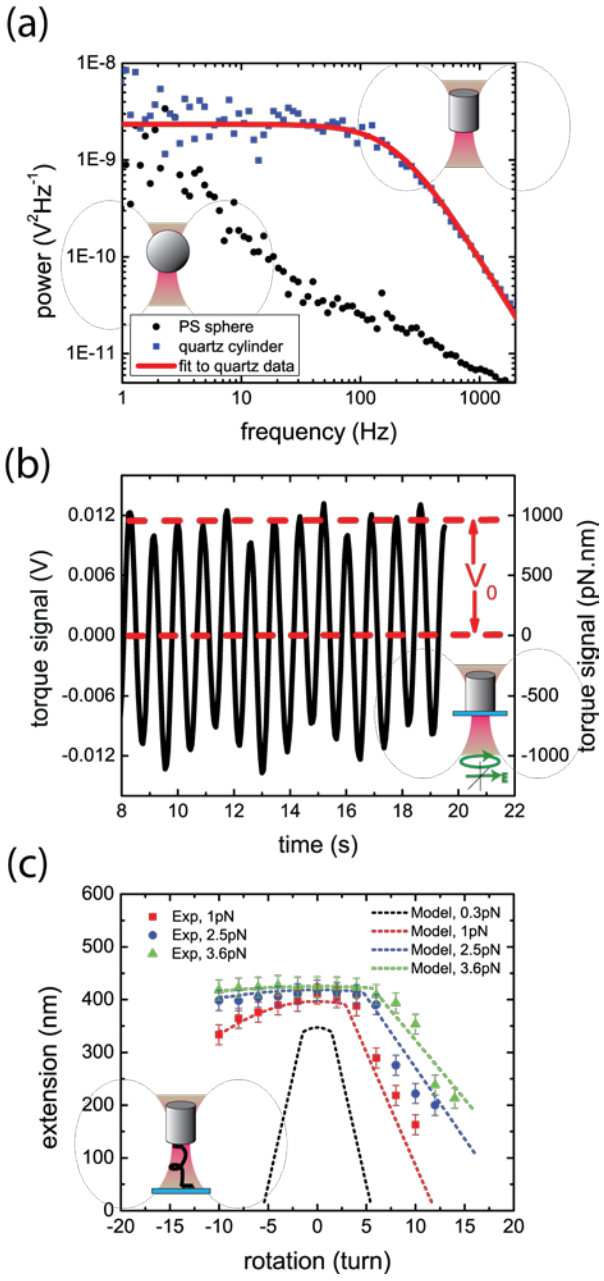

Figure 4.4. (a) Measured power spectra of torque signal for birefringent nanocylinders and polystyrene spheres with diameter of 820nm. The solid line indicates the Lorentzian fit for birefringent nanocylinders. (b) Torque signal of a fixed birefringent nanocylinder scanned by a rotating polarization vector. (c) Measured rotation-extension curve for a double-stranded DNA at different fixed forces. Gray dashed line indicates model prediction for low force limit.

4.5 CONCLUSION

In conclusion, a method for fabricating large quantities of birefringent nanocylinders using low-cost, rapid-patterning nanosphere lithography, and their use in single-molecule manipulation of dsDNA with optical torque wrench, are demonstrated. Patterning of the cylinder structures using nanosphere lithography offers a number of advantages over conventional lithographies employed in previous approaches, most notably in enabling rapid low cost fabrication of very large numbers of dielectric nanocylinders as required in OTW experiments. The calibration of force and torque in optical torque wrench measurements using dielectric nanocylinders fabricated in this way, together with the measured and modelled extension curve of double-stranded DNA under positive and negative rotation confirm the applicability of these birefringent nanocylinders in optical torque wrench measurements.

Chapter 5: Conclusions and Future Work

This dissertation has covered different applications of large-area subwavelength nanostructures including wide-angle wavelength-selective metasurface, omnidirectional enhancement in photovoltaic performance via subwavelength gradient anti-reflection coating, and applications of birefringent nanocylinders for single-molecule spectroscopy.

Chapter 2 summarized a series of works on wide-angle wavelength-selective metasurface. The best optimized metasurface with reflectance (>95%) and loss (<5%) were shown to be achieved with multilayer metasurface structures. These characteristics were shown to be independent of interlayer misalignment and insensitive to defects within individual layers. Interactions between different metasurfaces due to Fabry-Perot resonance were also examined with analytical model and numerical simulations. Wavelength-selective focusing at optical wavelengths which is enabled by large-area nanosphere lithography on a flexible substrate is demonstrated. The theoretical calculations and optimization of a proposed photovoltaic-thermal system show efficiency ~58.7%, which is superior to individual photovoltaics or thermal converters. Possible future work will emphasize 1) integrate fabrication processes with roll-to-roll nanoimprint lithography to achieve even larger patterned areas, 2) optimization and realization of a thermal absorber using low thermal emission materials such as carbon nanotubes to improve thermal-to-electrical energy conversion, 3) design and optimization of a Cassegrain reflector design for a trough mirror and a flexible metasurface to achieve the highest concentration factor, and 4) integration and test of a photovoltaic-thermal hybrid system.

Chapter 3 summarized a series of works on optimization and realization of omnidirectional enhancement in photovoltaic performance via subwavelength gradient

anti-reflection coatings. Large-area "moth-eye" structure fabricated on a flexible substrate is shown to have high transmittance (>85%) at large angles of incidence (>70^{o}) and insensitivity to polarizations. Integration of the "moth-eye" anti-reflection coating together with a nanostructured gradient Al_2O_3/TiO_2 on a GaAs solar cell shows significant improvements on external quantum efficiency (EQE) and short circuit current over all angle of incidences compared with conventional thin film anti-reflection coating. Detailed design, simulation, and fabrication of these nanostructured anti-reflection coating for reducing the discontinuity in refractive index profile will also be discussed. Possible future works will emphasize 1) reducing the defects and domain size of optical nanosctructures via nanosphere lithography, 2) further optimization of the interface between the packaging material and the GaAs solar cell, and 3) Realization and integration of antiflection nanosctructures on epitaxial lift-off GaAs cells.

Chapter 4 summarizes the application of birefringent nanocylinders to single-molecule spectroscopy, the design of and fabrication method for a large quantity of subwavelength birefringent nanoparticles. These birefringent nanoparticles were to be stably trapped in an optical torque wrench setup, which enabled observation of the dynamical response of a double-stranded DNA under torsional and extensional forces. Possible future work emphasize 1) further improvements in the resolution of the optical torque wrench setup, and 2) study of more complicated single-molecules such as nucleosomes.

References

1. Yu, N.; Genevet, P.; Aieta, F.; Kats, M. A.; Blanchard, R.; Aoust, G.; Tetienne, J. P.; Gaburro, Z.; Capasso, F., *Selected Topics in Quantum Electronics, IEEE Journal of* **2013,** *19* (3), 4700423-4700423. DOI 10.1109/jstqe.2013.2241399.
2. Chen, P.-Y.; Alù, A., *Physical Review B* **2011,** *84* (20), 205110.
3. Monticone, F.; Estakhri, N. M.; Alù, A., *Physical Review Letters* **2013,** *110* (20), 203903.
4. Yu, N.; Genevet, P.; Kats, M. A.; Aieta, F.; Tetienne, J.-P.; Capasso, F.; Gaburro, Z., *Science* **2011,** *334* (6054), 333-337. DOI 10.1126/science.1210713.
5. Cai, W.; Chettiar, U. K.; Yuan, H.-K.; de Silva, V. C.; Kildishev, A. V.; Drachev, V. P.; Shalaev, V. M., *Opt. Express* **2007,** *15* (6), 3333-3341.
6. Lassiter, J. B.; Sobhani, H.; Knight, M. W.; Mielczarek, W. S.; Nordlander, P.; Halas, N. J., *Nano Letters* **2011,** *12* (2), 1058-1062. DOI 10.1021/nl204303d.
7. Ye, J.; Wen, F.; Sobhani, H.; Lassiter, J. B.; Dorpe, P. V.; Nordlander, P.; Halas, N. J., *Nano Letters* **2012,** *12* (3), 1660-1667. DOI 10.1021/nl3000453.
8. Mousavi, S. H.; Kholmanov, I.; Alici, K. B.; Purtseladze, D.; Arju, N.; Tatar, K.; Fozdar, D. Y.; Suk, J. W.; Hao, Y.; Khanikaev, A. B.; Ruoff, R. S.; Shvets, G., *Nano Letters* **2013,** *13* (3), 1111-1117. DOI 10.1021/nl304476b.
9. Wu, C.; Khanikaev, A. B.; Adato, R.; Arju, N.; Yanik, A. A.; Altug, H.; Shvets, G., *Nat Mater* **2012,** *11* (1), 69-75. DOI http://www.nature.com/nmat/journal/v11/n1/abs/nmat3161.html#supplementary-information.
10. Zhu, Y.; Hu, X.; Huang, Y.; Yang, H.; Gong, Q., *Advanced Optical Materials* **2013,** *1* (1), 61-67. DOI 10.1002/adom.201200025.
11. Sun, Y.; Edwards, B.; Alù, A.; Engheta, N., *Nat Mater* **2012,** *11* (3), 208-212. DOI http://www.nature.com/nmat/journal/v11/n3/abs/nmat3230.html#supplementary-information.
12. Zhao, Y.; Belkin, M. A.; Alù, A., *Nat Commun* **2012,** *3*, 870.
13. Valentine, J.; Zhang, S.; Zentgraf, T.; Ulin-Avila, E.; Genov, D. A.; Bartal, G.; Zhang, X., *Nature* **2008,** *455* (7211), 376-379. DOI http://www.nature.com/nature/journal/v455/n7211/suppinfo/nature07247_S1.html.
14. Liu, N.; Hentschel, M.; Weiss, T.; Alivisatos, A. P.; Giessen, H., *Science* **2011,** *332* (6036), 1407-1410. DOI 10.1126/science.1199958.
15. Chanda, D.; Shigeta, K.; Gupta, S.; Cain, T.; Carlson, A.; Mihi, A.; Baca, A. J.; Bogart, G. R.; Braun, P.; Rogers, J. A., *Nat Nano* **2011,** *6* (7), 402-407. DOI http://www.nature.com/nnano/journal/v6/n7/abs/nnano.2011.82.html#supplementary-information.
16. Henzie, J.; Lee, M. H.; Odom, T. W., *Nat Nano* **2007,** *2* (9), 549-554. DOI http://www.nature.com/nnano/journal/v2/n9/suppinfo/nnano.2007.252_S1.html.
17. Lee, M. H.; Huntington, M. D.; Zhou, W.; Yang, J.-C.; Odom, T. W., *Nano Letters* **2010,** *11* (2), 311-315. DOI 10.1021/nl102206x.

18. Jiang, Z. H.; Yun, S.; Toor, F.; Werner, D. H.; Mayer, T. S., *ACS Nano* **2011,** *5* (6), 4641-4647. DOI 10.1021/nn2004603.
19. Pendry, J. B.; Aubry, A.; Smith, D. R.; Maier, S. A., *Science* **2012,** *337* (6094), 549-552. DOI 10.1126/science.1220600.
20. Alù, A.; Engheta, N., *Physical Review E* **2005,** *72* (1), 016623.
21. Chen, P.-Y.; Soric, J.; Alù, A., *Advanced Materials* **2012,** *24* (44), OP281-OP304. DOI 10.1002/adma.201202624.
22. Song, Y. M.; Xie, Y.; Malyarchuk, V.; Xiao, J.; Jung, I.; Choi, K.-J.; Liu, Z.; Park, H.; Lu, C.; Kim, R.-H.; Li, R.; Crozier, K. B.; Huang, Y.; Rogers, J. A., *Nature* **2013,** *497* (7447), 95-99. DOI 10.1038/nature12083
http://www.nature.com/nature/journal/v497/n7447/abs/nature12083.html#supplementary-information.
23. Li, P.-C.; Zhao, Y.; Alu, A.; Yu, E. T., *Applied Physics Letters* **2011,** *99* (22), 221106-3.
24. Li, P.-C.; Yu, E. T., *J. Opt. Soc. Am. B* **2013,** *30* (1), 27-32.
25. Li, P.-C.; Zhao, Y.; Alu, A.; Yu, E. T., *Applied Physics Letters* **2011,** *99* (22), 221106-3.
26. Li, L., *J. Opt. Soc. Am. A* **1997,** *14* (10), 2758-2767.
27. Moharam, M. G.; Gaylord, T. K., *J. Opt. Soc. Am.* **1981,** *71* (7), 811-818.
28. Lin, C.-H.; Leung, K. M.; Tamir, T., *J. Opt. Soc. Am. A* **2002,** *19* (10), 2005-2017.
29. Rakic, A. D.; Djuri?ic, A. B.; Elazar, J. M.; Majewski, M. L., *Appl. Opt.* **1998,** *37* (22), 5271-5283.
30. Palik, E. D., *Handbook of Optical Constants of Solids*. Academic Press: New York, **1991**.
31. Kottmann, J. P.; Martin, O. J. F., *Opt. Lett.* **2001,** *26* (14), 1096-1098.
32. Raether, H., *Surface Plasmons on Smooth and Rough Surfaces and on Gratings*. Springer: New York, **1988**.
33. Wood, R. W., *Physical Review* **1935,** *48* (12), 928-936.
34. Lim, S. H.; Mar, W.; Matheu, P.; Derkacs, D.; Yu, E. T., *Journal of Applied Physics* **2007,** *101* (10), 104309-7.
35. Li, P.-C.; Zhao, Y.; Alu, A.; Yu, E. T., *Applied Physics Letters* **2011,** *99* (22), 221106-3.
36. Alu, A., *Optical Wave Interaction with Two-Dimensional Arrays of Plasmonic Nanoparticles*. Cambridge University Press: New York, **2011**.
37. Taubert, R.; Ameling, R.; Weiss, T.; Christ, A.; Giessen, H., *Nano Letters* **2011,** *11* (10), 4421-4424. DOI 10.1021/nl202606g.
38. Haug, H.; Koch, S. W., *Quantum Theory of the Optical and Electronic Properties of Semiconductors*. 2nd ed.; World Scientific: Hong Kong, **1990**.
39. Yariv, A.; Yeh, P., *Photonics*. 6th ed.; Oxford University Press: New York, **2007**.
40. Born, M.; Wolf, E., *Principles of Optics*. 1st ed.; Pergamon Press: New York, **1959**.
41. Taubert, R.; Dregely, D.; Stroucken, T.; Christ, A.; Giessen, H., *Nat Commun* **2012,** *3*, 691.

42. Khitrova, G.; Gibbs, H. M.; Jahnke, F.; Kira, M.; Koch, S. W., *Reviews of Modern Physics* **1999,** *71* (5), 1591-1639.
43. Li, P.-C.; Yu, E. T., *J. Opt. Soc. Am. B* **2013,** *30* (1), 27-32.
44. Rybczynski, J.; Ebels, U.; Giersig, M., *Colloids and Surfaces A: Physicochemical and Engineering Aspects* **2003,** *219* (1–3), 1-6.
45. Ho, C.-C.; Chen, P.-Y.; Lin, K.-H.; Juan, W.-T.; Lee, W.-L., *ACS Applied Materials & Interfaces* **2011,** *3* (2), 204-208. DOI 10.1021/am100814z.
46. Macleod, H. A., *Thin-film Optical Filter*. 4th ed.; CRC Press: New York, **2010**.
47. Kats, M. A.; Blanchard, R.; Genevet, P.; Capasso, F., *Nat Mater* **2013,** *12* (1), 20-24. DOI http://www.nature.com/nmat/journal/v12/n1/abs/nmat3443.html#supplementary-information.
48. Christ, A.; Martin, O. J. F.; Ekinci, Y.; Gippius, N. A.; Tikhodeev, S. G., *Nano Letters* **2008,** *8* (8), 2171-2175. DOI 10.1021/nl0805559.
49. Dobrowolski, J. A.; Poitras, D.; Ma, P.; Vakil, H.; Acree, M., *Appl. Opt.* **2002,** *41* (16), 3075-3083.
50. Macleod, H. A., *Thin-Film Optical Filters*. 4th ed.; CRC Press: New York, **2010**.
51. Xi, J. Q.; Schubert, M. F.; Kim, J. K.; Schubert, E. F.; Chen, M.; Lin, S.-Y.; LiuW; Smart, J. A., *Nat Photon* **2007,** *1* (3), 176-179.
52. Kuo, M.-L.; Poxson, D. J.; Kim, Y. S.; Mont, F. W.; Kim, J. K.; Schubert, E. F.; Lin, S.-Y., *Opt. Lett.* **2008,** *33* (21), 2527-2529.
53. Welser, R. E.; Sood, A. W.; Pethuraja, G. G.; Sood, A. K.; Xing, Y.; Poxson, D. J.; Jaehee, C.; Schubert, E. F.; Harvey, J. L. In *Broadband nanostructured antireflection coating on glass for photovoltaic applications*, Photovoltaic Specialists Conference (PVSC), 2012 38th IEEE, 3-8 June 2012; **2012**; pp 003339-003342.
54. Cho, J.-Y.; Byeon, K.-J.; Lee, H., *Opt. Lett.* **2011,** *36* (16), 3203-3205.
55. Huang, Y.-F.; Chattopadhyay, S.; Jen, Y.-J.; Peng, C.-Y.; Liu, T.-A.; Hsu, Y.-K.; Pan, C.-L.; Lo, H.-C.; Hsu, C.-H.; Chang, Y.-H.; Lee, C.-S.; Chen, K.-H.; Chen, L.-C., *Nat Nano* **2007,** *2* (12), 770-774. DOI http://www.nature.com/nnano/journal/v2/n12/suppinfo/nnano.2007.389_S1.html.
56. Menna, P.; Di Francia, G.; La Ferrara, V., *Solar Energy Materials and Solar Cells* **1995,** *37* (1), 13-24.
57. Theiß, W., *Surface Science Reports* **1997,** *29* (3–4), 91-192.
58. Striemer, C. C.; Fauchet, P. M., *Applied Physics Letters* **2002,** *81* (16), 2980-2982.
59. Chen, J. Y.; Sun, K. W., *Thin Solid Films* **2011,** *519* (15), 5194-5198. DOI http://dx.doi.org/10.1016/j.tsf.2011.01.110.
60. Boden, S. A.; Bagnall, D. M., *Applied Physics Letters* **2008,** *93* (13), 133108-3.
61. Clapham, P. B.; Hutley, M. C., *Nature* **1973,** *244* (5414), 281-282.
62. Park, K.-C.; Choi, H. J.; Chang, C.-H.; Cohen, R. E.; McKinley, G. H.; Barbastathis, G., *ACS Nano* **2012,** *6* (5), 3789-3799. DOI 10.1021/nn301112t.
63. Yamada, N.; Ijiro, T.; Okamoto, E.; Hayashi, K.; Masuda, H., *Opt. Express* **2011,** *19* (S2), A118-A125.

64. Kanamori, Y.; Hane, K.; Sai, H.; Yugami, H., *Applied Physics Letters* **2001,** *78* (2), 142-143.
65. Deniz, H.; Khudiyev, T.; Buyukserin, F.; Bayindir, M., *Applied Physics Letters* **2011,** *99* (18), 183107-3.
66. Zhou, W.; Tao, M.; Chen, L.; Yang, H., *Journal of Applied Physics* **2007,** *102* (10), 103105-9.
67. Yang, Z.-P.; Ci, L.; Bur, J. A.; Lin, S.-Y.; Ajayan, P. M., *Nano Letters* **2008,** *8* (2), 446-451. DOI 10.1021/nl072369t.
68. Kanamori, Y.; Kikuta, H.; Hane, K., *Japanese Journal of Applied Physics* **2000,** *39*, L735-L737.
69. Chen, M.; Chang, H.-c.; Chang, A. S. P.; Lin, S.-Y.; Xi, J. Q.; Schubert, E. F., *Appl. Opt.* **2007,** *46* (26), 6533-6538.
70. Southwell, W. H., *J. Opt. Soc. Am. A* **1991,** *8* (3), 549-553.
71. Raguin, D. H.; Morris, G. M., *Appl. Opt.* **1993,** *32* (7), 1154-1167.
72. Grann, E. B.; Moharam, M. G.; Pommet, D. A., *J. Opt. Soc. Am. A* **1994,** *11* (10), 2695-2703.
73. Grann, E. B.; Varga, M. G.; Pommet, D. A., *J. Opt. Soc. Am. A* **1995,** *12* (2), 333-339.
74. Yanggang Andrew Xi, L. T., Bastiaan Arie Korevaar, Todd Ryan Tolliver, Dalong hZong Nanostructured Anti-reflection Coatings and Associated Methods and Devices. US20100259823, Oct. 14, **2010**.
75. Ekins-Daukes, N. J.; Barnham, K. W. J.; Connolly, J. P.; Roberts, J. S.; Clark, J. C.; Hill, G.; Mazzer, M., *Applied Physics Letters* **1999,** *75* (26), 4195-4197. DOI doi:http://dx.doi.org/10.1063/1.125580.
76. Luque, A.; Marti, A.; Stanley, C., *Nat Photon* **2012,** *6* (3), 146-152.
77. Sablon, K. A.; Little, J. W.; Mitin, V.; Sergeev, A.; Vagidov, N.; Reinhardt, K., *Nano Letters* **2011,** *11* (6), 2311-2317. DOI 10.1021/nl200543v.
78. Cotal, H.; Fetzer, C.; Boisvert, J.; Kinsey, G.; King, R.; Hebert, P.; Yoon, H.; Karam, N., *Energy & Environmental Science* **2009,** *2* (2), 174-192. DOI 10.1039/b809257e.
79. Winston, R.; Minano, J. C.; Benitez, P., *Nonimaging Optics*. Elsevier Academic Press: **2005**.
80. Trautz, K. M.; Jenkins, P. P.; Walters, R. J.; Scheiman, D.; Hoheisel, R.; Tatavarti, R.; Chan, R.; Miyamoto, H.; Adams, J. G. J.; Elarde, V. C.; Grimsley, J. In *Mobile Solar Power*, Photovoltaic Specialists Conference (PVSC), Volume 2, 2012 IEEE 38th, 3-8 June 2012; **2012**; pp 1-7.
81. Yoon, J.; Jo, S.; Chun, I. S.; Jung, I.; Kim, H.-S.; Meitl, M.; Menard, E.; Li, X.; Coleman, J. J.; Paik, U.; Rogers, J. A., *Nature* **2010,** *465* (7296), 329-333. DOI http://www.nature.com/nature/journal/v465/n7296/suppinfo/nature09054_S1.html.
82. Yu, P.; Chiu, M.-Y.; Chang, C.-H.; Hong, C.-Y.; Tsai, Y.-L.; Han, H.-V.; Wu, Y.-R., *Progress in Photovoltaics: Research and Applications* **2014,** *22* (3), 300-307. DOI 10.1002/pip.2259.

83. Guter, W.; Schöne, J.; Philipps, S. P.; Steiner, M.; Siefer, G.; Wekkeli, A.; Welser, E.; Oliva, E.; Bett, A. W.; Dimroth, F., *Applied Physics Letters* **2009,** *94* (22), -. DOI doi:http://dx.doi.org/10.1063/1.3148341.
84. Wei, G.; Shiu, K.-T.; Giebink, N. C.; Forrest, S. R., *Applied Physics Letters* **2007,** *91* (22), -. DOI doi:http://dx.doi.org/10.1063/1.2817753.
85. Konagai, M.; Sugimoto, M.; Takahashi, K., *Journal of Crystal Growth* **1978,** *45* (0), 277-280. DOI http://dx.doi.org/10.1016/0022-0248(78)90449-9.
86. Bauhuis, G. J.; Mulder, P.; Haverkamp, E. J.; Huijben, J. C. C. M.; Schermer, J. J., *Solar Energy Materials and Solar Cells* **2009,** *93* (9), 1488-1491. DOI http://dx.doi.org/10.1016/j.solmat.2009.03.027.
87. Liang, D.; Huo, Y.; Kang, Y.; Wang, K. X.; Gu, A.; Tan, M.; Yu, Z.; Li, S.; Jia, J.; Bao, X.; Wang, S.; Yao, Y.; Wong, H. S. P.; Fan, S.; Cui, Y.; Harris, J. S., *Advanced Energy Materials* **2012,** *2* (10), 1254-1260. DOI 10.1002/aenm.201200022.
88. Schubert, M. F.; Mont, F. W.; Chhajed, S.; Poxson, D. J.; Kim, J. K.; Schubert, E. F., *Optics Express* **2008,** *16* (8), 5290-5298. DOI 10.1364/oe.16.005290.
89. Chhajed, S.; Schubert, M. F.; Kim, J. K.; Schubert, E. F., *Applied Physics Letters* **2008,** *93* (25), -. DOI doi:http://dx.doi.org/10.1063/1.3050463.
90. Yan, X.; Poxson, D. J.; Cho, J.; Welser, R. E.; Sood, A. K.; Kim, J. K.; Schubert, E. F., *Advanced Functional Materials* **2013,** *23* (5), 583-590. DOI 10.1002/adfm.201201032.
91. Ashkin, A., *Physical Review Letters* **1970,** *24* (4), 156-159.
92. Ashkin, A.; Dziedzic, J. M.; Bjorkholm, J. E.; Chu, S., *Opt. Lett.* **1986,** *11* (5), 288-290.
93. Neuman, K. C.; Block, S. M., *Review of Scientific Instruments* **2004,** *75* (9), 2787-2809.
94. Tanase, M.; Biais, N.; Sheetz, M., Magnetic Tweezers in Cell Biology. In *Methods in Cell Biology*, Yu-Li, W.; Dennis, E. D., Eds. Academic Press: 2007; Vol. Volume 83, pp 473-493.
95. Lee, C.-K.; Wang, Y.-M.; Huang, L.-S.; Lin, S., *Micron* **2007,** *38* (5), 446-461. DOI http://dx.doi.org/10.1016/j.micron.2006.06.014.
96. Moerner, W. E.; Fromm, D. P., *Review of Scientific Instruments* **2003,** *74* (8), 3597-3619. DOI doi:http://dx.doi.org/10.1063/1.1589587.
97. Ashkin, A.; Dziedzic, J., *Science* **1987,** *235* (4795), 1517-1520. DOI 10.1126/science.3547653.
98. Bustamante, C.; Cheng, W.; Mejia, Y. X., *Cell* **2011,** *144* (4), 480-497.
99. Larson, M. H.; Landick, R.; Block, S. M., *Molecular cell* **2011,** *41* (3), 249-262.
100. Neuman, K. C.; Nagy, A., *Nat Meth* **2008,** *5* (6), 491-505.
101. Perkins, T. T., *Laser & Photonics Reviews* **2009,** *3* (1-2), 203-220. DOI 10.1002/lpor.200810014.
102. Ma, J.; Bai, L.; Wang, M. D., *Science* **2013,** *340* (6140), 1580-1583. DOI 10.1126/science.1235441.

103. Toyabe, S.; Watanabe-Nakayama, T.; Okamoto, T.; Kudo, S.; Muneyuki, E., *Proceedings of the National Academy of Sciences* **2011,** *108* (44), 17951-17956. DOI 10.1073/pnas.1106787108.
104. Chen, X.; Berg, H. C., *Biophysical Journal* **2000,** *78* (2), 1036-1041.
105. Xing, J.; Bai, F.; Berry, R.; Oster, G., *Proceedings of the National Academy of Sciences of the United States of America* **2006,** *103* (5), 1260-1265. DOI 10.1073/pnas.0507959103.
106. Kosiorek, A.; Kandulski, W.; Glaczynska, H.; Giersig, M., *Small* **2005,** *1* (4), 439-444. DOI 10.1002/smll.200400099.
107. La Porta, A.; Wang, M. D., *Physical Review Letters* **2004,** *92* (19), 190801.
108. Deufel, C.; Forth, S.; Simmons, C. R.; Dejgosha, S.; Wang, M. D., *Nat Meth* **2007,** *4* (3), 223-225. DOI http://www.nature.com/nmeth/journal/v4/n3/suppinfo/nmeth1013_S1.html.
109. Gutiérrez-Medina, B.; Andreasson, J. O. L.; Greenleaf, W. J.; LaPorta, A.; Block, S. M., Chapter 15 - An Optical Apparatus for Rotation and Trapping. In *Methods in Enzymology*, Nils, G. W., Ed. Academic Press: 2010; Vol. Volume 475, pp 377-404.
110. Huang, Z.; Pedaci, F.; van Oene, M.; Wiggin, M. J.; Dekker, N. H., *ACS Nano* **2011,** *5* (2), 1418-1427. DOI 10.1021/nn1034108.
111. Oroszi, L.; Galajda, P.; Kirei, H.; Bottka, S.; Ormos, P., *Physical Review Letters* **2006,** *97* (5), 058301.
112. Simpson, S. H.; Hanna, S., *J. Opt. Soc. Am. A* **2007,** *24* (2), 430-443.
113. Simpson, S. H.; Hanna, S., *J. Opt. Soc. Am. A* **2011,** *28* (5), 850-858.
114. Haynes, C. L.; Van Duyne, R. P., *The Journal of Physical Chemistry B* **2001,** *105* (24), 5599-5611. DOI 10.1021/jp010657m.
115. Li, P.-C.; Yu, E. T., *Journal of Applied Physics* **2013,** *114* (13), -. DOI doi:http://dx.doi.org/10.1063/1.4824371.
116. Li, P.-C.; Yu, E. T., *J. Opt. Soc. Am. B* **2013,** *30* (10), 2584-2588. DOI 10.1364/josab.30.002584.
117. Li, X. H.; Li, P. C.; Hu, D. Z.; Schaadt, D. M.; Yu, E. T., *Journal of Applied Physics* **2013,** *114* (4), -. DOI doi:http://dx.doi.org/10.1063/1.4816782.
118. Sowa, Y.; Hotta, H.; Homma, M.; Ishijima, A., *Journal of Molecular Biology* **2003,** *327* (5), 1043-1051. DOI http://dx.doi.org/10.1016/S0022-2836(03)00176-1.
119. de Messieres, M.; Brawn-Cinani, B.; La Porta, A., *Biophysical Journal* **2011,** *100* (11), 2736-2744. DOI http://dx.doi.org/10.1016/j.bpj.2011.03.067.
120. Marko, J. F., *Physical Review E* **2007,** *76* (2), 021926.
121. Sheinin, M. Y.; Wang, M. D., *Physical Chemistry Chemical Physics* **2009,** *11* (24), 4800-4803. DOI 10.1039/b901646e.
122. Marko, J. F., *Physical Review E* **1998,** *57* (2), 2134-2149.
123. Moroz, J. D.; Nelson, P., *Macromolecules* **1998,** *31* (18), 6333-6347. DOI 10.1021/ma971804a.
124. Svoboda, K.; Block, S. M., *Annual Review of Biophysics and Biomolecular Structure* **1994,** *23* (1), 247-285. DOI doi:10.1146/annurev.bb.23.060194.001335.

125. Tirado, M. M.; de la Torre, J. G., *The Journal of Chemical Physics* **1980,** *73* (4), 1986-1993. DOI doi:http://dx.doi.org/10.1063/1.440288.
126. Mosconi, F.; Allemand, J. F.; Bensimon, D.; Croquette, V., *Physical Review Letters* **2009,** *102* (7), 078301.
127. Strick, T. R.; Allemand, J.-F.; Bensimon, D.; Bensimon, A.; Croquette, V., *Science* **1996,** *271* (5257), 1835-1837. DOI 10.1126/science.271.5257.1835.
128. Forth, S.; Deufel, C.; Sheinin, M. Y.; Daniels, B.; Sethna, J. P.; Wang, M. D., *Physical Review Letters* **2008,** *100* (14), 148301.
129. Li, P.-C.; Chang, J.-C.; Porta, A. L.; Yu, E. T., *Nanotechnology* **2014,** *25* (23), 235304.